

## Ly $\alpha$ Emission from High Redshift Sources in COSMOS

Ryan P. Mallery<sup>1</sup>, Bahram Mobasher<sup>1</sup>, Peter Capak<sup>2</sup>, Yuko Kakazu<sup>2</sup>, Dan Masters<sup>2</sup>, Olivier Ilbert<sup>3</sup>, Shoubaneh Hemmati<sup>1</sup>, Claudia Scarlata<sup>4</sup>, Mara Salvato<sup>5</sup>, Henry McCracken<sup>6</sup>, Olivier LeFevre<sup>3</sup>, Nick Scoville<sup>2</sup>

### ABSTRACT

We investigate spectroscopically measured Ly $\alpha$  equivalent widths and escape fractions of 244 sources of which 95 are Lyman Break Galaxies (LBGs) and 106 Lyman Alpha Emitters (LAEs) at  $z \sim 4.2$ ,  $z \sim 4.8$ , and  $z \sim 5.6$  selected from intermediate and narrow-band observations. The sources were selected from the Cosmic Evolution Survey (COSMOS), and observed with the DEIMOS spectrograph. We find that the distribution of equivalent widths shows no evolution with redshift for both the LBG selected sources and the intermediate/narrow-band LAEs. We also find that the Ly $\alpha$  escape fraction of intermediate/narrow band LAEs is on average higher and has a larger variation than the escape fraction of LBG selected sources. The escape fraction does not show a dependence with redshift. Similar to what has been found for LAEs at low redshifts, the sources with the highest extinctions show the lowest escape fractions. The range of escape fractions increases with decreasing extinction. This is evidence that the dust extinction is the most important factor affecting the escape of Ly $\alpha$  photons, but at low extinctions other factors such as HI covering fraction and gas kinematics can be just as effective at inhibiting the escape of Ly $\alpha$  photons.

*Subject headings:* galaxies: evolution, galaxies: high-redshift, galaxies: ISM

---

<sup>1</sup>Department of Physics and Astronomy, University of California, Riverside, 900 University Ave, Riverside CA 92507

<sup>2</sup>California Institute of Technology, 1200 East California Boulevard, Pasadena, CA 91125

<sup>3</sup>Laboratoire d'Astrophysique de Marseille, CNRS-Universit de Provence, 38 rue Frdric Joliot-Curie, 13388 Marseille Cedex 13, France

<sup>4</sup>School of Physics and Astronomy, University of Minnesota, 116 Church St, Minneapolis, MN 55455

<sup>5</sup>Max-Planck-Institut fr Astronomie Knigstuhl 17 D-69117 Heidelberg, Germany

<sup>6</sup>Institut d'Astrophysique de Paris, UMR7095 CNRS, Universite Pierre et Marie Curie, 98 bis Boulevard Arago, 75014 Paris, France

## 1. Introduction

The study of the high redshift universe and the early evolution of galaxies has primarily relied on two techniques to obtain large samples of high redshift galaxies, the Lyman-break technique (LBGs; Steidel et al. 1999, Ouchi et al. 2004; Bouwens & Illingworth 2006, and references therein) and narrow band surveys targeting Ly $\alpha$  emitting galaxies (LAEs; Hu & McMahon 1996; Rhoads & Malhotra 2001; Ajiki et al. 2003; Hu et al. 2004; Taniguchi et al. 2005; Murayama et al. 2007, Gronwal et al. 2007, Ouchi et al. 2008; Hu et al. 2010, and references therein). Studying the difference in the nature and properties of the two populations, selected by these two techniques, helps to understand early stages of galaxy formation and provides constraints on reionization. However, the two populations of galaxies are found to have a degree of overlap, with a fraction of the LBGs having Ly $\alpha$  emission (Shapley et al. 2003; Kornei et al. 2010; Stark et al. 2010). The varying degree of overlap between the two techniques and how it changes with redshift is still an open question. Several authors have explored this by comparing spectral energy distributions (SED) properties of these two populations (Gawiser et al. 2007; Gronwall et al. 2007). Even less understood is the degree of overlap in the Ly $\alpha$  properties of the populations selected by these two techniques. Kornei et al. (2010) recently studied the Ly $\alpha$  properties of  $z \sim 3$  LBGs and found that LBGs with strong Ly $\alpha$  emission are older, have lower SFR, and are less dusty than objects with either weak Ly $\alpha$  emission, or the line in absorption. They concluded that, within the LBG sample, objects with strong Ly $\alpha$  emission represent a later stage of galaxy evolution in which supernovae-induced outflows have reduced the dust covering fraction. In contrast, analysis of LAEs at  $z \sim 3.1, 3.7,$  and  $5.7$  by Ouchi et al. (2008) have revealed that LAEs have lower extinction and/or younger ages than LBGs.

Due to the complex physics of Ly $\alpha$  radiative transfer process in galaxies, modeling Ly $\alpha$  emission, absorption, and escape has been investigated by numerous authors. Neufeld (1991) and Charlot & Fall (1993) modeled the Ly $\alpha$  radiative transfer and investigated the role of a clumpy, dusty, multiphase ISM on Ly $\alpha$  escape. Hansen & Oh (2006) has expanded on these past attempts by considering the effects of several different geometrical distributions of dust clouds, while Dijkstra et al. (2006) and Verhamme et al. (2006) have incorporated the effect of in-falling or outgoing spherical halos of neutral gas on Ly $\alpha$  escape and its profile. In particular, the monte-carlo radiative transfer models by Verhamme et al. (2008) taking into account dust, ISM kinematics, HI column densities, and gas temperature, have been able to reproduce the Ly $\alpha$  profiles of 11 LAEs found in Tapken et al. (2007).

Analysis of nearby Ly $\alpha$  emitting galaxies (Kunth et al. 2003; Mas-Hesse et al. 2003; Hayes et al. 2005; Ostlin et al. 2009; Atek et al. 2009; Scarlata et al. 2010) indicates that Ly $\alpha$  emission is affected by ISM geometry, gas kinematics and dust. However, the order of

importance of each of these factors is not clearly established and could possibly vary from object to object (Schaerer 2007). One method to ascertain the principle physical factors that affect the Ly $\alpha$  radiative transfer in galaxies, is to measure the Ly $\alpha$  escape fraction ( $f_{esc}$ ), defined as the ratio of the observed Ly $\alpha$  flux to what is expected from the star formation rate (SFR) of the galaxy. In recent years the study of the escape fraction of Ly $\alpha$  photons in star forming galaxies at redshifts ranging from  $z \sim 0.1 - 6$  has been studied by several authors (Scarlata et al. 2009; Finklestein et al. 2009; Atek et al. 2009; Hayes et al. 2010; Ono et al. 2010a; Ono et al. 2010b). Each study has found a strong trend of decreasing escape fraction with increasing extinction, though any change in the mean escape fraction of Ly $\alpha$  sources with redshift is uncertain given the difference in the methods of selecting samples of Ly $\alpha$  sources at  $z \sim 0.1$ ,  $z \sim 2$ , and  $z > 3$ .

In order to examine the varying degree of overlap between the Ly $\alpha$  properties of these two populations (LBGs and narrow band selected LAEs) and its redshift dependence, deep spectroscopic observations are required to measure the fraction of LBGs with Ly $\alpha$  emission. Spectroscopic follow-up for these high redshift sources has only recently been made possible due to the technical difficulties in the spectroscopy of faint,  $m_I > 22$ , high redshift sources. Ouchi et al. 2008 obtained Subaru/FOCAS and VLT/VIMOS spectroscopy of 84 out of 858 narrow band LAE candidates at  $z = 3.1, 3.7, \text{ and } 5.7$ . The Ly $\alpha$  luminosity function of these sources increases with redshift, indicating that galaxies with Ly $\alpha$  emission are more common at higher redshifts. Hu et al. (2010) presented an atlas of 88  $z \sim 5.7$  and 30  $z \sim 6.5$  spectroscopically confirmed LAEs. Ouchi et al. 2010 presented spectra of LAEs at  $z \sim 6.6$  examining the Ly $\alpha$  line profiles, the luminosity function, clustering properties of the sources. Analysis of their sample in comparison with LAEs at  $z \sim 5.7$  indicates that the intergalactic medium (IGM) was not highly neutral at  $z \sim 6.6$  and the bulk of reionization of the universe occurred at  $z > 7$ . Stark et al. (2010) spectroscopically confirmed 199 Ly $\alpha$  galaxies from a sample of 627 continuum selected LBGs at  $3 < z < 7$  and found that the fraction of LBGs with Ly $\alpha$  emission increases with redshift and is inversely correlated with UV luminosity. The likely cause of this is a decrease in dust extinction with redshift, and also a lower HI covering fraction for sources with lower UV luminosity.

In this paper we study Ly $\alpha$  emission from sources at  $4 < z < 6$ , detected in deep spectroscopic survey of the COSMOS field (Scoville et al. 2007). The selected sources consist of intermediate and narrow band LAEs at  $z \sim 4.2$  (IA624),  $z \sim 4.8$  (NB711) and  $z \sim 5.7$  (NB816), B $_J$  LBGs, g $^+$  LBGs, V $_J$  LBGs, r $^+$  LBGs, i $^+$  LBGs, and sources with photometric redshifts  $z > 4$ . In §2, we present the data, and the method used for source selection. In §3, we present our analysis of the Ly $\alpha$  emission as it relates to both redshift and our source selection. In §4 we estimate the Ly $\alpha$  escape fraction and perform a speculative analysis based on our estimates. Our conclusions are presented in §5. We assume  $H_o = 70 \text{ km s}^{-1}$

Mpc<sup>-1</sup>,  $\Omega_m = 0.3$ , and  $\Omega_\Lambda = 0.7$ . We assume AB magnitude. s

## 2. Data

### 2.1. DEIMOS Observations and Data Reduction

A total of 4267 sources were targeted for spectroscopic observations with the DEIMOS multi-slit spectrograph (Faber et al. 2003) on the Keck II telescope. Full details of the observations and data can be found in Capak et al. (in prep). A total of 42 separate slit masks were observed, each with on average 102 1" slits per mask. The observations were taken over a period of several semesters with 5 nights in January 2007, 4 nights in November 2008, 4 nights in November 2009, 7 nights in January 2010 and 5 nights in February 2010. The observations were taken with the 830 line BK7 grating with a wavelength coverage of  $\sim 6000 - 9000\text{\AA}$ . Observations of each mask were dithered by 1" with a total integration of 3.5 hours for each mask. Reductions were performed creating 1d spectra for each slit, using a variation of the standard DEIMOS spec2d reduction package in order to account for the dithered observations. Flux calibration was performed by first using stellar spectra to measure the detector response profile for each mask. The 1d spectra were then divided by the response profile and normalized. For absolute flux calibration, the spectra were then integrated over Subaru filter response profiles and scaled by the error-weighted mean ratio between magnitude (computed from the spectra) and Subaru photometry. Multi-bandpass Subaru photometry were used consisting of broad (r, i, z), narrow (NB711, NB816) and intermediate (IB624, IB709, IB738, IB767) band filters from the publicly available COSMOS optical catalog (see Capak et al. 2007)<sup>1</sup> The flux calibration procedure used, removes any slit-loss as the spectroscopy is scaled directly to the photometry.

### 2.2. Source Selection

A total of 1453 of the observed sources were selected to be at  $z > 3.8$ . After examination of their spectra, and removal of stellar sources and low- $z$  interlopers the number of possible  $z > 3.8$  sources is 644. The goal of the Keck program was to select as complete a sample

---

<sup>1</sup><http://irsa.ipac.caltech.edu/data/COSMOS/tables/photometry/> This catalog includes the photometry in all the 25 optical/NIR broad-, intermediate- and narrow-bands filters, from "u" to "Ks" . The photometry is computed at the position of the i\*-band image, using SExtractor (Bertin & Arnouts 1996) in dual mode. The catalog supersedes Capak et al. (2007), with improved source detection and photometry extracted in 3" apertures.

at  $z > 4$  as possible, for objects brighter than  $z^+ < 25$  and more massive than  $10^{10.5} M_{\odot}$  (Capak et al. in prep). To achieve this goal, a set of continuum selected objects brighter than  $z^+ < 25$  or IRAC  $[4.5\mu\text{m}] < 23.5$  were selected to satisfy the above magnitude and mass limits respectively. From this flux limited sample  $B_J$ ,  $g^+$ ,  $V_J$ ,  $r^+$ ,  $i^+$ , and  $z^+$  LBGs were selected using known criteria (Ouchi et al. 2004, Capak et al. 2004, 2011b, Iwata et al. 2003, and Hildebrandt et al. 2009). Objects with a probability greater than 50% of being at  $z > 4$ , based on the Ilbert et al. (2010) photo- $z$  catalog, were also included if they met the flux limit. Finally, to avoid any biases against heavily dust obscured objects (e.g. Capak et al. 2008, 2011a), sources meeting the LBG or photo- $z$  criteria and also detected by *Chandra*, *Spitzer* MIPS ( $24\mu$ ), AzTEC (1.1mm), Mambo (1.24mm), BoloCam (1.1mm) or the VLA (20cm) were also included in the sample even if they were fainter than the flux limit.

In addition, Ly $\alpha$  emitters were selected using the IA624, NB711, and NB816 bands following previous studies (Scarlata et al. in prep, Shioya et al. 2009, Murayama et al. 2007), with the modification that a fixed color cut was used to the faintest magnitudes as done in Hu et al. (2010) instead of a noise adjusted cut. To the NB711 sources selected by the Shioya et al. (2009) criteria, sources were also added with 0.3 magnitude excess between the NB711 and the interpolated  $r^+ i^+$  photometry, and also sources with a 0.3 magnitude excess between the NB711 and interpolated IA707 and IA738 magnitudes in order to add sources possibly having lower Ly $\alpha$  equivalent widths than the Shioya et al. (2009) selection criteria. To the NB816 sources selected by the Murayama et al. (2007) criteria, sources were also added with 0.3 magnitude excess between the NB816 and the interpolated  $i^+ z^+$  photometry, and also sources with a 0.3 magnitude excess between the NB816 and interpolated IA707 and IA738 magnitudes in order to add sources possibly having lower Ly $\alpha$  equivalent widths than the Murayama et al. (2007) criteria.

A total of 895 LBG sources were targeted for spectroscopy. Removal of low- $z$  contaminants and stars leaves 380  $z > 3.8$  LBG candidates. The Suprime-Cam  $z'$  magnitudes of the targeted LBGs range from 22.7 to 25 AB, with a mean of 24.8 AB. left panel of figure 1 (we refer to figure 1 again in section 2.4) shows the  $z'$  magnitude distribution of all the LBGs with spectroscopically measured redshifts. In addition to the LBGs, 83 IA624 LAEs at  $z \sim 4.2$ , 83 NB711 sources at  $z \sim 4.96$ , and 98 NB816 sources at  $z \sim 5.7$  were targeted for spectroscopy. After removal of stellar sources and low- $z$  contaminants, the distribution of LAEs becomes 26 at  $z \sim 4.2$  (IA624), 42 at  $z \sim 4.8$  (NB711) and 73 at  $z \sim 5.7$  (NB816). The IA624 sources have  $z'$  magnitudes range from 24.9 to 26.7 AB, with a mean of 25.8 AB. The NB711 sources vary in  $z'$  magnitudes from 23.6 to 27.2 AB with a an average of 24.9 AB, and the magnitudes of the NB816 sources vary from 24.1 to 27.2 AB with a mean of 25.6 AB. The right panel of figure 1 shows the  $z'$  magnitude distribution of the IA624, NB711 and NB816 sources with spectroscopically measured redshifts.

For the entire sample of 644 high redshift candidates, 244 have  $3\sigma$  detections of Ly $\alpha$ , with 86 having rest-frame Ly $\alpha$  equivalent widths ( $EW_{Ly\alpha,0} > 25\text{\AA}$ ). Table 1 lists the number of high redshift candidates, the sub-set with  $3\sigma$  Ly $\alpha$  detections, and the number with  $EW_{Ly\alpha,0} > 25\text{\AA}$  for each source type. Of the 380  $B_J, g^+, V_J, r^+$ , and  $i^+$  LBGs observed, 95/380 (32/380) have  $3\sigma$  detections of Ly $\alpha$  ( $EW_{Ly\alpha,0} > 25\text{\AA}$ ): 10/49 (3/49)  $B_J$ , 21/158 (3/158)  $g^+$ , 39/101 (16/101)  $V_J$ , 23/56 (9/56)  $r^+$  and 2/16 (1/16)  $i^+$ . The low number of  $i^+$  LBG sources with Ly $\alpha$  is likely due to low number statistics and the limit of our survey ( $z^+ < 25$ ), which selects only the bright sources ( $M_{UV} < -22$ ) at  $z \sim 6$  and the color selection criteria which selected mostly stars (98/114). We also find that 21/26 (9/26) of the IA624, 25/42 (9/42) of the NB711, and 60/73 (26/73) of the NB816 selected sources have  $3\sigma$  detections of Ly $\alpha$  ( $EW_{Ly\alpha,0} > 25\text{\AA}$ ).

### 2.3. Redshift, AGN, and Ly $\alpha$ Identification

Of the 644 high redshift candidates observed, 372 have high quality/reliable redshifts at  $z > 3.8$ . Each spectrum was examined by eye in IDL using **SpecPro** (Masters & Capak 2011) by at least two people, and often by three (RM, DM, & CP). Spectra with Ly $\alpha$  were easily identified by its asymmetric emission line shape (see figure 2). Spectra with only low S/N absorption features required several features before being confirmed. This included spectroscopic redshifts consistent with the photometric spectral energy distribution (SED), and agreement between independent estimates of the spectroscopic redshift.

The contamination of the high redshift sources by AGN is not well known. At the flux limits for the XMM survey of COSMOS (Cappelluti et al. 2009), we expect detections of only the high redshift sources with  $L_X > 10^{45}$  ergs/s. This is over three orders of magnitude higher than the standard AGN X-ray detection limit  $L_X > 10^{42}$  ergs/s. No sources are individually detected by XMM. One high redshift source ( $\alpha = 150.35980$   $\delta = 2.0737081$ ) is detected in the X-ray by *Chandra* in the C-COSMOS survey (Elvis et al. 2009), though unlike the XMM survey of COSMOS the *Chandra* survey is not uniform over the entire field. Two of the LBG sources are point sources in ACS ( $\alpha = 149.87082$   $\delta = 1.8827920$ , and  $\alpha = 150.13036$   $\delta = 2.4660110$  taken from Ikeda et al. 2011), but show no signs of AGN in their spectra, nor have x-ray detections.

Spectroscopic identification of AGN via NeV $\lambda$ 1238 emission or other broad emission lines ([CIV] $\lambda$ 1550 and CIII $\lambda$ 1908) is largely dependent on their redshifts. CIII $\lambda$ 1908 is redder than the wavelength cutoff for sources at  $z > 4.2$ , and [CIV] $\lambda$ 1550 for sources at  $z > 5.4$ . A total of 15/644 sources show possible signs of AGN in their spectra, with 6 of these also having

$\text{Ly}\alpha$  detections. Including the *Chandra* detection, this gives a lower limit of 2.9% (7/244) for AGN contamination in our  $\text{Ly}\alpha$  sample. AGN contamination in sources with  $\text{Ly}\alpha$  emission have been reported at 43% at  $z \sim 0.1$  (Finkelstein et al. 2009), 3%–7% at  $z = 2.1$  (Guaita et al. 2010), 5%–13% at  $z \sim 2.25$  (Nilsson et al. 2009), 1%–10% at  $z \sim 3.1 - 3.7$  (Gronwall et al. 2007; Ouchi et al. 2008; Lehmer et al. 2009),  $< 3.2\%$  ( $< 6.3\%$ ) for type-1 (type-2) AGN at  $z \sim 4.5$  (Zheng et al. 2010),  $< 5\%$  at  $z \sim 4.5$  (Malhotra et al. 2003; Wang et al. 2004), and  $< 1\%$  at  $z \sim 5.7$  (Ouchi et al. 2008).

## 2.4. Selection Bias

Selection bias for the sub-sample of high redshift spectroscopic sources with  $\text{Ly}\alpha$  emission is expected to be low as the spectroscopic sample was selected to be complete at  $z > 4$  for objects brighter than  $z^+ < 25$  and more massive than  $10^{10.5} M_{\odot}$ .  $\text{Ly}\alpha$  emission is detected to a redshift dependent flux limit of  $\sim 5e - 18$  ergs/s/cm<sup>2</sup>. Figure 1 shows the redshift plotted versus the  $z^+$  (AB) magnitude for all high redshift candidates with reliable spectroscopic redshift. Down to the limits of our survey ( $z^+ < 25$ ) there appears to be no bias between sources with  $\text{Ly}\alpha$  detections and those without, for both LBG and intermediate/narrow band selected sources. For the high redshift candidates observed using other selection criteria, the number statistics are too low for a meaningful comparison.

The amount of overlap between the LBGs and the intermediate/narrow-band selected LAEs is not fully known. In principle we can check which (if any) of the intermediate/narrow-band LAEs satisfy the color conditions used to select the LBGs. However, many of the intermediate/narrow-band LAEs are too faint and not detected in many of the various bands used to create the LBG source list. As figure 1 shows, most of the intermediate/narrow-band LAEs are fainter than the  $z^+ < 25$  criteria used to create the LBG source list. Relaxing this criteria for the intermediate/narrow-band LAEs, we can check the LBG color criteria for the intermediate/narrow-band LAEs that have the appropriate detections in the broad band photometry. For the 21 IA624  $\text{Ly}\alpha$  sources, 11 would be considered either  $B_J$ ,  $V_J$ , or  $g^+$  LBGs, 2 do not match any of the LBG criteria, and 8 are not detected in the enough bands to say one way or the other. For the 25 NB711  $\text{Ly}\alpha$  sources, 17 would be considered either  $B_J$ ,  $V_J$ ,  $g^+$  or  $r^+$  LBGs, 2 do not match any of the LBG criteria, and 6 are not detected in a sufficient number of bands to say one way or the other. For the 60 NB816  $\text{Ly}\alpha$  sources, 9 would be considered either  $V_J$ , or  $r^+$  LBGs, 23 do not match any of the LBG criteria, and 28 are not detected in the enough bands to anything definite.

## 2.5. Fraction of LBGs with Ly $\alpha$

The fraction of LBG sources with Ly $\alpha$  emission has recently become a potentially important ratio, as a decrease in this fraction at  $z > 6$  may be indicative of an increase of the neutral fraction of gas in the intergalactic medium (Furlanetto, Zaldarriaga & Hernquist 2006, Mesinger & Furlanetto 2008, Dayal, Maselli & Ferrara 2011). Currently, there has been some debate over whether such a trend has been detected. The luminosity functions of narrow-band LAEs studied by Kashikawa et al. (2006) and Ota et al. (2008) have shown a decline between  $z = 5.7$  &  $z = 7.0$  indicating that the IGM becomes increasingly neutral above  $z > 6$ , while those of Tilvi et al. (2010) and Krug et al. (2011) for narrow-band LAEs at  $z = 7.7$  are consistent with no evolution.

Several authors (Curtis-Lake et al. 2011, Stark et al. 2010, 2011, Schenker et al. 2011) have measured the fraction of LBG selected sources with spectroscopically detected Ly $\alpha$  emission at  $z > 4$ . At  $z \sim 7$  Ono et al. (2011), Pentericci et al. (2011) and Schenker et al. (2011) all find that the fraction decreases from  $z \sim 6$  to  $z \sim 7$ . Currently, there is a factor of 2 discrepancy between the fraction of luminous dropout sources with  $EW_{Ly\alpha,0} > 25\text{\AA}$  at  $z \sim 6$  (Curtis-Lake et al. 2011, Stark et al. 2010). Figure 3 shows the fraction of LBGs with  $EW_{Ly\alpha,0} > 25\text{\AA}$  and  $-20.25 < M_{UV} < -21.75$ . A completeness correction was made by adding simulated  $EW = 25\text{\AA}$  lines into the spectra (by RM), and having another author (SH) blindly search and measure the simulated lines. The mean completeness for the LBGs with  $EW_{Ly\alpha,0} > 25\text{\AA}$  and  $m_{continuum} < 26$  (AB) is 95%. In figure 3, the  $B_J$  and  $g^+$  LBGs are plotted together as a lower limit, since the the color selection criteria can select sources with redshifts below the minimum redshift that Ly $\alpha$  can be measured for the spectroscopic setup used. For the  $B_J$  and  $g^+$  LBGs at  $\langle z \rangle \sim 4.2$ , we calculate lower limit of 5%; for the  $V_J$  LBGs at  $\langle z \rangle \sim 4.6$ , we get a fraction of  $18 \pm 12\%$ ; and for the  $r^+$  LBGs at  $\langle z \rangle \sim 5$ , a fraction of  $15 \pm 16\%$ . These values agree, within the errors, with the fraction of LBGs with Ly $\alpha$  reported by Stark et al. (2010, 2011) and Schenker et al. (2011). Our estimates are below those reported by Curtis-Lake et al. (2011) and Stark et al. (2010, 2011) at  $z \sim 6$ , and do not support evolution in the fraction of LBGs with Ly $\alpha$  over the redshift range  $3.8 < z < 5.5$ .

## 2.6. Ly $\alpha$ Measurements

A detailed procedure is used to measure the flux, equivalent width (EW), peak wavelength and full width half maximum (FWHM) of the Ly $\alpha$  emission line in the spectra. Among the issues to overcome with the data concerning these measurements, is the faintness of the continuum, its low  $S/N \lesssim 1$ , and the varying shape of the Ly $\alpha$  feature which does not neces-



sarily ascribe to one consistent mathematical form from one source to the next. Variations in the continuum particularly effect the accuracy of our equivalent width measurements. In order to better elucidate our techniques, we first describe the particular method for ascertaining each measurement, and then describe the overall procedure. For several of the DEIMOS-COSMOS sources, the Ly $\alpha$  emission is double-peaked, with the wavelengths between the two peaks containing only detections of photons at the level of the continuum. These features are not [OII] as the long wavelength features shows a strong asymmetry, and the wavelength separation is always at least 5Å greater than would be expected if the features were [OII] doublets. For these cases the flux, equivalent width, peak wavelength, and FWHM are measured simultaneously for both peaks. Estimates of these quantities are made both from a skewed Gaussian fit to the data, and from numerical methods. A model for the skewed Gaussian is given in equation 1, with example spectra shown in figure 2. The fit returns values for the flux normalization (A), the first moment of a standard Gaussian ( $\lambda_0 = x + \omega\delta\sqrt{2/\pi}$ ), the second moment of a standard Gaussian ( $\sigma = \omega\sqrt{1 - 2\delta^2/\pi}$ ), the value of the skew (s), and the value of the continuum (c), where  $\delta = s/\sqrt{1 + s^2}$ . In figure 2, the skewed Gaussian fit to the Ly $\alpha$  line is shown in red, with the region used for numerical integration of the flux and equivalent width shown in blue. The flux, equivalent width, peak and fwhm of the Gaussian and their associated errors are derived by fitting equation 1 to the data.

$$flux = A * e^{-0.5*((\lambda-x)/\omega)^2} (\int_{-\infty}^{s(\lambda-x)/\omega} exp(-t^2/2) dt) + c \quad (1)$$

To determine the peak wavelength of the Ly $\alpha$  emission, we first calculate the derivative of each spectrum numerically. The peak is then taken to be the wavelength of the emission feature where this derivative is zero. The flux is then measured by numerical integration of the data, using Simpson’s rule, where the continuum of the Gaussian fit is subtracted from the spectrum. The wavelength bounds for the numerical integration are determined by first nearest neighbor smoothing the spectrum. The bounds used for the numerical integration are then the first pixels in the smoothed spectrum nearest to the peak that fall below the continuum of the Gaussian. The region used for numerical integration is illustrated in figure 2. Using these bounds, the unsmoothed spectrum minus the continuum is numerically integrated. In order to estimate the error, the numerical flux integration is repeated 500 times, each time the spectrum is varied randomly by the error of each pixel. The error of the numerically integrated flux is the standard deviation of 500 the iterations. Increasing the number of iterations was found to have a negligible effect on the determined errors of the flux, EW, and FWHM.

The EWs are numerically integrated via Simpson’s rule with the same boundaries as

the flux, and the same continuum value from the Gaussian fit. We impose the criteria that the continuum determined by the Gaussian be positive and only determine the EW for these cases. The spectra was used to determine the continuum instead of the broadband photometry in order to limit any biases that may be introduced due an assumption of the UV slope. The EW error is calculated in a similar fashion as the measurement of the flux errors. However, the distribution of the EWs tend to be skewed to lower values due to the faintness and low S/N detection of the continuum for most of the sources. Therefore, the standard deviation is a bad representation of the error. Instead, the 15.9% and 84.1% percentile values of the distributions are reported. The EWs are then converted to rest-frame EWs by dividing by  $(1+z)$ . In figure 4, we compare the EWs measured using the continuum from the spectra, versus EWs measured using continuum fluxes derived from the photometry. The continuum flux at 1215Å is derived from the photometry by quadratic interpolation of the photometry for each source from each band (listed in §2.1) with at least a  $5\sigma$  detection. Only 104 sources have photometric detections to the red and blue (or at the wavelength) of the Ly $\alpha$  line to constrain the continuum flux at Ly $\alpha$  from the photometry. The EWs are consistent within the errors for 75% of the sources, and only 4% have greater than a  $2\sigma$  deviation.

The FWHM is measured from the spectra by first fitting b-splines to the blue side of the peak pixel, and another to the red side of the peak pixel. Each spline is mirrored and the FWHM is then measured for each. The FWHM is taken as the average of the FWHM for two splines. This procedure is repeated 500 times varying the spectrum by its errors as in the other numerical calculations, and the error of the FWHM is taken to be the standard deviation of the 500 FWHM simulations.

The procedure we use to incorporate each of the measurements described above also takes into account how the wavelength boundaries used for the Gaussian fit affects our measurements and errors. First, for each Ly $\alpha$  emission feature, the spectrum is smoothed with 3-pixel boxcar and fitted with the skewed Gaussian in equation 1, using MPFIT (Markwardt 2008) in IDL, without specifying the wavelength range around the emission line. This fit is used to make an initial estimate of the continuum, the centroid and width of the emission feature. (NOTE: For the sources with two peaks, both features are fitted simultaneously). The wavelength boundaries for the numerical integration are estimated, and the skewed Gaussian is again fit to the data but only to the continuum on the red-side of the emission peak. Next, an iterative procedure is applied to compensate for any systematics that are introduced from the choice of the continuum region that is used in the fit. The skewed Gaussian is fit to the data covering a wavelength range from the short wavelength boundary used for numerical integration out to  $\lambda_0 + 4 * \sigma$ . The coefficients and errors on the coefficients for the skewed Gaussian fit are used to calculate the flux, EW, peak and FWHM of the skewed Gaussian. As detailed above, the wavelength boundaries for the numerical integration are

determined and the flux, EW, peak, and FWHM and corresponding errors are calculated. The wavelength range is increased on the long wavelength side of the centroid by  $\lambda_0 + 4 * \sigma + 1$  pixel, and a new skewed Gaussian is fitted to the data and the measurements are calculated again. This is iteratively done until the boundaries for the Gaussian fit are equal to  $\lambda_0 + 10\sigma$ . This usually needs  $\sim 30$  iterations for each Ly $\alpha$  feature. The median of the flux, EW, and FWHM, is taken as our best estimate, and except for the EWs, the standard deviation for each is added in quadrature to the error estimates from the individual iterations to obtain our final error estimates. For the EW errors, every equivalent width calculation made for every iteration is placed into a single distribution and the 15.9% and 84.1% percentile values are taken as the error on the numerically integrated equivalent widths. Table 2 shows the numerically estimated values for sources with a single Ly $\alpha$  peak and Table 3 shows the values for the sources with both a blue and redshifted Ly $\alpha$  peak.

### 3. Equivalent Width and Redshift Distribution

The redshift distribution of the Ly $\alpha$  sources is shown in figure 5 and the distribution of  $EW_{Ly\alpha,0}$  is plotted in figure 6. These are divided into three categories: the total sample, the intermediate/narrow band LAEs, and the LBGs. The mean (median)  $EW_{Ly\alpha,0}$  stay roughly constant with redshift but have a larger sample variance with increasing redshift for LBGs from  $21.9(19.6) \pm 9.0\text{\AA}$  for  $B_J$  LBGs,  $19.5(20.8) \pm 9.9\text{\AA}$  for  $g^+$  LBGs,  $25.4(21.1) \pm 14.1\text{\AA}$  for  $V_J$  LBGs,  $25.0(20.8) \pm 19.4\text{\AA}$  for  $r^+$  LBGs. The mean (median)  $EW_{Ly\alpha,0}$  for the intermediate/narrow band LAEs show a similar trend with redshift and a larger variance with redshift, from  $27.2(25.0) \pm 10.9\text{\AA}$  for IA624 LAEs and  $21.9(23.5) \pm 9.5\text{\AA}$  for NB711 selected sources to  $26.6(24.9) \pm 14.1\text{\AA}$  for NB816 selected sources. A comparison between the Ly $\alpha$  properties of the intermediate/narrow-band LAEs and the LBGs at similar redshifts will be instructive. While, unfortunately there are too few  $i^+$  LBGs to compare with the NB816 selected sources, a comparison can be made between the  $g^+$  LBGs and the IA624 LAEs as well as the  $V_J$  LBGs and the NB711 sources. The  $g^+$  LBGs and the intermediate band IA624 LAEs both have the same number of sources (21) and the number of sources in the NB711 sample (24) is roughly 3/5 the number  $V_J$ -dropouts (39). The IA624 LAEs have a slightly higher mean and a larger distribution of  $EW_{Ly\alpha,0}$  than the  $g^+$  LBGs, while the  $V_J$  LBG sample has a larger mean  $EW_{Ly\alpha,0}$  and a larger variance than the NB711 sources. Comparing  $EW_{Ly\alpha,0}$  for only the  $V_J$ -dropouts with NB711 LAEs with similar magnitudes ( $z^+ < 25$ ) though brings their median values into agreement at  $21.2\text{\AA}$  and  $21.0\text{\AA}$  respectively. None of the IA624 LAEs are brighter than  $z^+ < 25$  to compare with the  $g^+$  LBGs, but it is likely that the differences between the Ly $\alpha$  distributions for the LBGs and LAEs at a given redshift is due to the narrow band sample being fainter than the LBG sample.

The  $EW_{Ly\alpha,0}$  for our entire sample are plotted versus redshift in figure 7. We find that the median  $EW_{Ly\alpha,0}$  for the LBG and LAE sub-samples stay roughly constant with redshift. At  $z < 3$ , an increase in the distribution of  $EW_{Ly\alpha,0}$  with redshift has also been reported by Nilsson et al. (2009). They found that the distribution of EWs for  $z \sim 3$  LAEs studied by Gronwall et al. (2007) was higher than the distribution of EWs for their sample of LAEs at  $z \sim 2.25$ . They speculated that the change in EW distributions with redshift is the result of increased dust content in LAEs at lower redshifts. An increase in Ly $\alpha$  EWs with redshift has also been discovered in LBGs. Stark et al. (2010) found in their sample of  $\sim 199$  LBGs with detected Ly $\alpha$  emission at  $z = 3 - 6$ , that the prevalence of large EWs increases moderately with redshift.

Several authors (Shapley et al. 2003; Stark et al. 2010) have noted an anti-correlation between UV luminosity and EW. This has been refuted by Nilsson et al. (2009) who argued that the lack of luminous sources with high EWs may be due to the fact that luminous sources and sources with high EWs are both rare, and that this parameter space has been poorly represented in current flux limited surveys. Kornei et al. (2010) found only a marginal correlation between the EWs and UV luminosities for a large sample of LBGs at  $z \sim 3$ , with  $M_{UV} < -20$ . In the sample of LBGs studied in Stark et al. (2010), which detects sources to  $M_{UV} = -18$ , the authors found low-luminosity LBGs ( $M_{UV} = -19$ ) to show strong Ly $\alpha$  emission much more frequently than luminous systems ( $M_{UV} = -21$ ). For our sample, no correlation is found between the EWs and UV luminosities, neither for the full sample nor for the LBG selected sources. This is likely to be a selection effect as our LBG selected sources are mostly bright, with  $M_{UV} < -20$ .

#### 4. Estimating the Escape Fraction

The simplest method to estimate the escape fraction is to measure the flux of both Ly $\alpha$  and extinction corrected H $\alpha$ , assume a recombination regime (usually CASE B recombination, Osterbrock 1989), and compute the number of detected Ly $\alpha$  photons divided by the number of expected Ly $\alpha$  photons estimated from the H $\alpha$  flux. For the redshifts of our sources, H $\alpha$  is redshifted to the near-infrared and is currently unaccessible. We can however make a crude estimate of the escape fraction by noting that both the Ly $\alpha$  and H $\alpha$  fluxes are related to the star formation rate of the galaxy. By comparing the Ly $\alpha$  SFR versus an independently measured SFR, we can calculate a crude estimate of the Ly $\alpha$  escape fraction ( $f_{esc}$ ).  $f_{esc} = SFR_{Ly\alpha}/SFR_{BC03}$ , where  $SFR_{BC03}$  is the SFR predicted from Bruzual & Charlot (2003) models. A similar technique was used in Ono et al. (2010) to measure the escape fractions of narrow-band LAEs at  $z = 3 - 4$ .

Using the spectroscopic Ly $\alpha$  redshifts, the *Le Phare*<sup>2</sup> SED fitting code was used to generate estimates of SFR, E(B-V) and stellar mass for the sources. The SED fitting was performed following Ilbert et al. (2010), with the redshifts of the model SEDs fixed to the spectroscopic redshifts of our sources. Briefly, a set of galaxy templates were generated using Bruzual & Charlot (2003) with exponentially declining SFRs, two metallicities, Calzetti et al. (2000) extinction, and including emission features (Ly $\alpha$ , [OII], [OIII], H $\beta$  and H $\alpha$ ). See Table 1 from Ilbert et al. (2010) for a list of the parameter values used. Using a  $\chi^2$  procedure, the templates were fit to the multi-band optical/near-infrared photometry taken from 6 broad bands from the SuprimeCam/Subaru camera ( $B_J$ ,  $V_J$ ,  $g^+$ ,  $r^+$ ,  $i^+$ ,  $z^+$ ), 1 broad band from MEGACAM at CFHT ( $u'$ ), 14 medium and narrow bands from SuprimeCam/Subaru (IA427, IA464, IA484, IA505, IA527, IA574, IA624, IA679, IA709, IA738, IA767, IA827, NB711, NB816), the  $Y$ ,  $J$ ,  $H$ , and  $K_s$  broad bands from the Ultra-Vista survey of COSMOS (McCracken et al. 2012)<sup>3</sup> (in the region outside the survey coverage of the Ultra-Vista data the J-band from the WFCAM/UKIRT camera, H- and K-band from the WIRCAM/CFHT camera are used), and the 4 IRAC/*Spitzer* channels. From the fits, the median SFRs, and stellar masses are used along with the 16 and 84 percentile values are taken as the errors on for the SFR and stellar mass estimates. The errors on the SFRs and stellar masses are typically large (about an order of magnitude). The large uncertainties are due mostly to the faintness of the sources, since they are mostly detected at the 3-7 $\sigma$  level in the photometry. The E(B-V) value used is from best fit SED. The results of the SED fitting are listed in table 4.

For 153 of the 244 sources with 3 $\sigma$  Ly $\alpha$ , the SED fitting produced a best fit SED with  $\chi^2 < 50$  (4  $B_J$  LBGs, 16  $g^+$  LBGs, 20  $V_J$  LBGs, 16  $r^+$  LBGs, 2  $i^+$  LBG, 16 IA624, 19 NB711, 33 NB816 sources, and 27 from the various other selection methods), and the following analysis is restricted to these. The  $\chi^2 < 50$  criteria was chosen after inspection of the best fit SED and photometric data points of each source. For sources with  $\chi^2 > 50$ , the best fit SED was a bad match for 3 or more of the rest-frame UV and optical data points. These sources may have properties outside of the parameter space covered by the galaxy models and hence the SED fitting may produce unreliable estimates, and so these sources were excluded from the subsequent analysis. For sources with  $10 < \chi^2 < 50$ , these were

---

<sup>2</sup><http://www.oamp.fr/people/arnouts/LEPHARE.html>

<sup>3</sup>The Ultra-Vista data cover the central 1x1.5 degree area of the COSMOS survey in  $Y$ ,  $J$ ,  $H$ , and  $K_s$  bands with an exposure time of 11.8, 13.8, 11.8, and 10.9h respectively. The estimated 5 $\sigma$  depths are  $Y = 24.6$ ,  $J = 24.7$ ,  $H = 23.9$ ,  $K_s = 23.7$  AB. Deeper IRAC data from several small programs targeting our spectroscopic area and the SEDS survey have also been included in the photometry, significantly improving the mass estimates for fainter targets. These data reach an exposure time of 2-12h per pixel in the 3.6 $\mu$ m and 4.5 $\mu$ m bands.

the result of 1 to 2 discrepant photometric data points where the best fit SED matched the other data points within the errors. We use the SFR values to estimate our escape fractions. To convert our Ly $\alpha$  fluxes into SFRs, we first assume CASE-B recombination and convert the measured Ly $\alpha$  luminosities into expected H $\alpha$  luminosities ( $L_{H\alpha} = L_{Ly\alpha}/8.7$ ) and then to SFRs using equation 2 in Kennicutt (1998). We plot the Ly $\alpha$  luminosity versus stellar mass and SFR in figures 8 and 9 respectively. No trend between the Ly $\alpha$  luminosity and either mass or SFR is observed. The LAEs tend to have higher Ly $\alpha$  luminosities than the LBGs, but the LBGs, NB711 and NB816 LAEs have similar stellar mass ( $\sim 10^{10} M_{\odot}$ ), and SFRs ( $\sim 50 M_{\odot}/\text{yr}$ ). The IA624 LAEs on average have slightly lower stellar masses ( $\sim 5 \times 10^9 M_{\odot}$ ) and SFRs  $\sim 15 M_{\odot}/\text{yr}$  as these sources are on average 1 magnitude fainter in the rest-frame UV/optical. Previously Yuma et al. (2010) compared the properties of 3 LAEs and 88 LBGs at  $z \sim 5$  and found that the physical properties of LAEs and LBGs occupy similar parameter spaces. At the same rest-frame UV or optical luminosity, they found no difference in stellar properties (stellar mass, SFR, dust extinction) between their LAEs and LBGs at  $z \sim 5$ .

In figure 10 we show  $f_{esc}$  versus redshift. A definite difference is seen between the escape fractions of narrow-band LAEs and the LBGs at fixed redshift, as the intermediate/narrow band sources have higher mean  $f_{esc}$  and larger range of  $f_{esc}$ . Yet there is essentially no change in the escape fraction for the LBG sources with redshift, nor is there a noticeable difference between the escape fractions of the NB711 and NB816 selected LAEs. The mean, median and range of  $f_{esc}$  for each of the sub-samples is listed in table 5. Our measured escape fractions for the NB816 sources in COSMOS have the same range of escape fractions as the NB816 selected sources studied by Ono et al. (2010) in the Subaru/XMM-Newton Deep Survey field. Our mean escape fraction of 0.37 agrees with their value of 0.36. Our mean and median values are also in agreement with the escape fraction of  $z \sim 2.2$  LAEs studied by Hayes et al. (2010), who found median escape fraction to be higher than 0.32.

In figure 11 we show changes in  $f_{esc}$  with the stellar mass and E(B-V). There is a slight trend with decreasing escape fraction and increasing stellar mass. This is likely due to the trend for more massive and luminous galaxies at higher redshifts to have higher dust extinctions (Bouwens et al. 2009). Plotted versus E(B-V), we see an interesting trend where the sources with the highest extinctions have low escape fractions ( $f_{esc} \sim 0.1$ ), but sources with low extinctions have a range of escape fractions. As extinction increases the range of the escape fraction decreases. This is similar to the trend seen for Ly $\alpha$  sources at  $z \sim 0.1$  (Scarлата et al. (2009), Atek et al. (2009)) and  $z \sim 3$  (Blanc et al. 2011). This may indicate that the same physical conditions/processes (such as gas kinematics, HI covering fraction, and/or galaxy morphology) that inhibit and allow for the escape of Ly $\alpha$  photons at low redshift are similarly occurring in high redshift galaxies too.

In order for this explanation to hold, sources lacking Ly $\alpha$  should be on average more dusty than sources without. For 15 spectroscopic sources with redshifts measured from absorption features, the Ly $\alpha$   $1\sigma$  flux upper limits were calculated (see Table 6). Using these upper limits and the SED SFRs for these sources, the upper limits for the escape fraction for these sources was also determined. The combined escape fraction upper limit for these sources is 0.8%. As expected these sources are offset from the Ly $\alpha$  sample with significantly higher  $\langle E(B-V) \rangle = 0.19$  than the mean for sources with Ly $\alpha$  detections. Interestingly these sources have a slightly higher mean stellar mass  $\langle M_* \rangle = 2 \times 10^{10} M_\odot$  and have  $\langle \text{SFR} \rangle = 169 M_\odot/\text{yr}$  similar to the  $V_J$  LBGs.

## 5. Conclusion

In this paper we present an analysis of a spectroscopic sample of 244 LBGs and LAEs at  $4 < z < 6$  in COSMOS with clear Ly $\alpha$  detections. We have attempted to determine variations in the Ly $\alpha$  properties for these sources and their evolution with redshift. The sources were targeted for spectroscopy using a range of high redshift selection techniques, including LBG, intermediate/narrow-band, photo-z, and IRAC CH2 detections. The goal of the spectroscopic program was to select as complete a sample at  $z > 4$  as possible, for objects brighter than  $z^+ < 25$  and more massive than  $10^{10.5} M_\odot$  (Capak et al. in prep). We measured  $\text{EW}_{Ly\alpha,0}$  and escape fractions for  $B_J, g^+, V_J, r^+, i^+$  LBGs, one intermediate-band and two narrow-band selected samples of LAEs at  $z \sim 4.2$ ,  $z \sim 4.8$ , and  $z \sim 5.6$ . A sub-sample of 153 sources have estimates of  $E(B-V)$ , SFR and  $M_\odot$  from SED modeling. We analyze the variations of the Ly $\alpha$  properties for this subset with respect to these parameterizations of the host galaxies. The results are summarized below.

1) We find that the Ly $\alpha$  EWs remain roughly constant with redshift for both the LBG and intermediate/narrow-band LAEs. While low  $\text{EW}_{Ly\alpha,0}$  are detected for sources at all redshifts, increasingly larger  $\text{EW}_{Ly\alpha,0}$  are measured for sources from samples at higher redshifts. These results are in accordance with the results of Stark et al. 2010 who found a similar trend for LBGs with Ly $\alpha$  at  $z = 3 - 6$ , and with the similar findings of Nilsson et al. (2009) studying LAEs at lower redshifts ( $z=2-3$ ). The speculation is that the change in EW distributions with redshift is the result of increased dust content in LAEs at lower redshifts, but this is yet to be confirmed.

2) No trends were found between Ly $\alpha$  luminosity and stellar mass or SFR. Except for the IA624 LAEs, which on average have lower UV luminosities, the sources tend to have similar stellar masses and SFRs. The mean Ly $\alpha$  luminosities are slightly higher for the LAEs than the LBGs.

3) We find that the Ly $\alpha$  escape fraction of narrow-band LAEs is, on average, higher and has a larger variation than LBG selected sources. The escape fraction does not show a dependence on redshift. Our escape fraction for NB816 LAEs, 0.48, agrees within the errors to escape fraction of NB816 selected sources measured by Ono et al. (2010) in the Subaru/XMM-Newton Deep Survey field (0.36), and the mean escape fraction of Ly $\alpha$  sources (0.32) at  $z = 2.2$  studied by Hayes et al. (2010).

4) Similar to what has been found for sources with Ly $\alpha$  emission at low redshifts, the sources with the highest extinctions show the lowest escape fractions. The range of escape fractions increases with decreasing extinction. This is evidence that the dust extinction is the most important factor affecting the escape of Ly $\alpha$  photons, but at low extinctions other factors such as HI covering fraction and gas kinematics can be just as effective at inhibiting the escape of Ly $\alpha$  photons.

Based in part on data obtained at the W. M. Keck Observatory, which is operated as a scientific partnership among the California Institute of Technology, the University of California, and NASA and was made possible by the generous financial support of the W. M. Keck Foundation.

## REFERENCES

- Arnouts, S., Cristiani, S., Moscardini, L., Matarrese, S., Lucchin, F. et al., 1999, MNRAS, 310, 540
- Ajiki, M., Taniguchi, Y., Fujita, S. S., Shioya, Y., Nagao, T., Murayama, T., Yamada, S., Umeda, K., Komiyama, Y. 2003, AJ, 126, 2091
- Atek, H., Kunth, D., Hayes, M., Ostlin, G., Mas-Hesse, J. M. 2008, A&A, 488, 491
- Atek, H.; Kunth, D.; Schaerer, D.; Hayes, M.; Deharveng, J. M.; -Stlin, G.; Mas-Hesse, J. M., 2009, A&A, 506L, 1A
- Bertin, E., & Arnouts, S. 1996, A&AS, 117, 393
- Blanc, G. A., Adams, J. J., Gebhardt, K., Hill, G. J., Drory, N., Hao, L., Bender, R., Ciardullo, R. et al. 2011, ApJ, 736, 31
- Bouwens, R. J. & Illingworth, G. D., 2006, Nature, 443, 189
- Bouwens, R. J., Illingworth, G. D., Franx, M., Chary, R. R., Meurer, G. R., Conselice, C., J., Ford, H., Giavalisco, M., van Dokkum, P. 2009, ApJ, 705, 936



- Bruzual, G., & Charlot, S. 2003, MNRAS, 344, 1000
- Calzetti, D., Armus, L., Bohlin, R. C., Kinney, A. L., Koornneef, J., & Storchi-Bergmann, T. 2000, ApJ, 533, 682
- Capak, P. et al. in preparation
- Capak, P. et al. 2011, Nature, 470, 233
- Capak, P. et al. 2011, ApJ, 730, 68
- Capak, P., Carilli, C. L., Lee, N., Aldcroft, T., Aussel, H., Schinnerer, E., Wilson, G. W., Yun, M. S. et. al. 2008, ApJ, 681, 53
- Capak, P., Aussel, H., Ajiki, M., McCracken, H. J., Mobasher, B., Scoville, N., Shopbell, P., Taniguchi, Y. et al. 2007, ApJS, 172, 99
- Capak, P. et al. 2004, ApJ, 127, 180
- Cappelluti, N., Brusa, M., Hasinger, G., Comastri, A., Zamorani, G., Finoguenov, A., Gilli, R., Puccetti, S. et al. 2009, A&A, 497, 635
- Charlot, S. & Fall, S. M. 1993, ApJ, 415, 580
- Cowie, L. L., Barger, A. J., Hu, E. M. 2010, ApJ, 711, 928
- Curtis-Lake, E., McLure, R. J., Pearce, H. J., Dunlop, J. S., Cirasuolo, M., Stark, D. P., Almaini, O., Bradshaw, E. J. et al. 2011, arXiv:1110.1722
- Dayal, P., Maselli, A. & Ferrara, A. 2010, MNRAS, 410, 830
- Dijkstra, M., Haiman, Z., Spaans, M. 2006, ApJ, 649, 37D
- Elvis, M., Civano, F., Vignali, C., et al. 2009, ApJS, 184, 158
- Faber, S. M. et al. 2003, Proc SPIE, 4841, 1657
- Finkelstein, Cohen, S. H., Malhotra, S., Rhoads, J. E., Papovich, C., Zheng, Z. Y., & Wang, J. 2009, ApJ, 703, 162
- Furlanetto, Steven R., Zaldarriaga, M. & Hernquist, L. 2006, MNRAS, 365, 1012
- Gawiser, E., van Dokkum, P. G., Gronwall, C., Ciardullo, R., Blanc, G. A., Castander, F. J., Feldmeier, J., Francke, H. et al. 2006 ApJ 642, L13

- Gronwall, C. et al. 2007, *ApJ*, 667, 79
- Guaita, L.; Gawiser, E.; Padilla, N.; Francke, H.; Bond, N. A.; Gronwall, C.; Ciardullo, R. et al. 2010, *ApJ*, 714, 255
- Hansen, M. & Oh, S. P. 2006, *MNRAS*, 367, 979
- Hayes, M., Ostlin, F., Mas-Hesse, J. M., Kunth, D., Leitherer, C., Petrosian, A. 2005, *A&A*, 438, 71
- Hayes, M., Ostlin, G., Schaerer, D. et al. 2010, *Nature*, 464, 562
- Hildebrandt, H., Pielorz, J., Erben, T., van Waerbeke, L., Simon, P., & Capak, P. 2009, *A&A*, 498, 725
- Hu, E. M., Cowie, L. L., Barger, A. J., Capak, P., Kakazu, Y., Trouille, L. 2010, *ApJ*, 725, 394
- Hu E. M. & McMahon, R. G. 1996, *Nature*, 382, 231
- Ikeda, H., Nagao, T.; Matsuoka, K.; Taniguchi, Y.; Shioya, Y.; Trump, J. R.; Capak, P.; Comastri, A. et al. 2011, *ApJ*, 728, L25
- Ilbert, O., Arnouts, S., McCracken, H. J., Bolzonella, M., Bertin, E et al., 2006, *A&A*, 457, 841
- Ilbert, O. et al. 2009, *ApJ*, 690, 1236
- Ilbert, O. et al. 2010, *ApJ*, 709, 644
- Iwata, I., Ohta, K., Tamura, N., Ando, M., Wada, S., Watanabe, C., Akiyama, M., & Aoki, K. 2003, *PASJ*, 55, 415
- Kashikawa, N., Shimasaku, K.; Malkan, M. A.; Doi, M.; Matsuda, Y.; Ouchi, M.; Taniguchi, Y.; Ly, C. 2006, *ApJ*, 648, 7
- Kennicutt, R. C. 1998, *ARA&A*, 36, 189
- Kornei, K. A., Shapley, A. E., Erb, D. K., Steidel, C. C., Reddy, N. A., Pettini, M., Bogosavljevic, M. 2010, *ApJ*, 711, 693
- Krug, H., Veilleux, S., Tilvi, V., Malhotra, S., Rhoads, J., Hibon, P., Swaters, R., Probst, R. et al. 2011, arXiv:1106.6055
- Kunth, D., Leitherer, C., Mas-Hesse, J. M., Ostlin, G., Petrosian, A. 2003, *ApJ*, 597, 263

- Lehmer, B. D.; Alexander, D. M.; Geach, J. E.; Smail, I.; Basu-Zych, A.; Bauer, F. E.; Chapman, S. C.; Matsuda, Y. et al. 2009, *ApJ*, 691, 687
- Malhotra, S. & Rhoads, J. E. 2004, *ApJ*, 617, L5
- Malhotra, S., Wang, J. X.; Rhoads, J. E.; Heckman, T. M.; Norman, C. A. 2003, *ApJ*, 585, 25
- Markwardt, C. B. 2008, "Non-Linear Least Squares Fitting in IDL with MPFIT," in proc. Astronomical Data Analysis Software and Systems XVIII, Quebec, Canada, ASP Conference Series, Vol. 411, eds. D. Bohlender, P. Dowler & D. Durand (Astronomical Society of the Pacific: San Francisco), p. 251-254
- Masters, D. & Capak, P. 2011, *PASP*, 123, 638
- Mas-Hesse, J. M., Kunth, D., Tenorio-Tagle, G., Leitherer, C., Terlevich, R. J., Terlevich, E. 2003, *ApJ*, 598, 858
- McCracken, H., Milvang-Jensen, B., Dunlop, J., Franx, M., Fynbo, J. P. U., le Fevre, O., Holt, J., Caputi, K. I., et al. 2012, arXiv:1204.6586v1
- Mesinger, A. & Furlanetto S. R. 2008, *MNRAS*, 386, 1990
- Murayama, T., Taniguchi, Y., Scoville, N. Z., Ajiki, M., Sanders, D. B., Mobasher, B., Aussel, H., Capak, P., et al. 2007, *ApJS*, 172, 523
- Neufeld, D. A. 1991, *ApJ*, 370, 85
- Nilsson, K. K., Tapken, C., Moller, P., Freudling, W., Fynbo, J. P. U., Meisenheimer, K., Laursen, P., Ostlin, G. 2009, *A&A*, 498, 13
- Ono, Y., Ouchi, M., Shimasaku, K., et al. 2010, *MNRAS*, 402, 1580
- Ono, Y., Ouchi, M., Shimasaku, K., et al. 2010, *ApJ*, 724, 1524
- Ono, Y., Ouchi, M., Mobasher, B., Dickinson, M., Penner, K., Shimasaku, K., Weiner B. J., Kartaltepe, J. S. et al., 2011, arXiv:1107.3159
- Ostlin, G., Hayes, M., Kunth, D., Mas-Hesse, J. M., Leitherer, C., Petrosian, A., Atek, H. 2009, *AJ*, 138, 9230
- Osterbrock, D. E. 1989, *Astrophysics of Gaseous Nebulae and Active Galactic Nuclei* (Mill Valley: University Science Books)

- Ota, K.; Iye, M.; Kashikawa, N.; Shimasaku, K.; Kobayashi, M.; Totani, T.; Nagashima, M.; Morokuma, T. et al. 2008, *ApJ*, 677, 12
- Ouchi, M. et al. 2010, *ApJ*, 723, 869
- Ouchi, M. et al. 2008, *ApJS*, 176, 301
- Ouchi, M. et al. 2004, *ApJ*, 611, 660
- Pentericci, L., Fontana, A., Vanzella, E., Castellano, M., Grazian, A., Dijkstra, M., Boutsia, K., Cristiani, S et al. 2011, *ApJ*, 743, 132
- Rhoads, J. E. & Malhotra, S. 2001, *ApJ*, 563, 5
- Scarlata, C., Colbert, J., Teplitz, H. I., Panagia, N., Hayes, M., Siana, B., Rau, A., Francis, P. et al 2009, *ApJ*, 704, 98
- Schaerer, D. 2007, IAC Winterschool, Lecture on Primeval Galaxies, astro-ph/0706.0139
- Schenker, M. A., Stark, D.P., Ellis, R.S., Robertson, B.E., Dunlop, J.S., McLure, R.J., Kneib, J.-P., Richard, J. 2011, arXiv:1107.1261
- Scoville et al. 2007, *ApJS*, 172, 38
- Shapley, A. E., Steidel C. C., Adelberger K. L., Dickinson M., Giavalisco M., Pettini M., 2011 *ApJ* 562, 95
- Shapley, A. E., Steidel, C. C., Pettini, M., Adelberger, K. L. 2003, *ApJ*, 588, 65
- Shioya, Y., Taniguchi, Y., Sasaki, S. S., Nagao, T., Murayama, T., Saito, T., Ideue, Y., Nakajima, A. et al. 2009, *ApJ*, 696, 546
- Stark, D. P.; Ellis, R. S. & Ouchi, M. 2011, *ApJ*, 728, 2
- Stark, D. P., Ellis, R. S., Chiu, K., Ouchi, M., Bunker, M. 2010, *MNRAS*, 408, 628
- Steidel, C. C., Erb, D. K., Shapely, A. E., Pettini, M., Reddy, N. A., Bogosavljevic, M., Rudie, G. C., Rakic, O. 2010, *ApJ*, 717, 289
- Steidel, C. et al. 1999, *ApJ*, 519, 1
- Taniguchi, Y., Ajiki, M., Nagao, T., Shioya, Y., Murayama, T., Kashikawa, N., Kodaira, K., Kaifu, N., et al. 2005, *PASJ*, 57, 165

- Tapken, C., Appenzeller, I., Noll, S., Richling, S., Heidt, J., Meinkohn, E., Mehlert, D. 2007, *A&A*, 467, 63T
- Tilvi, V.; Rhoads, J. E.; Hibon, P.; Malhotra, S.; Wang, J.; Veilleux, S.; Swaters, R.; Probst, R. 2010, *ApJ*, 721, 1853
- Verhamme, A., Schaerer, D., Maselli, A. 2006, *A&A*, 460, 397
- Verhamme, A., Schaerer, Atek, H., Tapken, C. 2008, *A&A*, 491, 89
- Wang, J. X.; Rhoads, J. E.; Malhotra, S.; Dawson, S.; Stern, D.; Dey, A.; Heckman, T. M.; Norman, C. A.; Spinrad, H. 2004, *ApJ*, 608, 21
- Yuma, S., Ohta, K., Yabe, K., Shimasaku, K., Yoshida, M., Ouchi, M., Iwata, I., & Sawicki, M. 2010, *ApJ*, 720, 1016
- Zheng, Z. Y.; Wang, J. X.; Finkelstein, S. L.; Malhotra, S.; Rhoads, J. E.; Finkelstein, K. D. 2010, *ApJ*, 718, 52

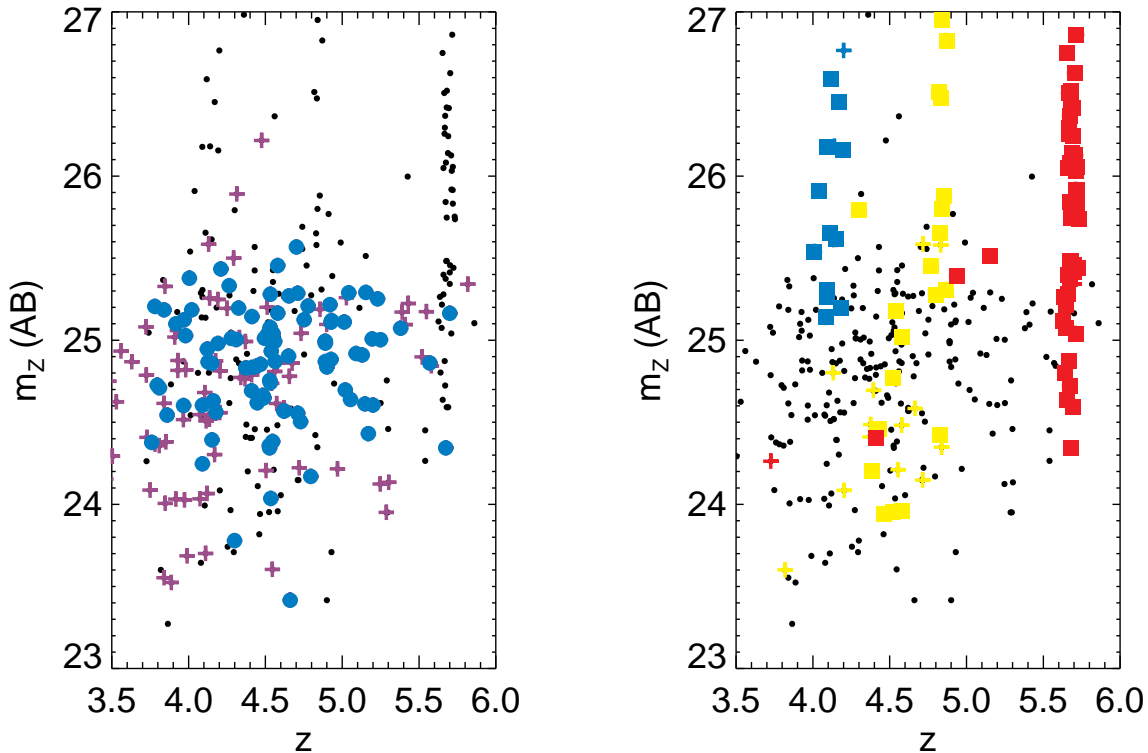


Fig. 1.— Redshift versus apparent  $z$  (AB) magnitude. In both panels the black dots represent all sources with measured spectroscopic redshifts. *Left Panel:* The  $m_z$ -redshift distribution for LBG selected sources with (without) Ly $\alpha$  as blue circles (purple crosses). *Right Panel:* The  $m_z$ -redshift distribution for narrow-band selected sources with (without) Ly $\alpha$  detections. Blue squares represent the IA624 sources, the yellow squares (crosses) the NB711 sources, and the red squares (crosses) the NB816 sources. The four low- $z$  NB816 outliers are from the relaxed color-cut criteria used to select the LAEs at  $z \sim 5.6$ , and would not have made the more stringent cut from Murayama et al. (2007). For both the LBG and intermediate/narrow band selected sources, Ly $\alpha$  detection shows no bias by either redshift, or magnitude, and hence luminosity, with regards to Ly $\alpha$  detection down to the detection limits of the spectroscopy. However, the narrow-band sources with Ly $\alpha$  are on average 0.8 magnitudes fainter than the LBG sources with Ly $\alpha$ .

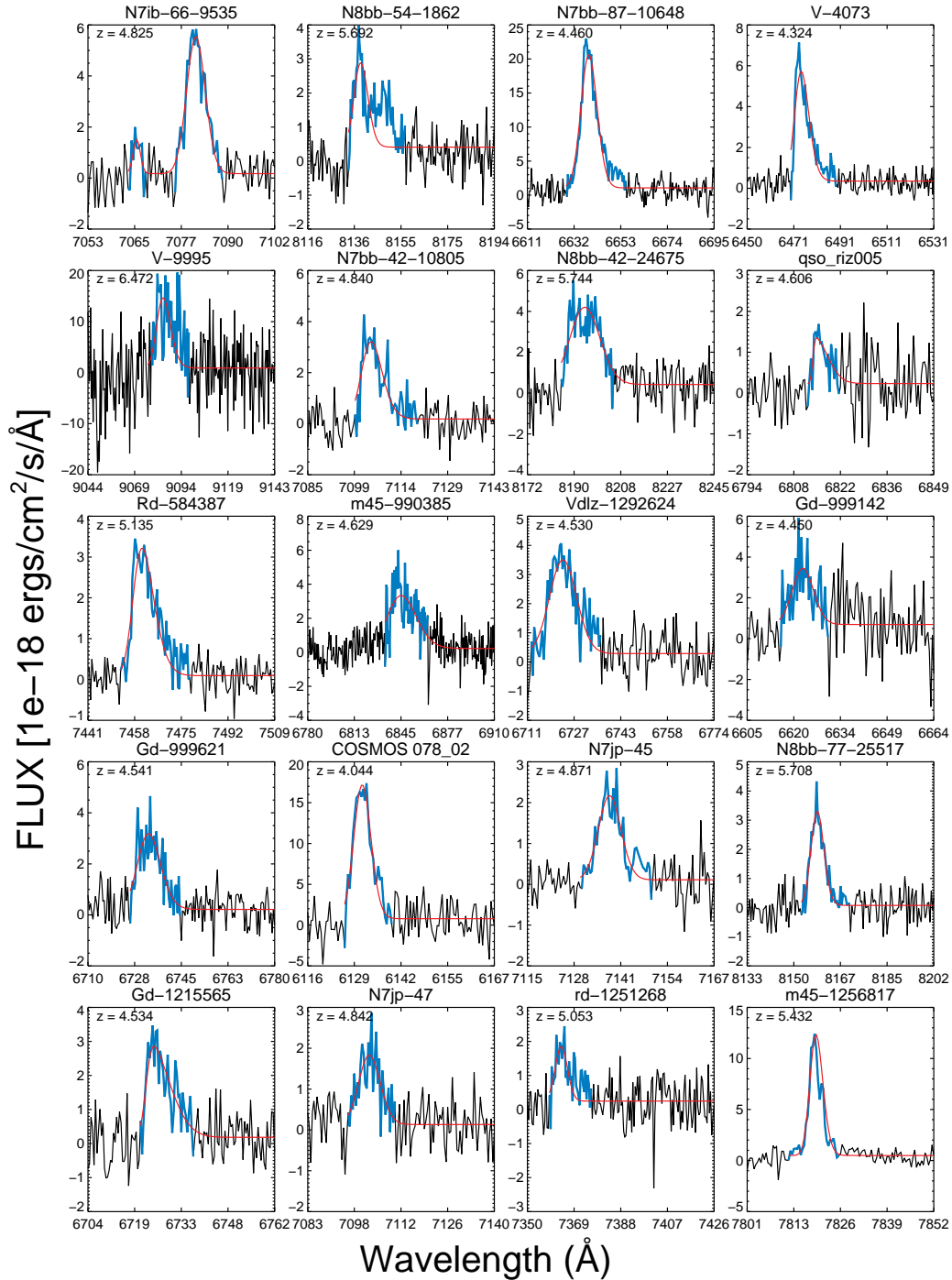


Fig. 2.— Spectra of 20 sources randomly chosen, showing the Ly $\alpha$  emission feature. The blue line highlights the region of each spectrum used for the numerical integration. The red line shows the best skewed Gaussian fit to the data. The 1D and 2D spectra will be shown in the data paper (Capak et al. in prep).

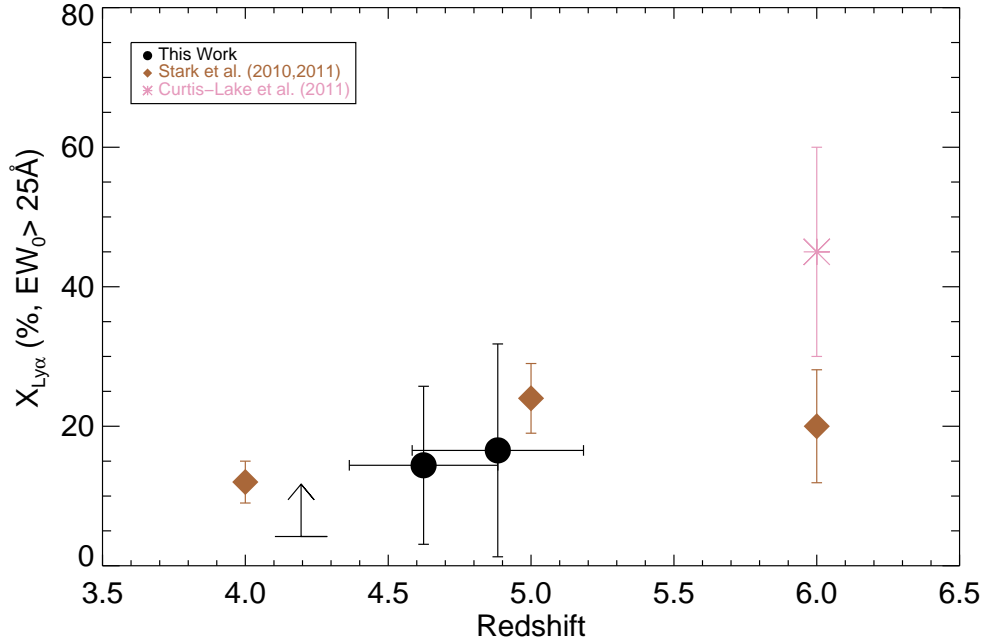


Fig. 3.— The fraction of LBGs with  $\text{EW}_{\text{Ly}\alpha,0} > 25$  and  $-21.75 < M_{UV} < -20.25$  plotted versus mean redshift. Plotted is the fraction of  $B_J + g^+$  LBGs (lower limit) at  $z \sim 4.2$ ,  $V_J$  LBGs (filled circle) at  $z \sim 4.6$ , and  $r^+$  LBGs (filled circle) at  $z \sim 5.0$ . Other fractions are taken from Curtis Lake et al. (2011) and Stark et al. (2010, 2011). Our measured fractions do not point to an evolution of the Ly $\alpha$  fraction of luminous LBGs over the redshift range  $3.8 < z < 5.5$  but are consistent with the fractions reported in Stark et al. (2010, 2011).



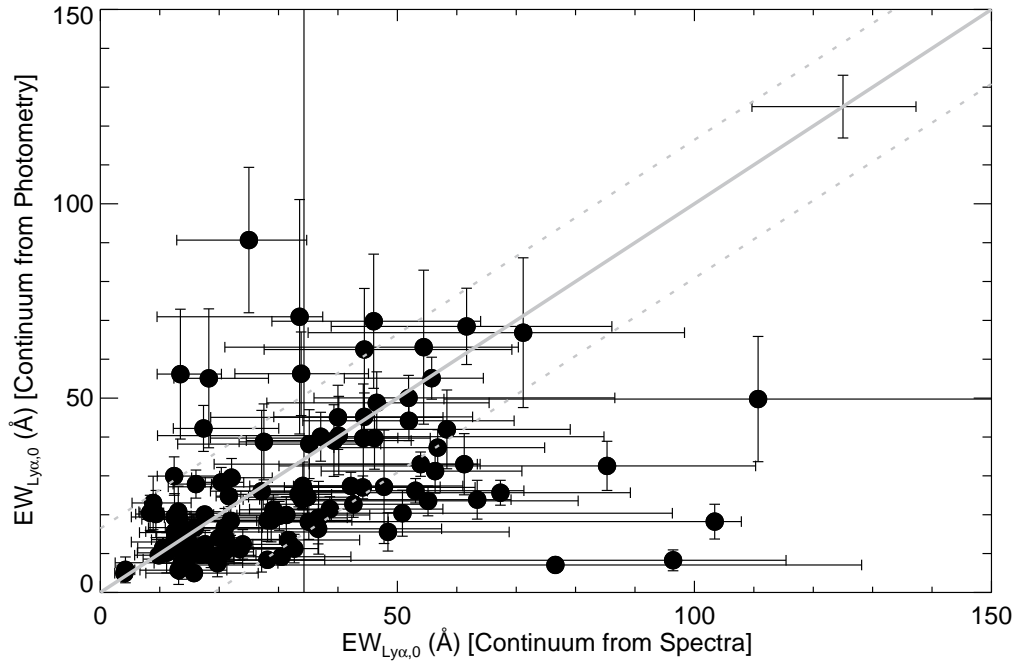


Fig. 4.— The flux calibrated rest frame  $Ly\alpha$  equivalent width comparison between continuums measured using the spectra, and continuums measured using the photometry. The solid gray line shows a 1 to 1 correspondence, and the dashed gray lines show the  $1\sigma$  deviation from a 1 to 1 correspondence determined from the mean errors on both equivalent widths. The mean equivalent width error bar is plotted in the upper right corner.

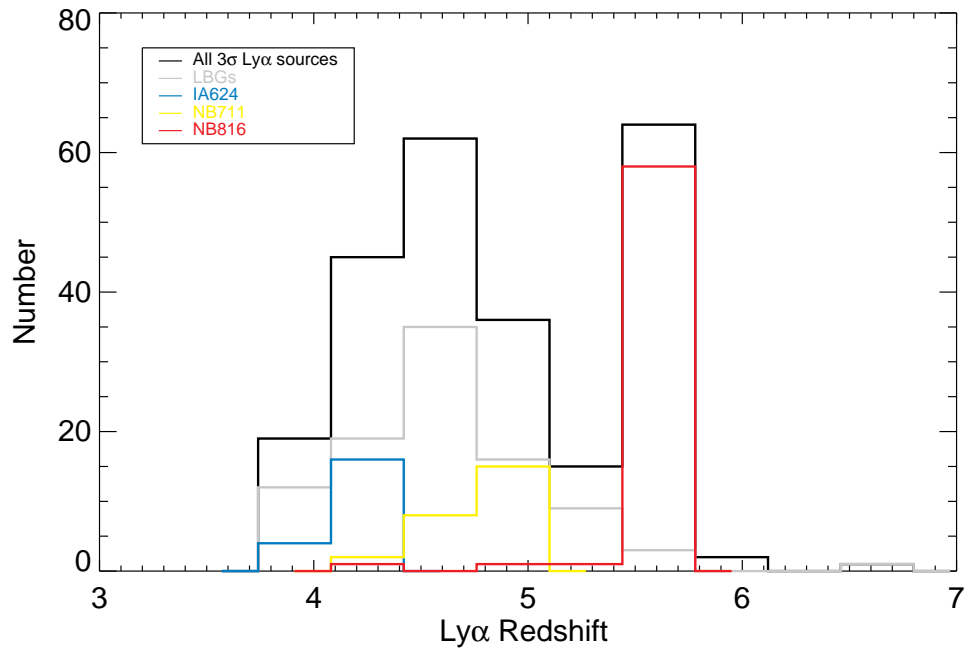


Fig. 5.— Redshift distribution of the Ly $\alpha$  sample. Sources are divided into the following categories: All sources (black), LBGs (gray), IA624 (blue), NB711 (yellow), NB816 (red). The source selection for each of these sub-samples is described in section 2.2

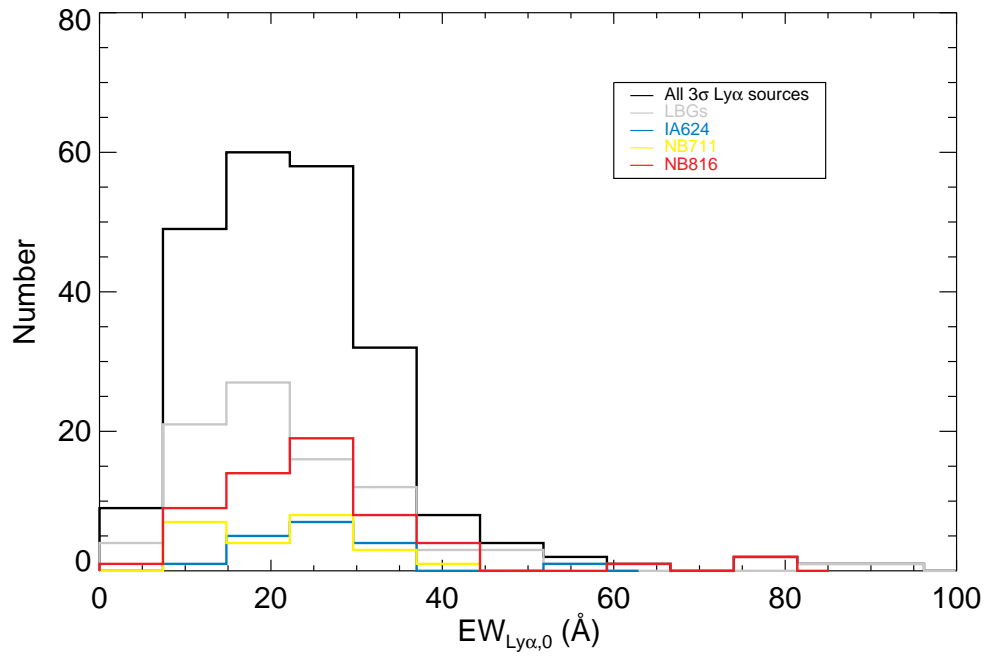


Fig. 6.— The flux calibrated rest frame Ly $\alpha$  equivalent width distribution. Sources are divided into the following categories: All sources (black), LBGs (gray), IA624 (blue), NB711 (yellow), NB816 (red). The LBGs have a lower mean EW than the narrow-band LAEs, which may be due to the narrow-band LAEs being on average fainter than the LBGs by 0.8 magnitudes.

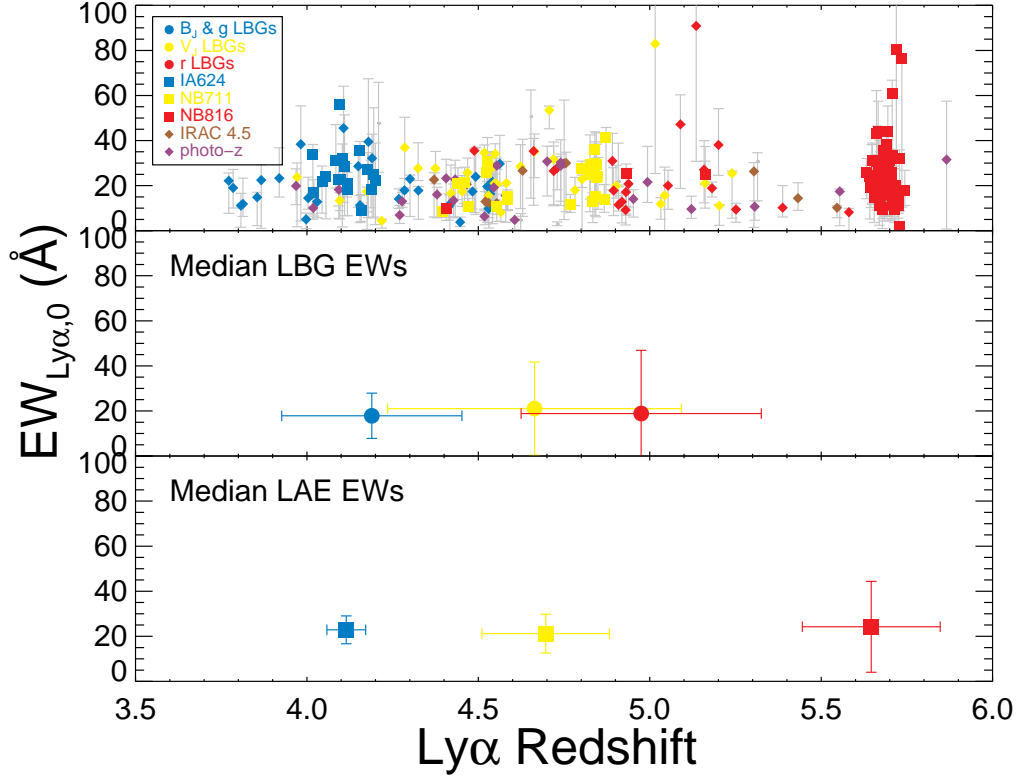


Fig. 7.— The change in rest frame Ly $\alpha$  equivalent width as a function of redshift. The median EW<sub>Ly $\alpha$ ,0</sub> of both the LBGs and LAEs show no evolution with redshift. The LAEs tend to have slightly higher EWs than the LBGs at similar redshifts. *Top Panel:* EW<sub>Ly $\alpha$ ,0</sub> versus redshift for the entire sample. *Middle Panel:* The median values of EW<sub>Ly $\alpha$ ,0</sub> and redshift for each of the LBG sub-samples. The median EW<sub>Ly $\alpha$ ,0</sub> shows no evolution with redshift for the LBG selected sources, though the sample variance increases with redshift. *Bottom Panel:* The median values of EW<sub>Ly $\alpha$ ,0</sub> versus redshift for each of the intermediate/narrow band LAEs. Similar to the LBGs, the median EW<sub>Ly $\alpha$ ,0</sub> shows no evolution with redshift. The EW, redshift error bars are the sample variances. The filled circles represent the LBG sources, and are colored as follows: The blue-dots represent B<sub>J</sub> and g<sup>+</sup> LBGs, yellow-dots the V<sub>J</sub> LBGs, red dots the r<sup>+</sup> LBGs and violet dots the i<sup>+</sup> LBGs. The filled squares represent the narrow-band selected LAEs with the blue-squares for the z  $\sim$  4.2 sources, the yellow-squares for the NB711 sources and the red-squares for the NB816 sources. The brown-diamonds represent the other selected sources.

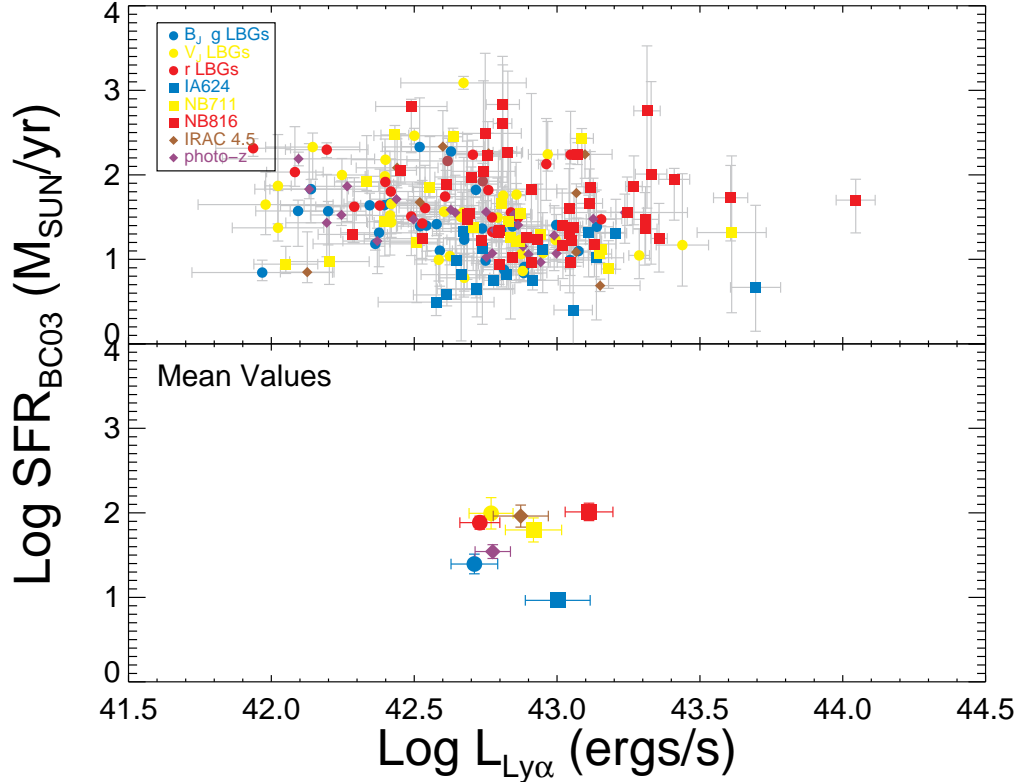


Fig. 8.— The flux calibrated Ly $\alpha$  luminosity plotted versus SFR estimated from BC03 galaxy models. *Top Panel:* All 153 sources with measured SFRs. *Bottom Panel:* The mean and error on the mean of the Ly $\alpha$  luminosity and SFR for each of the sub-samples. No particularly strong trends are found between Ly $\alpha$  luminosity, and SFR. The LAEs on average have higher Ly $\alpha$  luminosities. All have similar distributions of SFR except for the IA624 sources, which have  $\sim 1$  magnitude fainter UV luminosities than the rest of the LBGs and LAEs, and slightly lower SFRs. The symbols are the same as in figure 7.

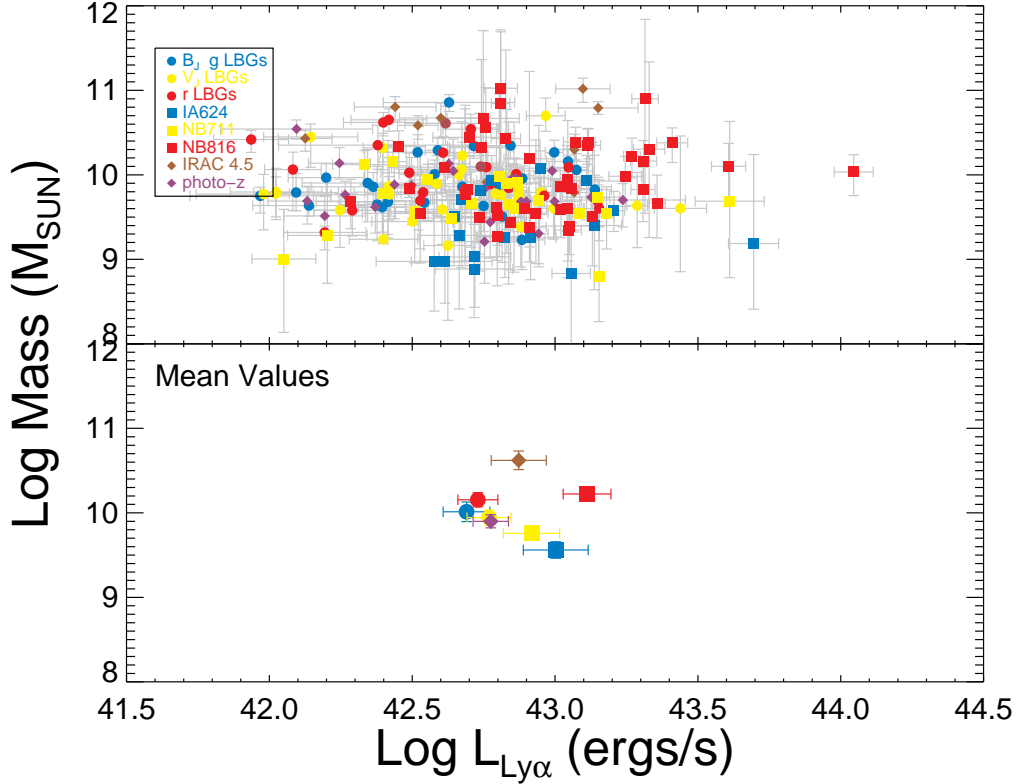


Fig. 9.— The flux calibrated  $\text{Ly}\alpha$  luminosity plotted versus stellar mass estimated from BC03 galaxy models in Ilbert et al. (2010). *Top Panel:* All 153 sources with measured stellar masses. *Bottom Panel:* The mean and error on the mean of the  $\text{Ly}\alpha$  luminosity and stellar mass for each of the sub-samples. Similar to the figure 7, no particularly strong trends are found between  $\text{Ly}\alpha$  luminosity and stellar mass. The LBGs and LAEs all have very similar distributions of stellar mass, except the IA624 sources which are slightly less massive. The symbols are the same as in figure 7.

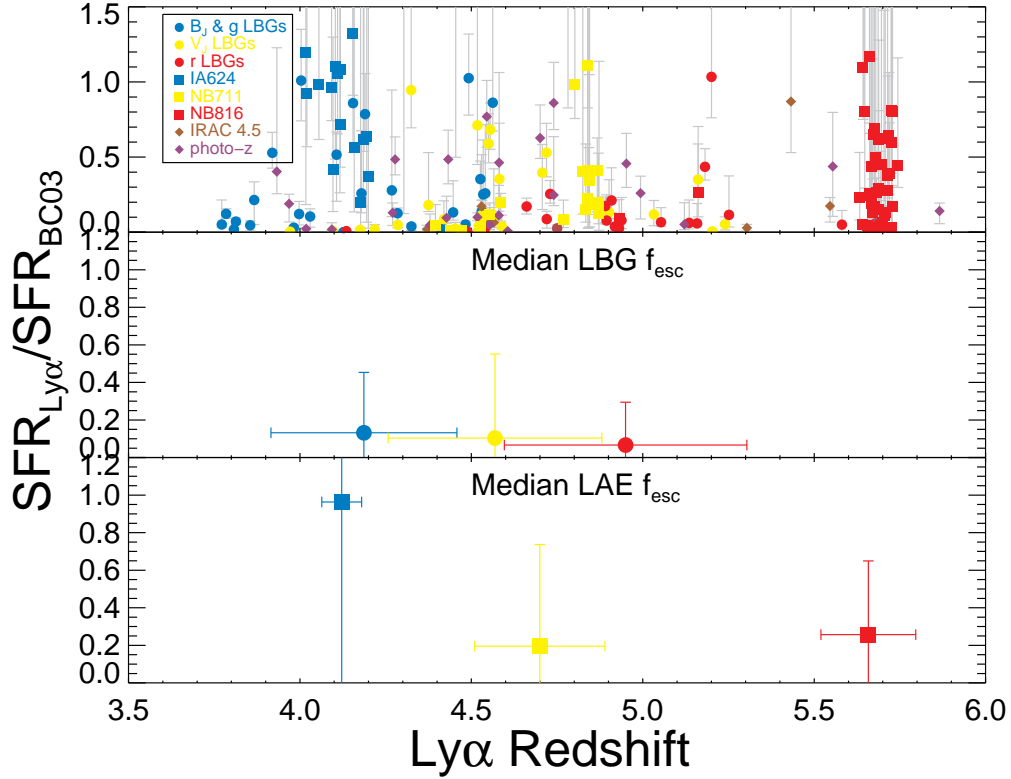


Fig. 10.— Estimated Ly $\alpha$  escape fraction plotted versus redshift. The symbols are the same as in figure 6. *Top Panel:* All 153 sources with SFRs from SED fitting. *Middle Panel:* The median escape fractions of the LBGs, with the error bars showing the sample variances. *Bottom Panel:* The median escape fractions of the LAEs, with the error bars showing the sample variances. The majority of sources indicate escape fractions at or below 50%. The escape fractions are highly uncertain due to uncertainties in the SED SFRs. The LAEs have the largest uncertainties due to the faintness of these sources which results in larger photometric errors and greater uncertainties in the physical properties derived from the SED fits. The sources with the highest escape fractions are narrow/intermediate band selected LAEs. The median escape fraction for the entire sample is 18%. The data is consistent with no change in escape fraction with redshift for the LBGs. The NB711 and NB816 LAEs have similar mean and median escape fraction twice that of the LBGs. The IA624 sources have extremely high escape fractions, with mean and median values up to and exceeding  $f_{esc} \sim 1$ . The high values are likely attributable to the uncertainties of the SED derived SFRs as these sources were chosen to be faint,  $m_z > 25(AB)$ . The top panel shows the entire sample, the middle panel shows the median values for the LBGs, and the bottom panel shows the median values for the narrow band LAEs.

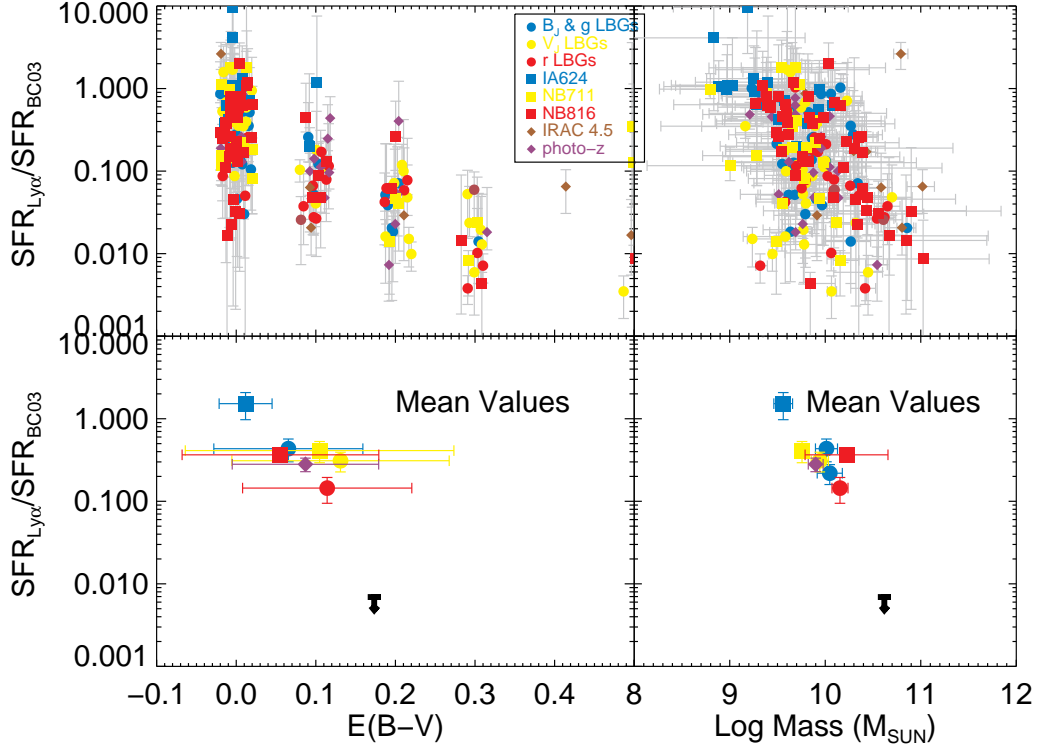


Fig. 11.— *Left*: Estimated Ly $\alpha$  escape fraction plotted versus extinction estimated from BC03 models. The E(B-V) values are discrete at 0.0, 0.1, 0.2, 0.3, 0.4, and 0.5. To make the points more visible a random scatter of 0.02 has been added to their values. This shows that while extinction inhibits the escape of Ly $\alpha$  photons, there are other factors that govern Ly $\alpha$  escape such as HI covering fraction, and gas kinematics, that can inhibit its escape even when there is little dust. *Right*: The Ly $\alpha$  escape fraction is plotted versus stellar mass estimated from BC03 models. There is a slight trend between stellar mass and escape fraction, with higher stellar mass sources having lower escape fractions. The black arrows represent the combined upper limit on the escape fraction for 15 spectroscopic sources with only  $1\sigma$  Ly $\alpha$  flux upper limits. The E(B-V) and  $M_*$  values plotted are the mean values for these sources. The other symbols are the same as in figure 7. The panels on the lower left and right show the mean values for each of the source types. The error bars on the mean E(B-V) values represents the sample variance, while the mean  $f_{esc}$  and  $M_*$  error bars are the errors on the means.



Table 1. DEIMOS Sources with Ly $\alpha$  Emission

Type	# > 3 $\sigma$ Ly $\alpha$	# with EW $_{Ly\alpha,0} > 25\text{\AA}$	AGN with > 3 $\sigma$ Ly $\alpha$	# Observed
All LBGs:	95	32	1	380
$B_J$ LBGs:	10	3	0	49
$g^+$ LBGs:	21	3	0	158
$V_J$ LBGs:	39	16	1	101
$r^+$ LBGs:	23	9	0	56
$i^+$ LBGs:	2	1	0	16
IA624:	20	9	2	26
NB711:	25	9	1	42
NB816:	61	26	0	73
IRAC4.5:	11	3	1	55
Photo-z:	22	5	0	58
Other:	5	0	1	10
Total:	244	84	7	644

Table 2. Ly $\alpha$  Emission

Source	RA J2000	DEC J2000	Type	z	Flux (1e-18 ergs/cm <sup>2</sup> /s)	EW <sub>Ly<math>\alpha</math>,0</sub> (Å)	FWHM (Å)	Skew
N7ib-66-9535	149.967958	2.258167	NB711	4.825	30.1± 6.00	24.9 <sup>+6.11</sup> <sub>-16.48</sub>	5.72± 1.47	0.80± 0.01
N8bb-54-1862	149.971875	2.118167	NB816	5.692	19.8± 7.60	5.3 <sup>+2.63</sup> <sub>-4.10</sub>	7.23± 1.79	1.12± 0.10
N8bb-54-20446	149.933583	2.014083	NB816	5.688	15.5± 2.62	27.8 <sup>+11.65</sup> <sub>-13.58</sub>	9.01± 2.22	1.51± 0.05
N8bb-66-30821	149.942250	2.128583	NB816	5.666	18.1± 2.18	24.9 <sup>+4.54</sup> <sub>-1.78</sub>	9.76± 2.34	2.34± 0.10
N8jp-66-40	149.977208	2.254611	NB816	5.688	13.8± 2.10	20.0 <sup>+7.44</sup> <sub>-13.25</sub>	6.80± 1.89	0.92± 0.07
N8jp-66-41	149.978292	2.177611	NB816	5.662	31.7± 4.83	15.9 <sup>+6.03</sup> <sub>-5.55</sub>	6.26± 1.56z	0.52± 0.07
B-8431	149.941292	2.057139	<i>B<sub>J</sub></i> LBG	4.150	31.6± 8.99	28.6 <sup>+5.76</sup> <sub>-18.22</sub>	9.13± 2.26	2.31± 0.10
N8bb-37-10756	150.790833	1.897889	NB816	5.705	46.6± 5.45	21.4 <sup>+2.98</sup> <sub>-14.10</sub>	4.54± 0.15	0.98± 0.01
N8bb-37-33891	150.775583	1.795306	NB816	5.680	31.7± 2.56	19.8 <sup>+10.58</sup> <sub>-9.05</sub>	7.10± 1.81	1.27± 0.01
N8bb-49-19547	150.754792	2.043361	NB816	5.682	73.5± 9.14	28.2 <sup>+4.51</sup> <sub>-11.81</sub>	9.98± 2.39	0.75± 0.30
N8bb-49-20883	150.779167	2.037833	NB816	5.676	116.0± 16.01	19.2 <sup>+10.44</sup> <sub>-10.90</sub>	6.41± 1.94	1.99± 0.01
N8jp-37-103	150.757583	1.836500	NB816	5.695	48.0± 9.86	29.4 <sup>+10.74</sup> <sub>-15.95</sub>	9.30± 3.14	0.64± 0.01
N8jp-37-104	150.772208	1.861389	NB816	5.694	60.7± 11.38	44.0 <sup>+11.43</sup> <sub>-30.73</sub>	9.90± 2.91	1.89± 0.01
B-10208	150.749458	1.824611	<i>B<sub>J</sub></i> LBG	4.190	38.1± 6.79	32.2 <sup>+10.66</sup> <sub>-26.46</sub>	9.07± 2.79	1.66± 0.01
V-4084	150.781250	1.906083	<i>V<sub>J</sub></i> LBG	4.782	83.0± 6.90	18.0 <sup>+5.64</sup> <sub>-6.84</sub>	8.85± 2.92	1.45± 0.03
N7bb-87-10648	150.512667	2.588472	NB711	4.460	172.0± 14.03	21.2 <sup>+6.96</sup> <sub>-9.21</sub>	8.16± 2.17	0.89± 0.02
N7bb-88-24551	150.363125	2.536167	NB711	4.586	14.7± 2.46	15.2 <sup>+5.91</sup> <sub>-5.91</sub>	8.18± 1.97	0.91± 0.08
N8bb-87-6788	150.438125	2.599361	NB816	5.673	21.9± 3.28	23.1 <sup>+11.96</sup> <sub>-11.87</sub>	6.95± 1.69	3.13± 0.10
N8bb-88-26173	150.379458	2.518333	NB816	5.690	19.2± 2.27	38.5 <sup>+5.04</sup> <sub>-29.93</sub>	6.14± 1.62	1.53± 0.15
N8bb-88-29007	150.365708	2.501694	NB816	5.696	24.3± 2.38	31.4 <sup>+10.32</sup> <sub>-13.40</sub>	11.92± 3.16	1.53± 0.05
N8bb-88-33344	150.291917	2.474778	NB816	5.681	17.8± 3.50	35.5 <sup>+4.66</sup> <sub>-24.43</sub>	12.12± 2.97	0.01± 0.01
B-6014	150.432125	2.572528	<i>B<sub>J</sub></i> LBG	4.526	48.4± 3.54	19.6 <sup>+5.25</sup> <sub>-10.92</sub>	6.97± 1.72	1.15± 0.02
B-9848	150.475625	2.540722	<i>B<sub>J</sub></i> LBG	4.268	21.8± 2.21	14.1 <sup>+4.47</sup> <sub>-4.24</sub>	5.73± 1.64	1.04± 0.08
N7bb-100-45206	150.297208	2.634806	NB711	4.802	60.4± 2.44	27.5 <sup>+3.36</sup> <sub>-8.30</sub>	8.45± 2.56	1.81± 0.01
N7ib-89-7876	150.129875	2.598083	NB711	4.826	106.7± 12.96	29.3 <sup>+13.21</sup> <sub>-15.25</sub>	4.67± 1.11	1.70± 0.03
Vc-89-8485	150.214958	2.582667	<i>V<sub>J</sub></i> LBG	5.314	12.0± 1.09	30.6 <sup>+3.99</sup> <sub>-17.38</sub>	10.21± 3.02	2.75± 0.05
N7bb-39-5654	150.497792	1.936917	NB711	4.441	13.8± 1.55	21.0 <sup>+6.93</sup> <sub>-7.17</sub>	9.29± 2.23	1.58± 0.07
N8bb-38-6719	150.690250	1.926667	NB816	5.633	54.2± 3.68	25.9 <sup>+6.11</sup> <sub>-11.72</sub>	10.49± 3.60	0.96± 0.01
N8ib-39-8551	150.536667	1.912556	NB816	5.676	37.5± 1.98	24.9 <sup>+13.18</sup> <sub>-9.49</sub>	7.67± 2.46	1.35± 0.03
N8ib-39-551	150.539750	1.951583	NB816	4.407	23.4± 5.03	9.8 <sup>+1.65</sup> <sub>-5.22</sub>	5.05± 1.34	2.06± 0.04
B-1441	150.678875	1.947111	<i>B<sub>J</sub></i> LBG	4.004	49.8± 9.25	14.5 <sup>+9.25</sup> <sub>-4.94</sub>	8.16± 2.27	1.90± 0.05
B-6412	150.596375	1.897556	<i>B<sub>J</sub></i> LBG	3.807	10.1± 4.57	11.2 <sup>+5.47</sup> <sub>-9.69</sub>	3.01± 1.03	1.26± 0.96
B-3516	150.543292	1.927000	<i>B<sub>J</sub></i> LBG	4.179	41.1± 9.79	39.5 <sup>+27.98</sup> <sub>-33.63</sub>	5.59± 1.41	1.36± 0.04
V-8065	150.481917	1.881667	<i>V<sub>J</sub></i> LBG	4.518	23.2± 4.77	34.6 <sup>+3.48</sup> <sub>-25.51</sub>	6.34± 1.64	0.80± 0.05
N7bb-16-16904	150.296500	1.560389	NB711	4.845	28.5± 2.41	23.5 <sup>+14.99</sup> <sub>-11.23</sub>	6.08± 1.64	1.47± 0.02
N7bb-17-4622	150.161000	1.609806	NB711	4.395	18.7± 2.62	8.5 <sup>+0.28</sup> <sub>-2.57</sub>	6.93± 0.83	0.92± 1.31
N7bb-17-5717	150.126792	1.606000	NB711	4.844	62.9± 3.54	29.3 <sup>+14.10</sup> <sub>-13.71</sub>	6.61± 1.70	1.55± 0.02
N8bb-16-2464	150.243375	1.611889	NB816	5.688	18.4± 2.47	28.2 <sup>+1.64</sup> <sub>-21.68</sub>	5.09± 1.31	1.39± 0.03
N8bb-16-3055	150.231333	1.608556	NB816	5.670	18.5± 1.38	22.2 <sup>+7.25</sup> <sub>-6.04</sub>	9.94± 2.47	8.02± 11.16
N8bb-16-12770	150.247083	1.555444	NB816	5.660	8.2± 1.04	24.5 <sup>+9.18</sup> <sub>-10.96</sub>	6.49± 1.70	1.54± 0.23
N8bb-17-10353	150.191875	1.576583	NB816	5.663	37.4± 3.95	30.9 <sup>+15.62</sup> <sub>-14.10</sub>	12.07± 2.93	2.67± 0.08
V-4073	150.261250	1.590667	<i>V<sub>J</sub></i> LBG	4.324	41.2± 3.27	27.7 <sup>+11.34</sup> <sub>-5.44</sub>	11.47± 3.45	10.64± 3.52
V-2597	150.144250	1.604472	<i>V<sub>J</sub></i> LBG	4.902	18.6± 1.74	19.9 <sup>+9.11</sup> <sub>-5.43</sub>	14.60± 3.40	1.67± 0.06
V-4147	150.222250	1.590667	<i>V<sub>J</sub></i> LBG	4.454	138.9± 29.28	-99.9 <sup>+0.00</sup> <sub>-0.00</sub>	5.51± 1.33	1.66± 0.36
N8bb-30-13181	149.942208	1.731528	NB816	5.717	33.2± 3.18	-99.9 <sup>+0.00</sup> <sub>-0.00</sub>	8.29± 2.40	1.53± 0.03

Table 2—Continued

Source	RA J2000	DEC J2000	Type	z	Flux (1e-18 ergs/cm <sup>2</sup> /s)	EW <sub>Ly<math>\alpha</math>,0</sub> (Å)	FWHM (Å)	Skew
N8bb-30-18324	149.905667	1.710778	NB816	5.162	22.5± 1.28	25.0 <sup>+12.38</sup> <sub>-4.51</sub>	10.61± 3.79	1.83± 0.02
N8jp-18-31	149.930292	1.598000	NB816	5.648	58.9± 5.70	24.2 <sup>+14.01</sup> <sub>-12.49</sub>	10.43± 3.70	0.40± 0.01
N8jp-18-37	149.967208	1.623111	NB816	5.724	19.6± 2.21	11.4 <sup>+3.78</sup> <sub>-5.88</sub>	7.31± 1.94	0.52± 0.02
B-16566	149.934792	1.638083	B <sub>J</sub> LBG	4.285	19.3± 1.94	17.9 <sup>+5.28</sup> <sub>-5.85</sub>	9.32± 2.33	1.68± 0.20
B-9885	149.885292	1.701667	B <sub>J</sub> LBG	4.483	12.4± 2.33	17.4 <sup>+1.30</sup> <sub>-7.80</sub>	7.25± 1.80	0.71± 0.03
V-1135	149.939042	1.617556	V <sub>J</sub> LBG	4.453	12.6± 2.01	17.4 <sup>+7.06</sup> <sub>-6.60</sub>	10.30± 2.77	4.09± 0.40
V-9995	149.960083	1.527694	V <sub>J</sub> LBG	6.472	155.4± 59.48	15.7 <sup>+1.41</sup> <sub>-13.11</sub>	10.04± 2.55	1.17± 0.04
V-11671	149.925333	1.683472	V <sub>J</sub> LBG	4.707	33.0± 1.97	53.4 <sup>+1.86</sup> <sub>-8.22</sub>	7.93± 0.84	0.79± 0.94
N7bb-28-9956	150.361125	1.757306	NB711	4.527	59.5± 5.52	30.7 <sup>+10.72</sup> <sub>-8.75</sub>	11.23± 2.84	0.99± 0.01
N8bb-27-22829	150.398500	1.685611	NB816	5.663	14.7± 6.57	13.6 <sup>+1.93</sup> <sub>-10.96</sub>	7.88± 1.98	2.09± 0.08
N8bb-28-12615	150.379625	1.722333	NB816	5.728	22.8± 3.07	32.0 <sup>+3.88</sup> <sub>-23.43</sub>	6.11± 1.78	1.50± 0.04
N8bb-39-33331	150.400417	1.801778	NB816	5.714	29.0± 2.89	20.3 <sup>+7.31</sup> <sub>-8.70</sub>	4.39± 1.07	1.29± 0.17
N8bb-40-24235	150.371167	1.824972	NB816	5.707	57.7± 6.12	60.9 <sup>+5.89</sup> <sub>-41.32</sub>	11.48± 3.25	3.43± 0.01
N8jp-28-71	150.362083	1.741694	NB816	5.686	32.1± 7.77	25.5 <sup>+3.21</sup> <sub>-19.25</sub>	8.72± 2.08	2.76± 0.65
V-18283	150.389042	1.634667	V <sub>J</sub> LBG	5.043	136.9± 114.02	15.7 <sup>+12.57</sup> <sub>-16.49</sub>	8.30± 2.41	1.20± 0.04
N7bb-40-9383	150.270708	1.921361	NB711	4.769	10.8± 1.58	11.7 <sup>+4.37</sup> <sub>-3.62</sub>	10.50± 2.58	1.05± 0.05
N7bb-40-18839	150.276917	1.885083	NB711	4.730	5.9± 1.49	2.9 <sup>+0.95</sup> <sub>-0.74</sub>	5.74± 1.50	0.65± 0.08
N8jp-40-64	150.280708	1.873000	NB816	5.668	16.5± 1.50	30.6 <sup>+14.84</sup> <sub>-12.36</sub>	10.27± 2.40	1.32± 0.02
N8bb-40-16913	150.262250	1.862417	NB816	5.666	33.0± 4.48	28.2 <sup>+17.88</sup> <sub>-12.60</sub>	10.31± 2.69	0.92± 0.07
N8bb-41-22708	150.123250	1.833500	NB816	5.707	13.9± 2.87	13.2 <sup>+5.91</sup> <sub>-8.37</sub>	6.63± 1.83	1.23± 0.01
N8ib-41-18744	150.213542	1.851056	NB816	4.931	7.7± 2.14	25.3 <sup>+4.29</sup> <sub>-17.80</sub>	8.83± 2.17	3.47± 0.15
N8jp-40-68	150.326708	1.951111	NB816	5.683	38.6± 1.63	26.1 <sup>+10.04</sup> <sub>-11.04</sub>	5.70± 0.24	2.72± 0.07
N8jp-40-70	150.349292	1.933389	NB816	5.726	37.9± 6.59	11.4 <sup>+8.01</sup> <sub>-7.32</sub>	6.45± 1.58	0.73± 0.08
V-7320	150.220583	1.899361	V <sub>J</sub> LBG	5.016	56.6± 13.17	83.0 <sup>+32.66</sup> <sub>-57.60</sub>	7.72± 2.50	1.48± 0.04
V-13973	150.197667	1.840889	V <sub>J</sub> LBG	3.971	31.2± 15.79	23.8 <sup>+6.26</sup> <sub>-22.03</sub>	6.63± 1.60	1.08± 0.41
N7bb-42-10805	149.983958	1.914306	NB711	4.840	28.2± 7.54	36.1 <sup>+7.44</sup> <sub>-29.31</sub>	9.05± 2.73	3.44± 0.01
N8bb-42-24675	149.966750	1.834944	NB816	5.744	49.0± 6.42	18.1 <sup>+8.76</sup> <sub>-6.88</sub>	14.12± 3.91	0.80± 0.03
N8bb-54-22980	150.003417	1.999083	NB816	5.655	12.2± 4.66	14.7 <sup>+2.44</sup> <sub>-11.07</sub>	10.08± 2.50	0.62± 0.01
N8jp-30-42	149.979208	1.789000	NB816	5.715	29.4± 4.85	17.2 <sup>+10.37</sup> <sub>-9.28</sub>	11.79± 4.17	2.75± 0.01
N8jp-42-43	150.002125	1.827806	NB816	5.672	18.0± 3.01	24.8 <sup>+15.32</sup> <sub>-15.95</sub>	8.85± 3.34	1.35± 0.01
N8jp-53-45	150.065292	2.015611	NB816	5.718	29.5± 3.40	19.9 <sup>+12.57</sup> <sub>-10.76</sub>	6.82± 1.48	2.23± 0.01
N8jp-53-47	150.083208	2.017611	NB816	5.645	322.0± 50.75	19.2 <sup>+7.25</sup> <sub>-8.88</sub>	7.56± 2.62	1.77± 0.01
B-18270	149.999208	1.970389	B <sub>J</sub> LBG	4.492	55.0± 9.56	24.0 <sup>+13.01</sup> <sub>-16.65</sub>	10.08± 2.71	0.68± 0.03
V-6310	150.027375	1.905889	V <sub>J</sub> LBG	4.566	19.2± 5.62	8.1 <sup>+3.71</sup> <sub>-4.01</sub>	8.11± 2.51	4.08± 3.60
V-16595	149.943208	1.811250	V <sub>J</sub> LBG	4.653	115.3± 14.51	50.5 <sup>+11.94</sup> <sub>-36.08</sub>	7.61± 2.37	1.15± 0.02
V-12253	150.055667	2.022306	V <sub>J</sub> LBG	4.622	410.6± 140.51	28.5 <sup>+9.71</sup> <sub>-18.72</sub>	14.65± 0.51	14.29± 0.01
qso_riz005	149.870833	1.882778	QSO	4.606	8.3± 3.35	16.8 <sup>+18.17</sup> <sub>-13.15</sub>	8.38± 2.10	7.19± 0.47
COSMOS	150.027917	1.884972	IA624	4.117	97.9± 8.53	21.1 <sup>+8.76</sup> <sub>-6.18</sub>	5.29± 1.35	1.70± 0.39
Rd-584387	149.913208	1.857861	r <sup>+</sup> LBG	5.135	33.2± 2.10	90.9 <sup>+33.53</sup> <sub>-60.07</sub>	10.75± 3.01	3.82± 0.06
Vdlz-602197	149.868125	1.895028	V <sub>J</sub> LBG	4.719	43.7± 10.56	31.7 <sup>+7.68</sup> <sub>-20.66</sub>	9.82± 2.96	1.31± 0.04
pz-559631	150.127833	1.862111	photo-z	4.278	42.3± 3.45	13.0 <sup>+3.79</sup> <sub>-2.71</sub>	10.36± 3.02	0.47± 0.03
Vdlz-527720	150.267125	1.901417	V <sub>J</sub> LBG	4.547	20.7± 2.28	21.1 <sup>+4.19</sup> <sub>-7.22</sub>	13.21± 3.08	0.62± 0.04
pz-553357	150.208250	1.903694	photo-z	4.740	38.3± 2.94	28.9 <sup>+5.09</sup> <sub>-15.76</sub>	7.62± 2.22	1.68± 0.01
Gd-557133	150.198375	1.877083	g <sup>+</sup> LBG	4.001	5.9± 2.78	4.2 <sup>+2.23</sup> <sub>-2.86</sub>	4.66± 1.24	0.60± 0.07
m45-598841	149.876708	1.924278	IRAC4.5 $\mu$ m	4.566	59.7± 13.10	-99.9 <sup>+0.00</sup> <sub>-0.00</sub>	17.73± 4.38	

Table 2—Continued

Source	RA J2000	DEC J2000	Type	z	Flux (1e-18 ergs/cm <sup>2</sup> /s)	EW <sub>Ly<math>\alpha</math>,0</sub> (Å)	FWHM (Å)	Skew
pz-789609	150.073625	1.968694	photo-z	4.994	28.2± 6.32	21.6 <sup>+15.90</sup> <sub>-9.05</sub>	11.37± 3.34	0.00± 0.01
Rd-520085	150.321333	1.955333	r <sup>+</sup> LBG	4.488	4.3± 1.29	35.5 <sup>+0.90</sup> <sub>-27.39</sub>	6.39± 1.86	1.32± 0.35
Rd-547589	150.179708	1.940833	r <sup>+</sup> LBG	5.387	61.8± 9.21	10.2 <sup>+9.80</sup> <sub>-4.16</sub>	7.11± 1.94	2.11± 0.05
m45-786441	150.142917	1.989222	IRAC4.5 $\mu$ m	4.466	54.4± 2.05	20.6 <sup>+1.07</sup> <sub>-4.72</sub>	12.16± 1.88	0.57± 0.04
pz-764734	150.311083	1.968139	photo-z	4.701	35.4± 3.22	30.7 <sup>+6.77</sup> <sub>-15.33</sub>	6.37± 1.18	1.28± 0.02
pz-765289	150.233375	1.962944	photo-z	4.740	26.4± 3.41	30.3 <sup>+10.12</sup> <sub>-19.08</sub>	6.74± 1.70	1.25± 0.01
Gd-525639	150.272292	1.917333	g <sup>+</sup> LBG	3.772	19.5± 5.78	22.2 <sup>+3.44</sup> <sub>-14.44</sub>	11.11± 2.52	0.59± 0.05
Gd-549720	150.162083	1.926194	g <sup>+</sup> LBG	4.325	8.6± 2.62	17.8 <sup>+1.74</sup> <sub>-12.74</sub>	3.00± 0.73	1.59± 2.41
COSMOS	150.446125	1.918194	IA624	4.020	43.0± 9.49	16.8 <sup>+5.84</sup> <sub>-10.29</sub>	6.85± 1.64	0.90± 0.05
Rd-496286	150.452375	1.957722	r <sup>+</sup> LBG	4.919	9.2± 3.16	5.4 <sup>+5.22</sup> <sub>-3.07</sub>	6.05± 1.53	0.42± 0.03
Rd-496641	150.438042	1.953417	r <sup>+</sup> LBG	4.909	29.4± 3.04	11.5 <sup>+8.02</sup> <sub>-2.79</sub>	5.81± 1.44	1.07± 0.02
Rd-736212	150.443083	1.991972	r <sup>+</sup> LBG	5.089	65.8± 8.68	47.2 <sup>+13.14</sup> <sub>-28.44</sub>	7.52± 1.81	1.21± 0.11
Vdlz-693689	150.579708	1.960222	V <sub>J</sub> LBG	4.098	13.2± 6.43	18.6 <sup>+4.32</sup> <sub>-13.23</sub>	19.15± 4.30	0.61± 0.06
Vdlz-739684	150.479333	1.967639	V <sub>J</sub> LBG	4.173	15.5± 6.04	18.8 <sup>+0.65</sup> <sub>-12.14</sub>	9.37± 2.44	1.30± 0.22
pz-496070	150.539750	1.951611	photo-z	4.406	21.9± 6.59	23.2 <sup>+8.45</sup> <sub>-15.20</sub>	6.21± 1.65	1.44± 0.05
pz-501373	150.403375	1.921306	photo-z	4.432	29.0± 8.08	22.8 <sup>+8.46</sup> <sub>-17.04</sub>	8.89± 2.19	1.72± 0.06
Rd-804402	149.902583	2.038389	r <sup>+</sup> LBG	4.720	13.6± 3.12	26.5 <sup>+11.05</sup> <sub>-14.96</sub>	10.86± 2.65	0.53± 0.02
Vdlz-806404	150.055625	2.022333	V <sub>J</sub> LBG	4.623	21.6± 11.90	4.7 <sup>+2.85</sup> <sub>-4.63</sub>	2.39± 0.35	2.00± 44.84
Gd-761379	150.323917	1.989667	g <sup>+</sup> LBG	4.030	15.3± 4.71	12.8 <sup>+6.46</sup> <sub>-7.08</sub>	9.26± 2.38	0.71± 0.05
Gd-761974	150.342708	1.985333	g <sup>+</sup> LBG	3.813	38.0± 8.04	11.9 <sup>+11.43</sup> <sub>-5.37</sub>	9.49± 2.28	1.13± 0.03
COSMOS	149.646875	2.081944	IA624	4.092	37.1± 2.90	22.9 <sup>+7.34</sup> <sub>-11.86</sub>	6.21± 1.70	1.08± 0.02
N7bb-55-13095	149.741292	2.080944	NB711	4.525	10.5± 2.72	26.0 <sup>+7.61</sup> <sub>-22.27</sub>	8.96± 2.46	1.94± 0.31
N7ib-55-10811	149.827292	2.089278	NB711	4.303	224.2± 62.38	-99.9 <sup>+0.00</sup> <sub>-0.00</sub>	4.84± 1.02	1.23± 0.03
N8bb-55-13814	149.832292	2.056139	NB816	5.704	16.3± 6.14	44.8 <sup>+3.20</sup> <sub>-41.47</sub>	12.14± 3.25	2.28± 0.10
N8bb-56-14179	149.721833	2.067083	NB816	5.649	77.3± 6.93	31.3 <sup>+7.65</sup> <sub>-19.10</sub>	7.50± 2.05	0.56± 0.02
Rd-843398	149.627500	2.108694	r <sup>+</sup> LBG	4.891	28.0± 2.52	31.0 <sup>+12.23</sup> <sub>-12.88</sub>	8.76± 2.85	0.64± 0.01
pz-845477	149.664292	2.088861	photo-z	4.093	8.4± 2.65	18.2 <sup>+6.59</sup> <sub>-12.81</sub>	7.91± 2.01	0.83± 0.04
m45-851027	149.618792	2.051889	IRAC4.5 $\mu$ m	5.546	35.3± 5.58	10.2 <sup>+0.87</sup> <sub>-4.42</sub>	6.43± 1.80	2.06± 0.09
Gd-827414	149.756250	2.050889	g <sup>+</sup> LBG	3.855	15.7± 8.32	14.8 <sup>+2.17</sup> <sub>-12.59</sub>	10.93± 1.78	0.22± 0.41
Vdz-189225	149.707042	2.066583	V <sub>J</sub> LBG	4.589	4.9± 2.02	-99.9 <sup>+0.00</sup> <sub>-0.00</sub>	11.20± 1.62	1.74± 0.01
COSMOS	149.898208	2.053139	IA624	4.118	31.9± 9.24	18.4 <sup>+7.57</sup> <sub>-11.71</sub>	7.22± 1.95	0.84± 0.02
Rd-793496	149.941708	2.111806	r <sup>+</sup> LBG	4.894	14.0± 2.95	17.8 <sup>+10.14</sup> <sub>-11.10</sub>	8.99± 2.17	0.60± 0.08
Vdlz-798659	149.971500	2.077139	V <sub>J</sub> LBG	4.555	42.9± 4.99	20.6 <sup>+6.57</sup> <sub>-7.44</sub>	7.52± 1.88	1.50± 0.04
pz-776988	150.097333	2.051222	photo-z	4.518	20.8± 3.52	6.3 <sup>+3.32</sup> <sub>-1.65</sub>	5.71± 1.52	0.73± 0.04
Vd-802160	150.021292	2.053389	V <sub>J</sub> LBG	5.240	9.1± 3.47	25.5 <sup>+1.05</sup> <sub>-19.91</sub>	9.79± 2.49	1.45± 0.08
Vdz-177851	150.016917	2.053667	V <sub>J</sub> LBG	5.203	4.9± 1.86	11.1 <sup>+0.46</sup> <sub>-8.75</sub>	4.74± 1.21	0.64± 0.07
COSMOS	150.147625	2.052667	IA624	4.195	26.9± 8.69	25.0 <sup>+29.55</sup> <sub>-18.97</sub>	7.24± 1.75	7.32± 0.19
COSMOS	150.128583	2.074750	IA624	4.096	95.2± 29.19	56.2 <sup>+0.00</sup> <sub>-0.00</sub>	5.35± 1.48	1.24± 0.02
rd-746010	150.254333	2.092083	r <sup>+</sup> LBG	4.938	22.8± 3.02	20.8 <sup>+6.88</sup> <sub>-10.30</sub>	11.11± 3.35	2.66± 0.11
Vd-749753	150.291042	2.075028	V <sub>J</sub> LBG	4.217	7.7± 3.57	13.7 <sup>+6.80</sup> <sub>-11.82</sub>	5.32± 1.47	0.16± 0.01
Gd-776657	150.117458	2.049833	g <sup>+</sup> LBG	4.155	52.3± 24.28	37.1 <sup>+16.45</sup> <sub>-32.89</sub>	7.18± 2.09	3.10± 0.15
Gd-748233	150.334708	2.076333	g <sup>+</sup> LBG	3.979	7.3± 3.34	23.9 <sup>+19.66</sup> <sub>-20.34</sub>	7.61± 1.59	1.81± 1.17
Vd-746980	150.354375	2.085639	V <sub>J</sub> LBG	5.032	17.7± 3.97	11.9 <sup>+2.78</sup> <sub>-6.79</sub>	8.12± 2.15	1.43± 0.02
Gd-773404	150.163958	2.070556	g <sup>+</sup> LBG	4.107	84.5± 11.22	45.5 <sup>+18.59</sup> <sub>-32.97</sub>	6.58± 2.15	1.42± 0.03
m45-769694	150.153458	2.101833	IRAC4.5 $\mu$ m	4.371	14.6± 4.81	22.6 <sup>+3.06</sup> <sub>-16.57</sub>	8.74± 2.24	1.27± 0.05

Table 2—Continued

Source	RA J2000	DEC J2000	Type	z	Flux (1e-18 ergs/cm <sup>2</sup> /s)	EW <sub>Ly<math>\alpha</math>,0</sub> (Å)	FWHM (Å)	Skew
chandra_931	150.359792	2.073694	AGN	4.908	57.7± 8.47	21.9 <sup>+16.99</sup> <sub>-6.43</sub>	12.04± 2.91	1.15± 0.14
COSMOS	149.697833	2.116889	IA624	4.155	49.0± 10.13	35.7 <sup>+3.98</sup> <sub>-25.10</sub>	6.25± 1.95	0.98± 0.02
Rd-816509	149.780292	2.122583	r <sup>+</sup> LBG	5.181	50.6± 6.05	18.9 <sup>+2.74</sup> <sub>-3.86</sub>	7.13± 2.01	1.02± 0.02
m45-1065581	149.758792	2.150722	IRAC4.5 $\mu$ m	5.305	18.5± 7.95	26.3 <sup>+3.89</sup> <sub>-24.82</sub>	8.43± 2.00	0.51± 0.05
Gd-816625	149.817667	2.120833	g <sup>+</sup> LBG	3.867	38.7± 18.54	22.4 <sup>+6.77</sup> <sub>-21.38</sub>	7.19± 1.81	1.52± 0.64
B12	149.971875	2.118222	sub-mm	5.699	22.7± 4.25	27.4 <sup>+5.90</sup> <sub>-10.63</sub>	16.78± 4.48	1.24± 0.08
B16	149.933250	2.166917	sub-mm	6.031	37.3± 8.07	15.9 <sup>+7.31</sup> <sub>-5.94</sub>	7.53± 1.91	1.31± 0.04
COSMOS	149.984000	2.126861	IA624	4.177	27.8± 7.02	27.1 <sup>+7.49</sup> <sub>-18.80</sub>	4.47± 1.17	1.79± 0.03
N7bb-66-39741	150.017375	2.146056	NB711	4.840	58.8± 5.52	28.6 <sup>+10.85</sup> <sub>-13.56</sub>	8.99± 2.27	1.00± 0.02
N8bb-54-1000	150.021000	2.121417	NB816	5.704	23.0± 4.72	26.0 <sup>+5.39</sup> <sub>-20.58</sub>	10.00± 2.41	0.93± 0.06
COSMOS	150.295792	2.124889	IA624	4.057	24.9± 8.73	26.7 <sup>+23.94</sup> <sub>-21.02</sub>	6.97± 1.82	0.76± 0.07
COSMOS	150.336542	2.127250	IA624	4.209	267.8± 24.02	47.7 <sup>+18.14</sup> <sub>-21.69</sub>	9.82± 2.77	1.05± 0.01
COSMOS	150.271958	2.155750	IA624	4.110	31.9± 9.97	28.6 <sup>+22.83</sup> <sub>-21.89</sub>	5.88± 1.45	1.48± 0.04
COSMOS	150.149000	2.155250	IA624	4.103	23.2± 10.82	31.9 <sup>+6.60</sup> <sub>-30.23</sub>	8.05± 1.91	1.01± 0.04
N8bb-52-807	150.249042	2.121889	NB816	5.642	14.5± 4.23	23.9 <sup>+5.08</sup> <sub>-18.75</sub>	7.77± 1.94	0.65± 0.03
Gd-988146	150.274792	2.163556	g <sup>+</sup> LBG	4.562	56.8± 5.39	29.7 <sup>+12.57</sup> <sub>-9.83</sub>	10.67± 2.54	1.67± 0.03
rd-985942	150.320542	2.175194	r <sup>+</sup> LBG	4.658	20.1± 7.24	32.4 <sup>+26.02</sup> <sub>-25.70</sub>	8.30± 2.13	2.77± 0.19
rd-1018964	150.187833	2.129056	r <sup>+</sup> LBG	5.706	2.7± 1.52	2.9 <sup>+3.03</sup> <sub>-1.81</sub>	4.26± 0.37	1.92± 10.54
Gd-1018158	150.191833	2.133944	g <sup>+</sup> LBG	4.417	22.0± 11.62	11.8 <sup>+4.14</sup> <sub>-11.76</sub>	11.07± 2.62	7.99± 2.56
zphot-1017802	150.178875	2.136806	photo-z	5.554	52.1± 26.27	17.4 <sup>+1.16</sup> <sub>-15.16</sub>	8.58± 2.23	0.38± 0.02
m45-990385	150.362833	2.148861	IRAC4.5 $\mu$ m	4.629	65.4± 21.02	26.6 <sup>+13.94</sup> <sub>-20.29</sub>	19.81± 4.90	0.55± 0.02
B20	150.036542	2.193444	sub-mm	5.866	15.0± 1.37	31.5 <sup>+25.95</sup> <sub>-30.82</sub>	14.47± 4.24	5.61± 0.01
zphot-1006191	150.076750	2.213083	photo-z	4.386	5.4± 2.72	28.9 <sup>+18.76</sup> <sub>-15.18</sub>	12.37± 2.97	2.05± 0.14
N7jp-38	150.230958	2.219222	NB711	4.872	26.1± 2.13	41.6 <sup>+4.25</sup> <sub>-29.80</sub>	5.03± 1.26	1.41± 0.02
N8bb-65-12966	150.203208	2.227833	NB816	5.709	14.0± 2.18	-99.9 <sup>+0.00</sup> <sub>-7.93</sub>	5.09± 1.38	0.93± 0.19
N8jp-64-66	150.290500	2.253806	NB816	5.712	73.2± 8.49	19.7 <sup>+0.00</sup> <sub>-7.93</sub>	7.21± 1.93	1.13± 0.09
Gd-1007642	150.110917	2.201667	g <sup>+</sup> LBG	4.528	11.5± 4.88	11.2 <sup>+4.68</sup> <sub>-7.84</sub>	10.81± 2.58	5.43± 1.53
Gd-982981	150.332042	2.197389	g <sup>+</sup> LBG	3.788	25.1± 8.63	20.8 <sup>+0.78</sup> <sub>-12.63</sub>	9.01± 2.37	1.73± 0.23
COSMOS	149.759083	2.295139	IA624	4.158	76.8± 22.38	9.0 <sup>+7.02</sup> <sub>-4.87</sub>	4.81± 1.40	0.90± 0.37
Vdlz-1072997	149.595708	2.268528	V <sub>J</sub> LBG	4.285	51.4± 8.05	36.9 <sup>+13.38</sup> <sub>-17.89</sub>	10.34± 3.01	1.96± 0.07
Vdlz-1291420	149.767917	2.312056	V <sub>J</sub> LBG	4.802	108.1± 56.80	22.8 <sup>+22.81</sup> <sub>-22.81</sub>	10.95± 2.51	0.51± 0.08
Vdlz-1292624	149.735208	2.310917	V <sub>J</sub> LBG	4.530	35.1± 5.52	15.6 <sup>+9.01</sup> <sub>-5.50</sub>	9.14± 2.21	0.96± 0.02
pz-1073870	149.618875	2.257278	photo-z	4.581	46.3± 15.26	-99.9 <sup>+0.00</sup> <sub>-0.00</sub>	16.55± 3.76	0.62± 0.05
pz-1074954	149.678250	2.256639	photo-z	3.933	91.0± 20.93	-99.9 <sup>+0.00</sup> <sub>-0.00</sub>	8.16± 1.97	1.52± 0.06
m45-1070303	149.587208	2.282917	IRAC4.5 $\mu$ m	4.916	105.3± 25.29	-99.9 <sup>+0.00</sup> <sub>-0.00</sub>	30.94± 6.39	0.49± 0.03
Vdz-245444	149.624917	2.271250	V <sub>J</sub> LBG	5.161	15.1± 2.92	21.0 <sup>+9.84</sup> <sub>-11.00</sub>	8.49± 2.00	0.35± 0.14
N8bb-65-832	150.126667	2.287444	NB816	5.695	15.7± 4.02	22.3 <sup>+10.13</sup> <sub>-11.75</sub>	11.78± 2.89	4.27± 0.68
N8bb-67-2393	149.875292	2.278528	NB816	5.680	617.0± 260.83	10.1 <sup>+0.11</sup> <sub>-9.16</sub>	6.50± 1.59	0.77± 0.05
N7bb-77-42228	150.198583	2.300611	NB711	4.586	35.1± 2.98	13.9 <sup>+2.58</sup> <sub>-4.88</sub>	8.87± 2.37	0.86± 0.02
N8bb-77-25517	150.167583	2.317750	NB816	5.719	22.0± 2.97	80.5 <sup>+25.76</sup> <sub>-65.69</sub>	7.93± 2.11	4.40± 0.49
rd-974353	150.270208	2.253889	r <sup>+</sup> LBG	4.540	4.8± 2.04	-99.9 <sup>+0.00</sup> <sub>-0.00</sub>	4.03± 1.13	0.96± 0.30
Gd-999142	150.135833	2.257917	g <sup>+</sup> LBG	4.450	25.3± 9.73	8.8 <sup>+5.19</sup> <sub>-5.37</sub>	8.91± 2.24	0.67± 0.18
rd-968994	150.346000	2.292222	r <sup>+</sup> LBG	4.730	26.1± 4.13	27.9 <sup>+5.05</sup> <sub>-9.68</sub>	20.85± 5.36	7.38± 0.40
Gd-971438	150.341167	2.272750	g <sup>+</sup> LBG	4.301	65.8± 19.23	23.0 <sup>+1.69</sup> <sub>-16.66</sub>	8.14± 2.12	1.01± 0.25
rd-996859	150.214167	2.273111	r <sup>+</sup> LBG	4.137	9.6± 3.67	-99.9 <sup>+0.00</sup> <sub>-0.00</sub>	5.13± 1.29	0.92± 0.49

Table 2—Continued

Source	RA J2000	DEC J2000	Type	z	Flux (1e-18 ergs/cm <sup>2</sup> /s)	EW <sub>Lya,0</sub> (Å)	FWHM (Å)	Skew
Gd-999621	150.217667	2.254306	g <sup>+</sup> LBG	4.541	30.8± 3.70	21.8 <sup>+13.00</sup> <sub>-8.12</sub>	10.04± 2.81	0.88± 0.02
zphot-999389	150.143000	2.256833	photo-z	5.121	5.7± 1.88	9.6 <sup>+5.66</sup> <sub>-4.14</sub>	9.94± 2.12	0.76± 0.06
zphot-1218871	150.309292	2.311778	photo-z	4.584	18.5± 7.05	15.5 <sup>+0.19</sup> <sub>-11.82</sub>	8.77± 3.86	0.48± 203.58
COSMOS	150.042042	2.317250	IA624	4.044	97.3± 19.82	22.0 <sup>+6.72</sup> <sub>-14.23</sub>	6.25± 1.63	1.30± 0.02
N8jp-79-27	149.877583	2.331694	NB816	5.687	18.5± 7.01	26.6 <sup>+10.86</sup> <sub>-23.98</sub>	12.37± 2.98	3.57± 0.24
Gd-1258302	149.946125	2.375806	g <sup>+</sup> LBG	4.414	17.1± 5.12	10.7 <sup>+5.63</sup> <sub>-6.12</sub>	7.44± 1.89	0.45± 0.14
zphot-1262018	150.008667	2.350889	photo-z	4.270	12.6± 6.12	12.9 <sup>+3.44</sup> <sub>-10.04</sub>	6.87± 1.73	1.56± 0.07
m45-1256817	149.950500	2.386028	IRAC4.5μm	5.432	37.0± 8.28	14.4 <sup>+6.84</sup> <sub>-5.37</sub>	4.54± 1.11	1.24± 0.17
N7jp-45	150.343500	2.380528	NB711	4.871	17.2± 6.55	-99.9 <sup>+0.00</sup> <sub>-0.00</sub>	7.46± 1.87	0.61± 0.07
Gd-1215565	150.292250	2.332306	g <sup>+</sup> LBG	4.534	23.0± 3.22	16.3 <sup>+10.33</sup> <sub>-7.52</sub>	8.70± 2.29	0.66± 0.03
rd-1233539	150.180083	2.378333	r <sup>+</sup> LBG	4.930	10.0± 3.20	9.2 <sup>+1.67</sup> <sub>-6.67</sub>	6.15± 1.54	0.47± 0.04
COSMOS	149.970125	2.406750	IA624	4.185	52.2± 9.99	-99.9 <sup>+0.00</sup> <sub>-0.00</sub>	4.91± 1.21	1.25± 0.07
N7jp-47	149.958417	2.414278	NB711	4.842	13.3± 4.94	19.6 <sup>+0.78</sup> <sub>-15.62</sub>	7.18± 1.84	0.78± 0.02
rd-1251268	150.009625	2.423361	r <sup>+</sup> LBG	5.053	15.2± 4.54	20.0 <sup>+6.87</sup> <sub>-10.49</sub>	13.20± 3.61	3.16± 1.30
Vd-1254662	150.059917	2.400333	V <sub>J</sub> LBG	4.663	74.3± 9.15	35.1 <sup>+7.83</sup> <sub>-11.52</sub>	14.38± 3.66	4.38± 0.28
N7bb-77-3905	150.171167	2.443722	NB711	4.867	30.2± 5.60	13.7 <sup>+6.81</sup> <sub>-5.45</sub>	8.44± 2.05	0.72± 0.02
N8bb-77-5438	150.163000	2.425694	NB816	5.642	32.3± 3.39	-99.9 <sup>+0.00</sup> <sub>-0.00</sub>	11.11± 2.67	1.84± 0.29
Rd-1204998	150.335792	2.402444	r <sup>+</sup> LBG	5.249	12.5± 6.49	14.7 <sup>+5.35</sup> <sub>-11.92</sub>	7.79± 2.09	1.52± 0.20
Rd-1205280	150.254875	2.399583	r <sup>+</sup> LBG	4.930	14.9± 6.76	11.9 <sup>+13.61</sup> <sub>-8.33</sub>	12.61± 2.92	0.09± 0.01
m45-1201590	150.302042	2.428556	IRAC4.5μm	4.521	19.5± 6.48	13.0 <sup>+4.39</sup> <sub>-10.33</sub>	4.91± 1.21	1.77± 0.05
m45-1202980	150.344125	2.417528	IRAC4.5μm	4.530	6.5± 1.40	12.3 <sup>+5.99</sup> <sub>-4.84</sub>	8.23± 2.34	2.20± 0.78
pz-1201657	150.280625	2.428556	photo-z	4.422	13.6± 4.87	7.2 <sup>+3.83</sup> <sub>-4.54</sub>	4.10± 1.08	2.11± 0.11
Vd-1203402	150.332958	2.413222	V <sub>J</sub> LBG	4.549	31.2± 5.63	34.1 <sup>+4.47</sup> <sub>-20.31</sub>	9.26± 2.74	2.31± 0.08
COSMOS	150.009458	2.463306	IA624	4.017	88.7± 19.48	34.0 <sup>+4.28</sup> <sub>-26.54</sub>	5.03± 1.27	1.52± 0.03
COSMOS	150.006167	2.463944	IA624	4.085	85.4± 6.57	31.1 <sup>+15.97</sup> <sub>-12.17</sub>	6.02± 1.38	1.37± 0.04
N7bb-91-33633	149.872250	2.497306	NB711	4.840	36.5± 2.38	30.0 <sup>+6.66</sup> <sub>-15.49</sub>	6.56± 1.98	1.52± 0.03
Id-1487302	149.981167	2.479972	i <sup>+</sup> LBG	4.750	18.0± 5.91	29.8 <sup>+28.13</sup> <sub>-24.90</sub>	6.12± 1.46	0.80± 0.03
m45-1465195	150.078417	2.470611	IRAC4.5μm	4.756	18.9± 3.49	30.0 <sup>+4.80</sup> <sub>-21.57</sub>	9.52± 2.52	1.70± 0.10
Vd-1246631	149.952208	2.455639	V <sub>J</sub> LBG	4.582	18.3± 3.53	21.1 <sup>+9.58</sup> <sub>-12.24</sub>	9.06± 2.29	2.83± 0.32
Vd-1460158	150.108875	2.505500	V <sub>J</sub> LBG	4.468	8.9± 1.86	25.7 <sup>+6.52</sup> <sub>-14.98</sub>	6.49± 1.67	1.44± 0.08
COSMOS	150.220625	2.460333	IA624	4.200	31.9± 10.11	22.3 <sup>+16.61</sup> <sub>-19.59</sub>	5.68± 0.75	0.86± 1.55
N7ib-89-31722	150.138250	2.509056	NB711	4.836	6.7± 3.49	13.4 <sup>+7.37</sup> <sub>-12.95</sub>	8.47± 2.03	0.81± 0.10
Id-1439889	150.291875	2.474806	i <sup>+</sup> LBG	5.679	15.7± 2.21	13.8 <sup>+5.59</sup> <sub>-6.44</sub>	12.38± 7.25	0.28± 10311.87
Vdlz-1435552	150.329583	2.506417	V <sub>J</sub> LBG	4.375	32.7± 1.85	27.7 <sup>+7.47</sup> <sub>-6.89</sub>	9.27± 2.84	0.93± 0.01
COSMOS	150.075042	2.552194	IA624	4.187	66.7± 10.34	18.5 <sup>+12.82</sup> <sub>-8.31</sub>	4.57± 0.73	1.00± 1.65
COSMOS	149.966625	2.528000	IA624	4.081	330.0± 114.78	-99.9 <sup>+0.00</sup> <sub>-0.00</sub>	3.14± 0.71	1.44± 0.11
N8jp-90-36	149.962500	2.539694	NB816	5.666	61.9± 23.75	42.5 <sup>+16.47</sup> <sub>-41.41</sub>	6.24± 1.59	1.55± 0.05
Vdlz-1474770	150.030667	2.570639	V <sub>J</sub> LBG	4.550	36.0± 3.10	20.4 <sup>+6.98</sup> <sub>-9.15</sub>	9.48± 2.54	0.86± 0.02
pz-1456157	150.100375	2.526806	photo-z	4.016	9.2± 4.15	12.4 <sup>+4.54</sup> <sub>-8.61</sub>	4.49± 0.75	0.84± 1.07
pz-1473252	149.974833	2.569944	photo-z	4.953	22.2± 7.97	15.8 <sup>+2.71</sup> <sub>-11.06</sub>	7.93± 1.90	0.70± 0.02
pz-1481860	149.988542	2.520250	photo-z	4.542	46.1± 16.31	19.7 <sup>+4.02</sup> <sub>-15.00</sub>	10.88± 2.46	1.06± 0.04
SMA3	150.086250	2.589028	sub-mm	5.309	15.6± 8.25	8.0 <sup>+12.06</sup> <sub>-7.28</sub>	8.39± 1.93	0.46± 0.03
Rd-1442768	150.104083	2.621750	r <sup>+</sup> LBG	5.200	49.6± 1.83	38.1 <sup>+16.14</sup> <sub>-13.48</sub>	8.93± 2.74	1.46± 0.02
Rd-1686652	150.016792	2.626694	r <sup>+</sup> LBG	5.158	40.0± 6.24	27.1 <sup>+12.91</sup> <sub>-14.73</sub>	8.24± 2.26	1.23± 0.03
m45-1711133	150.011292	2.627861	IRAC4.5μm	4.550	16.7± 5.88	13.7 <sup>+2.98</sup> <sub>-8.95</sub>	18.01± 5.16	5.40± 4.45

Table 2—Continued

Source	RA J2000	DEC J2000	Type	z	Flux ( $1e-18$ ergs/cm <sup>2</sup> /s)	EW <sub><i>Ly</i>α,0</sub> (Å)	FWHM (Å)	Skew
Vd-1469863	150.002042	2.605361	<i>V<sub>J</sub></i> LBG	4.531	12.6± 3.46	30.0 <sup>+5.11</sup> <sub>-24.24</sub>	9.31± 2.35	0.34± 0.03
Vd-1708971	149.979833	2.635639	<i>V<sub>J</sub></i> LBG	4.541	4.4± 1.67	28.1 <sup>+1.15</sup> <sub>-25.07</sub>	11.72± 3.12	3.31± 1.14
Gd-1470575	149.983375	2.599389	<i>g</i> <sup>+</sup> LBG	3.919	38.5± 4.27	23.3 <sup>+13.51</sup> <sub>-8.37</sub>	7.65± 1.91	1.75± 0.06
COSMOS	149.894875	2.670917	IA624	4.097	27.3± 4.55	22.8 <sup>+7.54</sup> <sub>-13.89</sub>	5.98± 1.60	0.96± 0.03
N7bb-101-29864	150.111333	2.684972	NB711	4.472	21.7± 1.69	10.9 <sup>+3.43</sup> <sub>-0.98</sub>	9.59± 2.64	1.94± 0.05
N7jp-69	149.944458	2.704361	NB711	4.849	13.3± 3.03	24.0 <sup>+8.47</sup> <sub>-14.53</sub>	7.51± 1.89	8.33± 14.12
N8bb-101-23318	150.121333	2.687722	NB816	5.735	41.8± 5.98	76.6 <sup>+0.42</sup> <sub>-66.20</sub>	6.25± 1.73	1.26± 0.02
N8bb-101-23908	150.093750	2.684278	NB816	5.661	65.6± 4.33	43.1 <sup>+19.11</sup> <sub>-19.05</sub>	10.54± 3.11	1.20± 0.03
pz-1682081	150.078458	2.657444	photo-z	3.968	47.0± 6.88	19.9 <sup>+7.58</sup> <sub>-8.28</sub>	7.67± 2.08	1.14± 0.02
pz-1725039	149.890917	2.698944	photo-z	4.554	13.2± 2.76	28.9 <sup>+3.27</sup> <sub>-20.14</sub>	6.55± 1.61	1.77± 0.05
Vd-1697491	149.901167	2.719361	<i>V<sub>J</sub></i> LBG	4.420	13.5± 1.86	16.6 <sup>+12.54</sup> <sub>-5.67</sub>	6.84± 1.47	1.00± 0.59
N8bb-115-24856	149.889250	2.832222	NB816	5.724	22.5± 8.06	28.0 <sup>+8.07</sup> <sub>-25.53</sub>	15.64± 3.66	8.74± 0.51
N8jp-114-35	149.958583	2.901694	NB816	5.726	58.0± 6.18	15.3 <sup>+3.44</sup> <sub>-7.53</sub>	5.40± 1.59	0.97± 0.03
N8jp-109-108	150.805417	2.925000	NB816	5.714	21.4± 10.07	12.8 <sup>+4.27</sup> <sub>-11.78</sub>	5.46± 1.34	2.57± 3.36

Table 3. Double Peaked Ly $\alpha$  Emission

Source	RA J2000	DEC J2000	Type	Ly $\alpha$ z	Flux (1e-18 ergs/cm <sup>2</sup> /s)	EW (Å)	FWHM(Å)
pz-559631	150.127833	1.862111	photo-z	4.262	16.2 $\pm$ 2.83	160.9 <sup>+26.22</sup> <sub>-109.19</sub>	4.89 $\pm$ 1.20
				4.278	42.3 $\pm$ 3.45	68.8 <sup>+20.03</sup> <sub>-14.32</sub>	4.28 $\pm$ 2.22
m45-786441	150.142917	1.989222	IRAC CH2	4.457	7.8 $\pm$ 0.74	14.0 <sup>+5.19</sup> <sub>-3.53</sub>	2.26 $\pm$ 0.18
				4.466	54.4 $\pm$ 2.05	112.6 <sup>+5.87</sup> <sub>-25.81</sub>	6.77 $\pm$ 2.33



Table 4. Best-fit Model SED Parameters

Source	RA J2000	DEC J2000	Best $\chi^2$	Best E(B-V)	Log Median SFR <sup>a</sup> (M <sub>⊙</sub> /yr)	Log Median Mass <sup>a</sup> (M <sub>⊙</sub> )	Median Age <sup>a</sup> (Gyr)
N8jp-109-108	150.805417	2.925000	21.2	0.0	1.31 <sup>2.22</sup> <sub>0.89</sub>	9.62 <sup>10.60</sup> <sub>8.99</sub>	0.23 <sup>0.58</sup> <sub>0.09</sub>
N8bb-54-1862	149.971875	2.118167	12.3	0.2	2.24 <sup>2.38</sup> <sub>2.12</sub>	10.39 <sup>10.56</sup> <sub>10.18</sub>	0.17 <sup>0.30</sup> <sub>0.11</sub>
N8bb-54-20446	149.933583	2.014083	11.4	0.0	1.23 <sup>1.67</sup> <sub>0.80</sub>	9.49 <sup>9.82</sup> <sub>9.06</sub>	0.22 <sup>0.55</sup> <sub>0.10</sub>
N8bb-66-30821	149.942250	2.128583	109.4	0.0	1.10 <sup>1.48</sup> <sub>1.01</sub>	9.97 <sup>10.27</sup> <sub>9.67</sub>	0.62 <sup>0.85</sup> <sub>0.30</sub>
N8jp-66-40	149.977208	2.254611	0.6	0.0	1.47 <sup>2.40</sup> <sub>0.65</sub>	9.76 <sup>10.78</sup> <sub>8.93</sub>	0.25 <sup>0.59</sup> <sub>0.10</sub>
N8jp-66-41	149.978292	2.177611	3.6	0.0	1.61 <sup>2.07</sup> <sub>0.89</sub>	9.94 <sup>10.35</sup> <sub>9.33</sub>	0.27 <sup>0.61</sup> <sub>0.11</sub>
B-8431	149.941292	2.057139	156.0	0.0	1.12 <sup>1.19</sup> <sub>1.04</sub>	9.80 <sup>9.96</sup> <sub>9.57</sub>	0.65 <sup>0.97</sup> <sub>0.36</sub>
V-2019	149.941750	2.111778	—	0.0	0.00 <sup>0.00</sup> <sub>0.00</sub>	0.00 <sup>0.00</sup> <sub>0.00</sub>	0.00 <sup>0.00</sup> <sub>0.00</sub>
N8bb-37-10756	150.790833	1.897889	—	0.0	0.00 <sup>0.00</sup> <sub>0.00</sub>	0.00 <sup>0.00</sup> <sub>0.00</sub>	0.00 <sup>0.00</sup> <sub>0.00</sub>
N8bb-37-33891	150.775583	1.795306	2.0	0.0	1.30 <sup>2.29</sup> <sub>1.60</sub>	9.60 <sup>10.64</sup> <sub>8.78</sub>	0.25 <sup>0.59</sup> <sub>0.10</sub>
N8bb-49-19547	150.754792	2.043361	7.7	0.0	1.95 <sup>2.08</sup> <sub>1.46</sub>	10.38 <sup>10.56</sup> <sub>10.15</sub>	0.32 <sup>0.65</sup> <sub>0.15</sub>
N8bb-49-20883	150.779167	2.037833	4.2	0.0	1.73 <sup>2.11</sup> <sub>1.22</sub>	10.10 <sup>10.37</sup> <sub>9.63</sub>	0.26 <sup>0.59</sup> <sub>0.10</sub>
N8jp-37-103	150.757583	1.836500	—	0.0	0.00 <sup>0.00</sup> <sub>0.00</sub>	0.00 <sup>0.00</sup> <sub>0.00</sub>	0.00 <sup>0.00</sup> <sub>0.00</sub>
N8jp-37-104	150.772208	1.861389	—	0.0	0.00 <sup>0.00</sup> <sub>0.00</sub>	0.00 <sup>0.00</sup> <sub>0.00</sub>	0.00 <sup>0.00</sup> <sub>0.00</sub>
B-10208	150.749458	1.824611	34.3	0.0	0.88 <sup>0.99</sup> <sub>0.79</sub>	9.51 <sup>9.82</sup> <sub>8.96</sub>	0.52 <sup>1.05</sup> <sub>0.14</sub>
V-4084	150.781250	1.906083	6.8	0.0	1.05 <sup>1.36</sup> <sub>0.77</sub>	9.64 <sup>10.03</sup> <sub>9.14</sub>	0.39 <sup>0.88</sup> <sub>0.14</sub>
N7bb-87-10648	150.512667	2.588472	—	0.0	0.00 <sup>0.00</sup> <sub>0.00</sub>	0.00 <sup>0.00</sup> <sub>0.00</sub>	0.00 <sup>0.00</sup> <sub>0.00</sub>
N7bb-88-24551	150.363125	2.536167	59.5	0.2	2.44 <sup>2.55</sup> <sub>1.81</sub>	9.49 <sup>9.99</sup> <sub>9.44</sub>	0.10 <sup>0.20</sup> <sub>0.01</sub>
N8bb-87-6788	150.438125	2.599361	50.3	0.0	1.37 <sup>1.80</sup> <sub>0.96</sub>	9.78 <sup>10.11</sup> <sub>9.33</sub>	0.31 <sup>0.68</sup> <sub>0.12</sub>
N8bb-88-26173	150.379458	2.518333	0.6	0.5	2.27 <sup>3.23</sup> <sub>1.22</sub>	10.43 <sup>11.48</sup> <sub>9.35</sub>	0.23 <sup>0.56</sup> <sub>0.10</sub>
N8bb-88-29007	150.365708	2.501694	2.3	0.0	1.24 <sup>1.89</sup> <sub>0.83</sub>	9.55 <sup>10.41</sup> <sub>8.95</sub>	0.24 <sup>0.60</sup> <sub>0.10</sub>
N8bb-88-33344	150.291917	2.474778	—	0.0	0.00 <sup>0.00</sup> <sub>0.00</sub>	0.00 <sup>0.00</sup> <sub>0.00</sub>	0.00 <sup>0.00</sup> <sub>0.00</sub>
B-6014	150.432125	2.572528	36.2	0.0	1.41 <sup>1.53</sup> <sub>0.98</sub>	10.27 <sup>10.41</sup> <sub>10.07</sub>	0.79 <sup>1.13</sup> <sub>0.45</sub>
B-9848	150.475625	2.540722	19.1	0.0	1.10 <sup>1.63</sup> <sub>0.68</sub>	10.29 <sup>10.44</sup> <sub>10.12</sub>	0.89 <sup>1.06</sup> <sub>0.40</sub>
N7bb-100-45206	150.297208	2.634806	22.4	0.0	1.12 <sup>1.31</sup> <sub>1.01</sub>	8.80 <sup>9.38</sup> <sub>8.26</sub>	0.10 <sup>0.32</sup> <sub>0.01</sub>
N7ib-89-7876	150.129875	2.598083	154.0	0.0	1.16 <sup>1.25</sup> <sub>1.06</sub>	10.70 <sup>10.76</sup> <sub>10.64</sub>	0.90 <sup>0.97</sup> <sub>0.83</sub>
Vc-89-8485	150.214958	2.582667	309.7	0.2	2.95 <sup>3.30</sup> <sub>2.57</sub>	11.39 <sup>11.67</sup> <sub>10.86</sub>	0.24 <sup>0.62</sup> <sub>0.10</sub>
N7bb-39-5654	150.497792	1.936917	37.0	0.3	2.47 <sup>2.58</sup> <sub>2.05</sub>	10.16 <sup>10.35</sup> <sub>10.08</sub>	0.05 <sup>0.24</sup> <sub>0.05</sub>
N7bb-39-20615	150.530042	1.881639	44.5	0.0	0.94 <sup>1.15</sup> <sub>0.83</sub>	9.00 <sup>9.59</sup> <sub>8.13</sub>	0.17 <sup>0.63</sup> <sub>0.05</sub>
N8bb-38-6719	150.690250	1.926667	3.3	0.0	1.86 <sup>2.22</sup> <sub>1.41</sub>	10.22 <sup>10.43</sup> <sub>9.96</sub>	0.29 <sup>0.62</sup> <sub>0.11</sub>
N8ib-39-8551	150.536667	1.912556	19.8	0.0	1.85 <sup>2.28</sup> <sub>1.34</sub>	10.39 <sup>10.55</sup> <sub>10.19</sub>	0.36 <sup>0.70</sup> <sub>0.14</sub>
N8ib-39-551	150.539750	1.951583	—	0.0	0.00 <sup>0.00</sup> <sub>0.00</sub>	0.00 <sup>0.00</sup> <sub>0.00</sub>	0.00 <sup>0.00</sup> <sub>0.00</sub>
B-1441	150.678875	1.947111	8.4	0.0	0.84 <sup>0.95</sup> <sub>0.75</sub>	9.23 <sup>9.57</sup> <sub>8.88</sub>	0.30 <sup>0.75</sup> <sub>0.12</sub>
B-6412	150.596375	1.897556	7.7	0.2	1.83 <sup>1.95</sup> <sub>1.43</sub>	9.64 <sup>9.86</sup> <sub>9.51</sub>	0.09 <sup>0.26</sup> <sub>0.05</sub>
B-3516	150.543292	1.927000	42.6	0.1	1.39 <sup>1.80</sup> <sub>1.14</sub>	10.35 <sup>10.50</sup> <sub>10.19</sub>	0.79 <sup>1.18</sup> <sub>0.32</sub>
V-8065	150.481917	1.881667	21.5	0.0	0.78 <sup>1.24</sup> <sub>0.62</sub>	10.23 <sup>10.39</sup> <sub>9.93</sub>	0.93 <sup>1.12</sup> <sub>0.56</sub>
N7bb-16-16904	150.296500	1.560389	0.1	0.5	1.26 <sup>2.27</sup> <sub>0.29</sub>	9.65 <sup>10.63</sup> <sub>8.71</sub>	0.28 <sup>0.71</sup> <sub>0.11</sub>
N7bb-17-4622	150.161000	1.609806	13.4	0.2	1.85 <sup>2.45</sup> <sub>1.73</sub>	9.94 <sup>10.12</sup> <sub>9.46</sub>	0.17 <sup>0.29</sup> <sub>0.05</sub>
N7bb-17-5717	150.126792	1.606000	13.1	0.0	0.89 <sup>1.22</sup> <sub>0.66</sub>	9.54 <sup>9.86</sup> <sub>9.12</sub>	0.44 <sup>0.89</sup> <sub>0.15</sub>
N8bb-16-2464	150.243375	1.611889	7.3	0.5	2.83 <sup>3.30</sup> <sub>1.91</sub>	11.02 <sup>11.72</sup> <sub>10.02</sub>	0.23 <sup>0.56</sup> <sub>0.10</sub>
N8bb-16-3055	150.231333	1.608556	0.1	0.3	2.61 <sup>3.40</sup> <sub>1.73</sub>	10.85 <sup>11.69</sup> <sub>10.00</sub>	0.25 <sup>0.59</sup> <sub>0.10</sub>
N8bb-16-12770	150.247083	1.555444	7.9	0.0	2.05 <sup>2.49</sup> <sub>1.90</sub>	10.34 <sup>10.52</sup> <sub>10.11</sub>	0.24 <sup>0.45</sup> <sub>0.10</sub>
N8bb-17-10353	150.191875	1.576583	7.7	0.0	1.66 <sup>2.07</sup> <sub>1.18</sub>	10.35 <sup>10.54</sup> <sub>10.13</sub>	0.40 <sup>0.82</sup> <sub>0.17</sub>
V-4073	150.261250	1.590667	18.2	0.0	0.86 <sup>1.26</sup> <sub>0.74</sub>	9.39 <sup>9.74</sup> <sub>8.91</sub>	0.31 <sup>0.88</sup> <sub>0.11</sub>
V-2597	150.144250	1.604472	31.3	0.0	1.50 <sup>1.92</sup> <sub>1.34</sub>	10.00 <sup>10.20</sup> <sub>9.75</sub>	0.30 <sup>0.83</sup> <sub>0.11</sub>

Table 4—Continued

Source	RA J2000	DEC J2000	Best $\chi^2$	Best E(B-V)	Log Median SFR <sup>a</sup> (M <sub>⊙</sub> /yr)	Log Median Mass <sup>a</sup> (M <sub>⊙</sub> )	Median Age <sup>a</sup> (Gyr)
V-4147	150.222250	1.590667	10.4	0.0	1.17 <sup>2.01</sup> <sub>0.68</sub>	9.60 <sup>10.46</sup> <sub>8.85</sub>	0.28 <sup>0.82</sup> <sub>0.10</sub>
N8bb-30-13181	149.942208	1.731528	—	0.0	0.00 <sup>0.00</sup> <sub>0.00</sub>	0.00 <sup>0.00</sup> <sub>0.00</sub>	0.00 <sup>0.00</sup> <sub>0.00</sub>
N8bb-30-18324	149.905667	1.710778	5.4	0.2	1.34 <sup>1.77</sup> <sub>0.93</sub>	9.52 <sup>9.76</sup> <sub>9.17</sub>	0.20 <sup>0.52</sup> <sub>0.06</sub>
N8jp-18-31	149.930292	1.598000	5.2	0.0	1.36 <sup>1.79</sup> <sub>0.93</sub>	9.83 <sup>10.09</sup> <sub>9.45</sub>	0.29 <sup>0.65</sup> <sub>0.12</sub>
N8jp-18-37	149.967208	1.623111	10.3	0.0	1.03 <sup>1.57</sup> <sub>0.86</sub>	9.43 <sup>10.13</sup> <sub>8.88</sub>	0.24 <sup>0.60</sup> <sub>0.09</sub>
B-16566	149.934792	1.638083	4.9	0.0	1.40 <sup>1.50</sup> <sub>1.10</sub>	9.67 <sup>9.88</sup> <sub>9.45</sub>	0.23 <sup>0.48</sup> <sub>0.11</sub>
B-9885	149.885292	1.701667	31.7	0.1	1.64 <sup>1.78</sup> <sub>1.21</sub>	9.62 <sup>9.82</sup> <sub>9.32</sub>	0.13 <sup>0.37</sup> <sub>0.05</sub>
V-1135	149.939042	1.617556	21.7	0.3	1.96 <sup>2.42</sup> <sub>1.84</sub>	10.32 <sup>10.49</sup> <sub>10.06</sub>	0.23 <sup>0.51</sup> <sub>0.05</sub>
V-9995	149.960083	1.527694	21.0	0.0	-0.34 <sup>0.21</sup> <sub>0.56</sub>	11.00 <sup>11.05</sup> <sub>10.95</sub>	2.01 <sup>2.22</sup> <sub>0.98</sub>
V-11671	149.925333	1.683472	4.9	0.0	1.23 <sup>1.40</sup> <sub>1.44</sub>	9.68 <sup>9.98</sup> <sub>9.33</sub>	0.35 <sup>0.81</sup> <sub>0.12</sub>
N7bb-28-9956	150.361125	1.757306	26.8	0.2	2.43 <sup>2.55</sup> <sub>1.86</sub>	9.55 <sup>9.97</sup> <sub>9.49</sub>	0.10 <sup>0.17</sup> <sub>0.01</sub>
N8bb-27-22829	150.398500	1.685611	0.6	0.0	1.53 <sup>2.48</sup> <sub>0.76</sub>	9.79 <sup>10.82</sup> <sub>8.98</sub>	0.25 <sup>0.59</sup> <sub>0.10</sub>
N8bb-28-12615	150.379625	1.722333	7.0	0.0	0.96 <sup>1.37</sup> <sub>0.84</sub>	9.38 <sup>9.69</sup> <sub>8.97</sub>	0.24 <sup>0.56</sup> <sub>0.10</sub>
N8bb-39-33331	150.400417	1.801778	56.1	0.1	1.79 <sup>2.20</sup> <sub>1.44</sub>	10.35 <sup>10.51</sup> <sub>10.16</sub>	0.39 <sup>0.74</sup> <sub>0.14</sub>
N8bb-40-24235	150.371167	1.824972	16.4	0.0	1.47 <sup>1.86</sup> <sub>1.01</sub>	10.16 <sup>10.40</sup> <sub>9.87</sub>	0.49 <sup>0.82</sup> <sub>0.19</sub>
N8jp-28-71	150.362083	1.741694	4.2	0.0	1.22 <sup>1.65</sup> <sub>1.10</sub>	9.39 <sup>9.69</sup> <sub>9.06</sub>	0.17 <sup>0.39</sup> <sub>0.05</sub>
V-18283	150.389042	1.634667	103.1	0.0	0.82 <sup>0.96</sup> <sub>0.73</sub>	10.32 <sup>10.44</sup> <sub>10.27</sub>	0.89 <sup>0.99</sup> <sub>0.64</sub>
N7bb-40-9383	150.270708	1.921361	37.0	0.0	1.45 <sup>1.87</sup> <sub>1.04</sub>	9.78 <sup>9.20</sup> <sub>9.89</sub>	0.28 <sup>0.75</sup> <sub>0.10</sub>
N7bb-40-18839	150.276917	1.885083	25.8	0.3	2.31 <sup>2.87</sup> <sub>2.21</sub>	10.00 <sup>10.23</sup> <sub>9.81</sub>	0.09 <sup>0.12</sup> <sub>0.05</sub>
N8jp-40-64	150.280708	1.873000	0.1	0.0	2.23 <sup>2.63</sup> <sub>1.55</sub>	10.56 <sup>11.03</sup> <sub>9.81</sub>	0.27 <sup>0.62</sup> <sub>0.11</sub>
N8bb-40-16913	150.262250	1.862417	9.6	0.0	1.37 <sup>1.79</sup> <sub>0.97</sub>	9.84 <sup>10.11</sup> <sub>9.43</sub>	0.28 <sup>0.63</sup> <sub>0.11</sub>
N8bb-41-22708	150.123250	1.833500	3.4	0.1	1.54 <sup>1.82</sup> <sub>1.22</sub>	9.82 <sup>9.56</sup> <sub>9.56</sub>	0.23 <sup>0.55</sup> <sub>0.10</sub>
N8ib-41-18744	150.213542	1.851056	26.4	0.1	1.30 <sup>1.68</sup> <sub>1.20</sub>	9.68 <sup>9.95</sup> <sub>9.36</sub>	0.30 <sup>0.68</sup> <sub>0.11</sub>
N8jp-40-68	150.326708	1.951111	124.2	0.0	0.94 <sup>1.29</sup> <sub>0.83</sub>	9.30 <sup>9.66</sup> <sub>8.80</sub>	0.25 <sup>0.60</sup> <sub>0.10</sub>
N8jp-40-70	150.349292	1.933389	3.0	0.0	1.18 <sup>1.80</sup> <sub>0.76</sub>	9.51 <sup>10.39</sup> <sub>8.92</sub>	0.25 <sup>0.61</sup> <sub>0.10</sub>
V-7320	150.220583	1.899361	189.0	0.0	1.27 <sup>1.46</sup> <sub>0.90</sub>	10.26 <sup>10.42</sup> <sub>10.11</sub>	0.80 <sup>0.97</sup> <sub>0.59</sub>
V-13973	150.197667	1.840889	25.9	0.5	3.09 <sup>3.16</sup> <sub>3.01</sub>	10.07 <sup>10.12</sup> <sub>10.02</sub>	0.01 <sup>0.05</sup> <sub>0.01</sub>
N7bb-42-10805	149.983958	1.914306	4.1	0.0	1.44 <sup>2.29</sup> <sub>0.65</sub>	9.90 <sup>10.77</sup> <sub>9.07</sub>	0.29 <sup>0.76</sup> <sub>0.11</sub>
N8bb-42-24675	149.966750	1.834944	2.0	0.1	1.56 <sup>1.97</sup> <sub>1.40</sub>	9.98 <sup>10.22</sup> <sub>9.63</sub>	0.25 <sup>0.59</sup> <sub>0.10</sub>
N8bb-54-22980	150.003417	1.999083	10.0	0.1	1.89 <sup>2.05</sup> <sub>1.46</sub>	10.09 <sup>10.29</sup> <sub>9.87</sub>	0.22 <sup>0.57</sup> <sub>0.11</sub>
N8jp-30-42	149.979208	1.789000	2.7	0.0	1.40 <sup>1.83</sup> <sub>1.20</sub>	9.85 <sup>10.09</sup> <sub>9.53</sub>	0.29 <sup>0.65</sup> <sub>0.11</sub>
N8jp-42-43	150.002125	1.827806	49.0	0.0	0.94 <sup>1.62</sup> <sub>0.70</sub>	9.27 <sup>10.05</sup> <sub>8.69</sub>	0.22 <sup>0.56</sup> <sub>0.09</sub>
N8jp-53-45	150.065292	2.015611	7.7	0.0	1.17 <sup>1.38</sup> <sub>0.77</sub>	9.59 <sup>9.84</sup> <sub>9.26</sub>	0.32 <sup>0.69</sup> <sub>0.13</sub>
N8jp-53-47	150.083208	2.017611	0.9	0.0	1.70 <sup>1.95</sup> <sub>1.31</sub>	10.03 <sup>10.24</sup> <sub>9.75</sub>	0.27 <sup>0.60</sup> <sub>0.11</sub>
B-18270	149.999208	1.970389	0.9	0.0	0.99 <sup>1.08</sup> <sub>0.91</sub>	10.16 <sup>10.31</sup> <sub>9.90</sub>	0.86 <sup>1.24</sup> <sub>0.64</sub>
V-6310	150.027375	1.905889	6.7	0.2	1.56 <sup>2.19</sup> <sub>1.45</sub>	9.59 <sup>9.78</sup> <sub>9.18</sub>	0.15 <sup>0.24</sup> <sub>0.01</sub>
V-16595	149.943208	1.811250	23.5	0.0	0.84 <sup>0.96</sup> <sub>0.73</sub>	10.43 <sup>10.50</sup> <sub>10.34</sub>	0.92 <sup>1.01</sup> <sub>0.81</sub>
V-12253	150.055667	2.022306	—	0.0	0.00 <sup>0.00</sup> <sub>0.00</sub>	0.00 <sup>0.00</sup> <sub>0.00</sub>	0.00 <sup>0.00</sup> <sub>0.00</sub>
qso_riz005	149.870833	1.882778	24.6	0.2	2.19 <sup>2.27</sup> <sub>2.11</sub>	10.54 <sup>10.65</sup> <sub>10.42</sub>	0.26 <sup>0.34</sup> <sub>0.17</sub>
COSMOS	150.027917	1.884972	10.1	0.0	1.31 <sup>1.71</sup> <sub>0.88</sub>	9.58 <sup>9.80</sup> <sub>9.33</sub>	0.25 <sup>0.72</sup> <sub>0.10</sub>
Rd-584387	149.913208	1.857861	12.9	0.2	2.13 <sup>2.67</sup> <sub>1.70</sub>	9.75 <sup>10.07</sup> <sub>9.63</sub>	0.09 <sup>0.19</sup> <sub>0.01</sub>
Vdlz-602197	149.868125	1.895028	10.7	0.0	1.23 <sup>1.34</sup> <sub>1.14</sub>	9.60 <sup>9.95</sup> <sub>9.24</sub>	0.30 <sup>0.72</sup> <sub>0.11</sub>
pz-559631	150.127833	1.862111	11.1	0.0	1.15 <sup>1.27</sup> <sub>1.06</sub>	9.69 <sup>9.86</sup> <sub>9.49</sub>	0.42 <sup>0.68</sup> <sub>0.18</sub>
Vdlz-527720	150.267125	1.901417	61.0	0.2	1.83 <sup>2.00</sup> <sub>1.74</sub>	10.06 <sup>10.21</sup> <sub>9.78</sub>	0.22 <sup>0.31</sup> <sub>0.13</sub>
pz-553357	150.208250	1.903694	16.4	0.0	0.97 <sup>1.08</sup> <sub>0.87</sub>	9.30 <sup>9.69</sup> <sub>8.91</sub>	0.28 <sup>0.71</sup> <sub>0.10</sub>

Table 4—Continued

Source	RA J2000	DEC J2000	Best $\chi^2$	Best E(B-V)	Log Median SFR <sup>a</sup> (M <sub>⊙</sub> /yr)	Log Median Mass <sup>a</sup> (M <sub>⊙</sub> )	Median Age <sup>a</sup> (Gyr)
Gd-557133	150.198375	1.877083	20.6	0.0	0.84 <sup>0.99</sup> <sub>0.75</sub>	9.75 <sup>9.85</sup> <sub>9.55</sub>	0.91 <sup>1.23</sup> <sub>0.36</sub>
m45-598841	149.876708	1.924278	8.1	0.4	2.24 <sup>2.44</sup> <sub>1.96</sub>	11.02 <sup>11.14</sup> <sub>10.86</sub>	0.72 <sup>1.13</sup> <sub>0.31</sub>
pz-789609	150.073625	1.968694	10.0	0.0	1.41 <sup>1.54</sup> <sub>0.98</sub>	9.96 <sup>10.13</sup> <sub>9.76</sub>	0.44 <sup>0.76</sup> <sub>0.18</sub>
Rd-520085	150.321333	1.955333	23.6	0.3	2.31 <sup>2.43</sup> <sub>2.22</sub>	10.42 <sup>10.53</sup> <sub>10.27</sub>	0.16 <sup>0.22</sup> <sub>0.11</sub>
Rd-547589	150.179708	1.940833	52.1	0.0	0.94 <sup>1.05</sup> <sub>0.85</sub>	10.55 <sup>10.64</sup> <sub>10.44</sub>	0.85 <sup>0.99</sup> <sub>0.39</sub>
m45-786441	150.142917	1.989222	53.7	0.0	1.54 <sup>1.62</sup> <sub>1.46</sub>	10.36 <sup>10.43</sup> <sub>10.23</sub>	0.85 <sup>1.03</sup> <sub>0.59</sub>
pz-764734	150.311083	1.968139	15.3	0.0	1.00 <sup>1.19</sup> <sub>0.96</sub>	9.69 <sup>9.89</sup> <sub>9.41</sub>	0.51 <sup>0.91</sup> <sub>0.17</sub>
pz-765289	150.233375	1.962944	6.1	0.1	1.35 <sup>1.76</sup> <sub>1.22</sub>	9.93 <sup>10.12</sup> <sub>9.73</sub>	0.38 <sup>0.87</sup> <sub>0.14</sub>
Gd-525639	150.272292	1.917333	20.0	0.2	1.66 <sup>2.28</sup> <sub>1.56</sub>	9.68 <sup>9.81</sup> <sub>9.29</sub>	0.14 <sup>0.19</sup> <sub>0.05</sub>
Gd-549720	150.162083	1.926194	2.8	0.2	1.57 <sup>1.69</sup> <sub>1.17</sub>	9.97 <sup>10.13</sup> <sub>9.76</sub>	0.30 <sup>0.74</sup> <sub>0.15</sub>
COSMOS	150.446125	1.918194	7.2	0.0	0.82 <sup>1.22</sup> <sub>0.65</sub>	9.26 <sup>9.73</sup> <sub>8.79</sub>	0.28 <sup>0.88</sup> <sub>0.10</sub>
N8bb-39-5745	150.517125	1.928944	33.9	0.3	2.81 <sup>2.89</sup> <sub>2.26</sub>	9.84 <sup>10.11</sup> <sub>9.80</sub>	0.01 <sup>0.13</sup> <sub>0.01</sub>
Rd-496286	150.452375	1.957722	4.1	0.1	1.80 <sup>2.19</sup> <sub>1.42</sub>	10.65 <sup>10.78</sup> <sub>10.52</sub>	0.54 <sup>0.96</sup> <sub>0.28</sub>
Rd-496641	150.438042	1.953417	16.9	0.0	1.50 <sup>1.80</sup> <sub>1.39</sub>	10.01 <sup>10.19</sup> <sub>9.79</sub>	0.37 <sup>0.70</sup> <sub>0.15</sub>
Rd-736212	150.443083	1.991972	53.6	0.3	1.93 <sup>2.55</sup> <sub>1.47</sub>	9.81 <sup>10.05</sup> <sub>9.56</sub>	0.13 <sup>0.41</sup> <sub>0.05</sub>
Vdlz-693689	150.579708	1.960222	18.6	0.2	2.46 <sup>2.55</sup> <sub>2.37</sub>	9.45 <sup>9.49</sup> <sub>9.41</sub>	0.01 <sup>0.01</sup> <sub>0.01</sub>
Vdlz-739684	150.479333	1.967639	16.3	0.2	2.18 <sup>2.28</sup> <sub>1.91</sub>	9.24 <sup>9.67</sup> <sub>9.18</sub>	0.01 <sup>0.15</sup> <sub>0.01</sub>
pz-496070	150.539750	1.951611	67.8	0.0	1.57 <sup>1.67</sup> <sub>1.20</sub>	10.25 <sup>10.41</sup> <sub>10.07</sub>	0.59 <sup>0.90</sup> <sub>0.31</sub>
pz-501373	150.403375	1.921306	3.9	0.0	1.03 <sup>1.14</sup> <sub>0.94</sub>	9.21 <sup>9.71</sup> <sub>8.72</sub>	0.20 <sup>0.69</sup> <sub>0.06</sub>
Rd-804402	149.902583	2.038389	10.8	0.0	1.51 <sup>1.70</sup> <sub>1.04</sub>	10.02 <sup>10.26</sup> <sub>9.73</sub>	0.43 <sup>0.90</sup> <sub>0.16</sub>
Vdlz-806404	150.055625	2.022333	26.9	0.0	1.13 <sup>1.21</sup> <sub>1.05</sub>	10.04 <sup>10.15</sup> <sub>9.91</sub>	0.96 <sup>1.24</sup> <sub>0.61</sub>
Gd-761379	150.323917	1.989667	9.2	0.0	1.31 <sup>1.45</sup> <sub>0.91</sub>	9.65 <sup>9.22</sup> <sub>9.22</sub>	0.30 <sup>0.90</sup> <sub>0.11</sub>
Gd-761974	150.342708	1.985333	14.5	0.2	1.82 <sup>1.92</sup> <sub>1.73</sub>	10.34 <sup>10.45</sup> <sub>10.20</sub>	0.43 <sup>0.58</sup> <sub>0.23</sub>
COSMOS	149.646875	2.081944	27.5	0.0	0.75 <sup>1.11</sup> <sub>0.65</sub>	9.94 <sup>10.23</sup> <sub>9.60</sub>	0.89 <sup>1.20</sup> <sub>0.55</sub>
N7bb-55-13095	149.741292	2.080944	16.4	0.3	1.92 <sup>2.46</sup> <sub>1.82</sub>	10.12 <sup>10.29</sup> <sub>9.83</sub>	0.20 <sup>0.32</sup> <sub>0.05</sub>
N7ib-55-10811	149.827292	2.089278	0.1	0.0	1.32 <sup>2.22</sup> <sub>0.37</sub>	9.69 <sup>10.63</sup> <sub>8.78</sub>	0.29 <sup>0.82</sup> <sub>0.11</sub>
N8bb-55-13814	149.832292	2.056139	0.5	0.0	2.49 <sup>3.44</sup> <sub>1.36</sub>	10.67 <sup>11.71</sup> <sub>9.55</sub>	0.23 <sup>0.56</sup> <sub>0.10</sub>
N8bb-56-14179	149.721833	2.067083	—	0.0	0.00 <sup>0.00</sup> <sub>0.00</sub>	0.00 <sup>0.00</sup> <sub>0.00</sub>	0.00 <sup>0.00</sup> <sub>0.00</sub>
Rd-843398	149.627500	2.108694	5.0	0.0	1.56 <sup>1.68</sup> <sub>1.13</sub>	9.85 <sup>10.10</sup> <sub>9.56</sub>	0.27 <sup>0.59</sup> <sub>0.11</sub>
pz-845477	149.664292	2.088861	38.2	0.3	1.83 <sup>2.37</sup> <sub>1.72</sub>	9.69 <sup>9.86</sup> <sub>9.42</sub>	0.10 <sup>0.17</sup> <sub>0.05</sub>
m45-851027	149.618792	2.051889	26.0	0.0	1.78 <sup>1.89</sup> <sub>1.39</sub>	10.30 <sup>10.48</sup> <sub>10.05</sub>	0.43 <sup>0.74</sup> <sub>0.16</sub>
Gd-827414	149.756250	2.050889	6.7	0.0	1.64 <sup>1.78</sup> <sub>1.24</sub>	9.90 <sup>10.30</sup> <sub>9.44</sub>	0.29 <sup>0.84</sup> <sub>0.10</sub>
Rdz-182496	149.753750	2.091028	23.9	0.0	1.64 <sup>2.07</sup> <sub>1.16</sub>	10.35 <sup>10.59</sup> <sub>10.07</sub>	0.43 <sup>0.80</sup> <sub>0.17</sub>
Vdz-189225	149.707042	2.066583	23.5	0.1	1.37 <sup>1.81</sup> <sub>1.22</sub>	9.80 <sup>10.08</sup> <sub>9.47</sub>	0.30 <sup>0.78</sup> <sub>0.11</sub>
COSMOS	149.898208	2.053139	4.7	0.0	0.64 <sup>1.22</sup> <sub>0.32</sub>	9.03 <sup>9.78</sup> <sub>8.43</sub>	0.28 <sup>0.86</sup> <sub>0.10</sub>
Rd-793496	149.941708	2.111806	4.5	0.2	1.61 <sup>2.11</sup> <sub>1.48</sub>	9.79 <sup>10.06</sup> <sub>9.45</sub>	0.17 <sup>0.41</sup> <sub>0.05</sub>
Vdlz-798659	149.971500	2.077139	36.4	0.0	1.08 <sup>1.17</sup> <sub>1.00</sub>	9.79 <sup>9.97</sup> <sub>9.53</sub>	0.62 <sup>1.00</sup> <sub>0.29</sub>
pz-776988	150.097333	2.051222	10.0	0.1	1.59 <sup>1.68</sup> <sub>1.51</sub>	10.13 <sup>10.26</sup> <sub>9.97</sub>	0.45 <sup>0.62</sup> <sub>0.26</sub>
Vd-802160	150.021292	2.053389	2.0	0.3	1.66 <sup>1.93</sup> <sub>1.26</sub>	9.77 <sup>9.98</sup> <sub>9.47</sub>	0.18 <sup>0.54</sup> <sub>0.05</sub>
Vdz-177851	150.016917	2.053667	7.7	0.3	2.33 <sup>2.49</sup> <sub>1.95</sub>	10.45 <sup>10.60</sup> <sub>10.09</sub>	0.17 <sup>0.36</sup> <sub>0.10</sub>
COSMOS	150.147625	2.052667	3.5	0.0	0.82 <sup>1.71</sup> <sub>0.03</sub>	9.28 <sup>10.25</sup> <sub>8.41</sub>	0.30 <sup>0.88</sup> <sub>0.11</sub>
COSMOS	150.128583	2.074750	237.0	0.0	1.16 <sup>1.25</sup> <sub>1.08</sub>	8.14 <sup>8.18</sup> <sub>8.11</sub>	0.01 <sup>0.01</sup> <sub>0.01</sub>
rd-746010	150.254333	2.092083	3.0	0.1	1.82 <sup>2.29</sup> <sub>1.33</sub>	10.09 <sup>10.69</sup> <sub>9.54</sub>	0.28 <sup>0.71</sup> <sub>0.11</sub>
Vd-749753	150.291042	2.075028	14.6	0.3	1.65 <sup>2.03</sup> <sub>1.29</sub>	9.77 <sup>10.01</sup> <sub>9.35</sub>	0.17 <sup>0.40</sup> <sub>0.06</sub>
Gd-776657	150.117458	2.049833	29.4	0.0	0.91 <sup>1.22</sup> <sub>0.82</sub>	9.96 <sup>10.10</sup> <sub>9.81</sub>	0.98 <sup>1.29</sup> <sub>0.53</sub>

Table 4—Continued

Source	RA J2000	DEC J2000	Best $\chi^2$	Best E(B-V)	Log Median SFR <sup>a</sup> (M <sub>⊙</sub> /yr)	Log Median Mass <sup>a</sup> (M <sub>⊙</sub> )	Median Age <sup>a</sup> (Gyr)
Gd-748233	150.334708	2.076333	12.0	0.0	1.57 <sup>1.70</sup> <sub>1.15</sub>	9.79 <sup>10.01</sup> <sub>9.57</sub>	0.21 <sup>0.56</sup> <sub>0.11</sub>
Vd-746980	150.354375	2.085639	9.4	0.2	1.55 <sup>1.79</sup> <sub>1.16</sub>	9.71 <sup>9.97</sup> <sub>9.28</sub>	0.19 <sup>0.50</sup> <sub>0.09</sub>
Gd-773404	150.163958	2.070556	49.1	0.0	1.38 <sup>1.49</sup> <sub>1.00</sub>	9.83 <sup>10.00</sup> <sub>9.64</sub>	0.32 <sup>0.60</sup> <sub>0.18</sub>
m45-769694	150.153458	2.101833	11.3	0.1	2.08 <sup>2.43</sup> <sub>1.85</sub>	10.80 <sup>10.93</sup> <sub>10.63</sub>	0.64 <sup>1.16</sup> <sub>0.19</sub>
chandra_931	150.359792	2.073694	3000.0	0.0	-99.00 <sup>-99.00</sup> <sub>-99.00</sub>	-99.00 <sup>-99.00</sup> <sub>-99.00</sub>	0.00 <sup>0.00</sup> <sub>0.00</sub>
COSMOS	149.697833	2.116889	23.6	0.0	0.75 <sup>1.15</sup> <sub>0.64</sub>	9.25 <sup>9.72</sup> <sub>8.76</sub>	0.31 <sup>0.94</sup> <sub>0.11</sub>
Rd-816509	149.780292	2.122583	21.4	0.0	1.47 <sup>1.57</sup> <sub>1.40</sub>	9.60 <sup>9.94</sup> <sub>9.22</sub>	0.17 <sup>0.41</sup> <sub>0.06</sub>
m45-1065581	149.758792	2.150722	9.0	0.2	2.25 <sup>2.49</sup> <sub>1.78</sub>	9.91 <sup>10.13</sup> <sub>9.46</sub>	0.06 <sup>0.25</sup> <sub>0.01</sub>
Gd-816625	149.817667	2.120833	20.9	0.1	1.36 <sup>1.48</sup> <sub>0.98</sub>	9.49 <sup>9.71</sup> <sub>9.19</sub>	0.16 <sup>0.56</sup> <sub>0.09</sub>
B12	149.971875	2.118222	—	0.0	0.00 <sup>0.00</sup> <sub>0.00</sub>	0.00 <sup>0.00</sup> <sub>0.00</sub>	0.00 <sup>0.00</sup> <sub>0.00</sub>
B16	149.933250	2.166917	—	0.0	0.00 <sup>0.00</sup> <sub>0.00</sub>	0.00 <sup>0.00</sup> <sub>0.00</sub>	0.00 <sup>0.00</sup> <sub>0.00</sub>
COSMOS	149.984000	2.126861	0.1	0.1	1.33 <sup>2.21</sup> <sub>0.55</sub>	9.70 <sup>10.63</sup> <sub>8.90</sub>	0.29 <sup>0.83</sup> <sub>0.10</sub>
N7bb-66-39741	150.017375	2.146056	22.7	0.0	1.06 <sup>1.44</sup> <sub>0.95</sub>	9.73 <sup>9.97</sup> <sub>9.39</sub>	0.45 <sup>0.88</sup> <sub>0.17</sub>
N8bb-54-1000	150.021000	2.121417	0.1	0.0	1.83 <sup>2.96</sup> <sub>1.80</sub>	10.19 <sup>11.22</sup> <sub>9.10</sub>	0.25 <sup>0.58</sup> <sub>0.10</sub>
COSMOS	150.295792	2.124889	1.6	0.0	0.58 <sup>0.99</sup> <sub>0.45</sub>	8.97 <sup>9.46</sup> <sub>8.48</sub>	0.24 <sup>0.75</sup> <sub>0.09</sub>
COSMOS	150.336542	2.127250	85.8	0.0	0.85 <sup>0.94</sup> <sub>0.76</sub>	9.88 <sup>10.14</sup> <sub>9.60</sub>	0.92 <sup>1.25</sup> <sub>0.58</sub>
COSMOS	150.271958	2.155750	4.1	0.0	0.65 <sup>0.95</sup> <sub>0.54</sub>	8.89 <sup>9.41</sup> <sub>8.31</sub>	0.20 <sup>0.70</sup> <sub>0.05</sub>
COSMOS	150.149000	2.155250	6.4	0.0	0.49 <sup>0.98</sup> <sub>0.34</sub>	8.98 <sup>9.79</sup> <sub>8.39</sub>	0.28 <sup>0.91</sup> <sub>0.10</sub>
N8bb-52-807	150.249054	2.121889	8.0	0.1	1.97 <sup>2.09</sup> <sub>1.60</sub>	10.44 <sup>10.61</sup> <sub>10.22</sub>	0.34 <sup>0.61</sup> <sub>0.15</sub>
Gd-988146	150.274792	2.163556	17.0	0.0	1.10 <sup>1.49</sup> <sub>1.00</sub>	10.06 <sup>10.25</sup> <sub>9.86</sub>	0.68 <sup>1.18</sup> <sub>0.33</sub>
rd-985942	150.320542	2.175194	14.1	0.1	1.50 <sup>1.59</sup> <sub>1.41</sub>	9.92 <sup>10.14</sup> <sub>9.66</sub>	0.32 <sup>0.62</sup> <sub>0.15</sub>
rd-1018964	150.187833	2.129056	19.9	0.2	1.62 <sup>1.97</sup> <sub>1.20</sub>	9.58 <sup>9.79</sup> <sub>9.28</sub>	0.13 <sup>0.32</sup> <sub>0.05</sub>
Gd-1018158	150.191833	2.133944	9.6	0.2	2.28 <sup>2.38</sup> <sub>1.77</sub>	10.86 <sup>10.95</sup> <sub>10.75</sub>	0.45 <sup>0.59</sup> <sub>0.20</sub>
zphot-1017802	150.178875	2.136806	4.8	0.1	1.55 <sup>1.77</sup> <sub>1.19</sub>	9.70 <sup>9.90</sup> <sub>9.38</sub>	0.18 <sup>0.55</sup> <sub>0.09</sub>
m45-990385	150.362833	2.148861	49.8	0.0	0.69 <sup>0.77</sup> <sub>0.67</sub>	10.79 <sup>10.87</sup> <sub>10.72</sub>	1.26 <sup>1.36</sup> <sub>0.16</sub>
B20	150.036542	2.193444	2.4	0.1	1.56 <sup>1.69</sup> <sub>1.17</sub>	9.83 <sup>10.05</sup> <sub>9.58</sub>	0.24 <sup>0.53</sup> <sub>0.11</sub>
zphot-1006191	150.076750	2.213083	13.4	0.1	1.53 <sup>1.93</sup> <sub>1.40</sub>	10.14 <sup>10.32</sup> <sub>9.95</sub>	0.51 <sup>0.96</sup> <sub>0.13</sub>
N7jp-38	150.230958	2.219222	0.1	0.5	1.66 <sup>2.61</sup> <sub>0.67</sub>	9.98 <sup>10.95</sup> <sub>9.03</sub>	0.28 <sup>0.71</sup> <sub>0.10</sub>
N8bb-65-12966	150.203208	2.227833	—	0.0	0.00 <sup>0.00</sup> <sub>0.00</sub>	0.00 <sup>0.00</sup> <sub>0.00</sub>	0.00 <sup>0.00</sup> <sub>0.00</sub>
N8jp-64-66	150.290500	2.253806	92.3	0.2	2.54 <sup>2.79</sup> <sub>1.89</sub>	11.22 <sup>11.37</sup> <sub>11.06</sub>	0.63 <sup>0.88</sup> <sub>0.24</sub>
Gd-1007642	150.110917	2.201667	22.8	0.0	1.18 <sup>1.28</sup> <sub>1.11</sub>	9.86 <sup>10.03</sup> <sub>9.65</sub>	0.63 <sup>0.98</sup> <sub>0.30</sub>
Gd-982981	150.332042	2.197389	12.6	0.1	1.39 <sup>1.48</sup> <sub>1.31</sub>	9.55 <sup>9.79</sup> <sub>9.35</sub>	0.18 <sup>0.35</sup> <sub>0.10</sub>
COSMOS	149.759083	2.295139	4.9	0.0	1.32 <sup>1.76</sup> <sub>0.79</sub>	9.93 <sup>10.23</sup> <sub>9.47</sub>	0.44 <sup>0.97</sup> <sub>0.15</sub>
Vdlz-1072997	149.595708	2.268528	28.1	0.2	2.24 <sup>2.63</sup> <sub>2.04</sub>	10.70 <sup>10.91</sup> <sub>10.52</sub>	0.40 <sup>0.92</sup> <sub>0.11</sub>
Vdlz-1291420	149.767917	2.312056	102.1	0.0	1.37 <sup>2.15</sup> <sub>1.21</sub>	10.95 <sup>11.04</sup> <sub>10.83</sub>	0.94 <sup>1.04</sup> <sub>0.83</sub>
Vdlz-1292624	149.735208	2.310917	31.0	0.1	1.77 <sup>1.90</sup> <sub>1.66</sub>	9.99 <sup>10.20</sup> <sub>9.71</sub>	0.22 <sup>0.39</sup> <sub>0.11</sub>
pz-1073870	149.618875	2.257278	22.2	0.0	1.28 <sup>1.63</sup> <sub>0.87</sub>	10.05 <sup>10.25</sup> <sub>9.76</sub>	0.67 <sup>1.06</sup> <sub>0.22</sub>
pz-1074954	149.678250	2.256639	21.4	0.2	1.48 <sup>1.96</sup> <sub>1.33</sub>	9.74 <sup>9.95</sup> <sub>9.46</sub>	0.17 <sup>0.46</sup> <sub>0.05</sub>
m45-1070303	149.587208	2.282917	18.1	0.0	1.80 <sup>2.50</sup> <sub>0.63</sub>	10.65 <sup>10.79</sup> <sub>10.46</sub>	0.49 <sup>0.88</sup> <sub>0.16</sub>
Vdz-245444	149.624917	2.271250	26.8	0.0	1.04 <sup>1.26</sup> <sub>0.93</sub>	9.16 <sup>9.74</sup> <sub>8.28</sub>	0.18 <sup>0.65</sup> <sub>0.11</sub>
N8bb-65-832	150.126667	2.287444	0.1	0.0	2.04 <sup>2.11</sup> <sub>0.98</sub>	10.32 <sup>11.36</sup> <sub>9.27</sub>	0.24 <sup>0.58</sup> <sub>0.10</sub>
N8bb-67-2393	149.875292	2.278528	—	0.0	0.00 <sup>0.00</sup> <sub>0.00</sub>	0.00 <sup>0.00</sup> <sub>0.00</sub>	0.00 <sup>0.00</sup> <sub>0.00</sub>
N7bb-77-42228	150.198583	2.300611	9.5	0.0	1.54 <sup>1.66</sup> <sub>1.12</sub>	9.80 <sup>10.01</sup> <sub>9.62</sub>	0.23 <sup>0.82</sup> <sub>0.13</sub>
N8bb-77-25517	150.167583	2.317750	6.1	0.0	1.26 <sup>1.53</sup> <sub>0.93</sub>	9.61 <sup>9.79</sup> <sub>9.35</sub>	0.26 <sup>0.58</sup> <sub>0.11</sub>
rd-974353	150.270208	2.253889	21.0	0.3	2.03 <sup>2.57</sup> <sub>1.86</sub>	10.06 <sup>10.27</sup> <sub>9.58</sub>	0.19 <sup>0.29</sup> <sub>0.05</sub>

Table 4—Continued

Source	RA J2000	DEC J2000	Best $\chi^2$	Best E(B-V)	Log Median SFR <sup>a</sup> (M <sub>⊙</sub> /yr)	Log Median Mass <sup>a</sup> (M <sub>⊙</sub> )	Median Age <sup>a</sup> (Gyr)
Gd-999142	150.135833	2.257917	10.4	0.0	1.42 <sup>1.83</sup> <sub>1.28</sub>	10.01 <sup>10.18</sup> <sub>9.84</sub>	0.41 <sup>0.80</sup> <sub>0.14</sub>
rd-968994	150.346000	2.292222	13.9	0.0	1.33 <sup>1.44</sup> <sub>1.24</sub>	9.89 <sup>10.12</sup> <sub>9.57</sub>	0.44 <sup>0.84</sup> <sub>0.16</sub>
Gd-971438	150.341167	2.272750	79.1	0.3	2.24 <sup>2.81</sup> <sub>2.13</sub>	10.14 <sup>10.27</sup> <sub>9.83</sub>	0.12 <sup>0.17</sup> <sub>0.01</sub>
rd-996859	150.214167	2.273111	20.4	0.3	2.30 <sup>2.38</sup> <sub>2.20</sub>	9.32 <sup>9.39</sup> <sub>9.27</sub>	0.01 <sup>0.11</sup> <sub>0.01</sub>
Gd-999621	150.217667	2.254306	33.3	0.0	1.35 <sup>1.79</sup> <sub>1.21</sub>	9.88 <sup>10.07</sup> <sub>9.67</sub>	0.36 <sup>0.76</sup> <sub>0.12</sub>
zphot-999389	150.143000	2.256833	4.5	0.2	1.43 <sup>2.01</sup> <sub>1.03</sub>	9.51 <sup>9.75</sup> <sub>9.11</sub>	0.16 <sup>0.38</sup> <sub>0.05</sub>
zphot-1218871	150.309292	2.311778	2.3	0.1	1.55 <sup>2.00</sup> <sub>1.07</sub>	10.05 <sup>10.42</sup> <sub>9.58</sub>	0.32 <sup>0.90</sup> <sub>0.12</sub>
COSMOS	150.042042	2.317250	68.6	0.0	0.85 <sup>0.95</sup> <sub>0.76</sub>	9.49 <sup>9.81</sup> <sub>8.90</sub>	0.56 <sup>1.14</sup> <sub>0.14</sub>
N8jp-79-27	149.877583	2.331694	68.7	0.1	2.41 <sup>2.90</sup> <sub>1.90</sub>	10.78 <sup>11.35</sup> <sub>10.10</sub>	0.28 <sup>0.64</sup> <sub>0.11</sub>
Gd-1258302	149.946125	2.375806	31.5	0.3	2.33 <sup>2.91</sup> <sub>1.91</sub>	10.27 <sup>10.48</sup> <sub>9.99</sub>	0.11 <sup>0.50</sup> <sub>0.05</sub>
zphot-1262018	150.008667	2.350889	10.8	0.0	1.22 <sup>1.37</sup> <sub>0.83</sub>	9.62 <sup>9.86</sup> <sub>9.31</sub>	0.35 <sup>0.90</sup> <sub>0.14</sub>
m45-1256817	149.950500	2.386028	19.4	0.0	1.00 <sup>1.49</sup> <sub>0.92</sub>	9.70 <sup>10.17</sup> <sub>9.32</sub>	0.41 <sup>0.88</sup> <sub>0.15</sub>
N7jp-45	150.343500	2.380528	1.8	0.0	1.37 <sup>1.80</sup> <sub>0.87</sub>	9.66 <sup>10.03</sup> <sub>9.14</sub>	0.26 <sup>0.66</sup> <sub>0.10</sub>
Gd-1215565	150.292250	2.332306	12.7	0.0	1.23 <sup>1.62</sup> <sub>1.06</sub>	9.86 <sup>10.08</sup> <sub>9.59</sub>	0.38 <sup>0.95</sup> <sub>0.15</sub>
rd-1233539	150.180083	2.378333	6.6	0.1	1.92 <sup>2.05</sup> <sub>1.80</sub>	10.62 <sup>10.74</sup> <sub>10.46</sub>	0.63 <sup>0.92</sup> <sub>0.29</sub>
COSMOS	149.970125	2.406750	11.1	0.0	1.12 <sup>1.55</sup> <sub>0.60</sub>	10.08 <sup>10.28</sup> <sub>9.84</sub>	0.67 <sup>1.05</sup> <sub>0.28</sub>
N7jp-47	149.958417	2.414278	3.3	0.0	1.20 <sup>1.69</sup> <sub>0.49</sub>	9.57 <sup>10.03</sup> <sub>8.96</sub>	0.29 <sup>0.73</sup> <sub>0.11</sub>
rd-1251268	150.009625	2.423361	10.8	0.1	1.74 <sup>2.13</sup> <sub>1.58</sub>	10.26 <sup>10.46</sup> <sub>10.07</sub>	0.31 <sup>0.84</sup> <sub>0.12</sub>
Vd-1254662	150.059917	2.400333	398.0	0.2	2.90 <sup>2.99</sup> <sub>2.82</sub>	9.88 <sup>11.32</sup> <sub>9.83</sub>	0.01 <sup>0.34</sup> <sub>0.01</sub>
N7bb-77-3905	150.171167	2.443722	10.2	0.0	1.21 <sup>1.38</sup> <sub>0.76</sub>	9.91 <sup>10.09</sup> <sub>9.68</sub>	0.56 <sup>0.92</sup> <sub>0.23</sub>
N8bb-77-5438	150.163000	2.425694	3.1	0.0	0.96 <sup>1.37</sup> <sub>0.81</sub>	9.35 <sup>9.60</sup> <sub>8.98</sub>	0.22 <sup>0.54</sup> <sub>0.10</sub>
Rd-1204998	150.335792	2.402444	1.5	0.1	1.42 <sup>1.93</sup> <sub>1.01</sub>	9.60 <sup>10.34</sup> <sub>9.13</sub>	0.24 <sup>0.67</sup> <sub>0.10</sub>
Rd-1205280	150.254875	2.399583	13.7	0.1	2.24 <sup>2.41</sup> <sub>1.83</sub>	10.54 <sup>10.72</sup> <sub>10.33</sub>	0.26 <sup>0.88</sup> <sub>0.12</sub>
m45-1201590	150.302042	2.428556	23.6	0.5	2.33 <sup>2.76</sup> <sub>1.95</sub>	10.67 <sup>10.85</sup> <sub>10.43</sub>	0.24 <sup>0.67</sup> <sub>0.05</sub>
m45-1202980	150.344125	2.417528	36.8	0.0	0.85 <sup>1.32</sup> <sub>0.72</sub>	10.43 <sup>10.53</sup> <sub>8.72</sub>	0.96 <sup>1.11</sup> <sub>0.80</sub>
pz-1201657	150.280625	2.428556	22.7	0.1	1.47 <sup>1.87</sup> <sub>1.33</sub>	9.88 <sup>10.21</sup> <sub>9.55</sub>	0.29 <sup>0.76</sup> <sub>0.11</sub>
Vd-1203402	150.332958	2.413222	11.4	0.1	1.75 <sup>1.86</sup> <sub>1.64</sub>	9.76 <sup>9.93</sup> <sub>9.46</sub>	0.12 <sup>0.20</sup> <sub>0.05</sub>
COSMOS	150.009458	2.463306	0.1	0.1	1.02 <sup>1.82</sup> <sub>0.28</sub>	9.40 <sup>10.23</sup> <sub>8.64</sub>	0.29 <sup>0.82</sup> <sub>0.11</sub>
COSMOS	150.006167	2.463944	59.5	0.0	0.97 <sup>1.16</sup> <sub>0.87</sub>	9.08 <sup>9.66</sup> <sub>8.18</sub>	0.21 <sup>0.79</sup> <sub>0.05</sub>
N7bb-91-33633	149.872250	2.497306	0.1	0.0	1.29 <sup>2.17</sup> <sub>0.76</sub>	9.70 <sup>10.59</sup> <sub>8.95</sub>	0.26 <sup>0.68</sup> <sub>0.10</sub>
Id-1487302	149.981167	2.479972	0.6	0.1	2.16 <sup>2.43</sup> <sub>1.73</sub>	10.61 <sup>10.81</sup> <sub>10.35</sub>	0.34 <sup>0.80</sup> <sub>0.13</sub>
m45-1465195	150.078417	2.470611	53.3	0.4	2.75 <sup>2.85</sup> <sub>2.64</sub>	11.28 <sup>11.51</sup> <sub>11.04</sub>	0.42 <sup>0.89</sup> <sub>0.20</sub>
Vd-1246631	149.952208	2.455639	47.2	0.0	0.99 <sup>1.30</sup> <sub>0.74</sub>	9.89 <sup>10.23</sup> <sub>9.52</sub>	0.73 <sup>1.08</sup> <sub>0.27</sub>
Vd-1460158	150.108875	2.505500	24.6	0.2	2.00 <sup>2.19</sup> <sub>1.48</sub>	9.58 <sup>9.78</sup> <sub>9.14</sub>	0.05 <sup>0.23</sup> <sub>0.01</sub>
COSMOS	150.220625	2.460333	9.6	0.0	1.12 <sup>1.97</sup> <sub>0.23</sub>	9.82 <sup>10.73</sup> <sub>8.86</sub>	0.35 <sup>0.95</sup> <sub>0.12</sub>
N7ib-89-31722	150.138250	2.509056	2.5	0.0	0.97 <sup>1.55</sup> <sub>0.70</sub>	9.28 <sup>9.93</sup> <sub>8.72</sub>	0.23 <sup>0.64</sup> <sub>0.09</sub>
Id-1439889	150.291875	2.474806	13.4	0.3	1.92 <sup>2.14</sup> <sub>1.50</sub>	10.10 <sup>10.35</sup> <sub>9.70</sub>	0.21 <sup>0.53</sup> <sub>0.10</sub>
Vdlz-1435552	150.329583	2.506417	18.5	0.1	1.49 <sup>1.96</sup> <sub>1.38</sub>	9.78 <sup>10.00</sup> <sub>9.54</sub>	0.22 <sup>0.48</sup> <sub>0.05</sub>
COSMOS	150.075042	2.552194	0.1	0.0	0.40 <sup>1.40</sup> <sub>-0.44</sub>	8.83 <sup>9.79</sup> <sub>7.93</sub>	0.29 <sup>0.86</sup> <sub>0.11</sub>
COSMOS	149.966625	2.528000	3.8	0.0	0.67 <sup>1.64</sup> <sub>0.15</sub>	9.19 <sup>10.24</sup> <sub>8.41</sub>	0.30 <sup>0.90</sup> <sub>0.11</sub>
N8jp-90-36	149.962500	2.539694	5.7	0.0	2.01 <sup>2.10</sup> <sub>0.94</sub>	10.30 <sup>11.34</sup> <sub>9.26</sub>	0.24 <sup>0.58</sup> <sub>0.10</sub>
Vdlz-1474770	150.030667	2.570639	26.1	0.0	1.06 <sup>1.18</sup> <sub>0.97</sub>	9.75 <sup>9.92</sup> <sub>9.50</sub>	0.58 <sup>0.98</sup> <sub>0.22</sub>
pz-1456157	150.100375	2.526806	23.1	0.2	1.86 <sup>1.97</sup> <sub>1.45</sub>	9.76 <sup>9.92</sup> <sub>9.55</sub>	0.10 <sup>0.32</sup> <sub>0.05</sub>
pz-1473252	149.974833	2.569944	21.2	0.0	1.07 <sup>1.20</sup> <sub>0.98</sub>	9.44 <sup>9.82</sup> <sub>9.01</sub>	0.28 <sup>0.74</sup> <sub>0.10</sub>
pz-1481860	149.988542	2.520250	27.5	0.0	1.07 <sup>1.16</sup> <sub>1.00</sub>	9.69 <sup>9.95</sup> <sub>9.26</sub>	0.54 <sup>0.99</sup> <sub>0.18</sub>

Table 4—Continued

Source	RA J2000	DEC J2000	Best $\chi^2$	Best E(B-V)	Log Median SFR <sup>a</sup> ( $M_{\odot}/\text{yr}$ )	Log Median Mass <sup>a</sup> ( $M_{\odot}$ )	Median Age <sup>a</sup> (Gyr)
SMA3	150.086250	2.589028	80.6	0.2	2.08 <sup>2.43</sup> <sub>1.98</sub>	10.64 <sup>10.77</sup> <sub>10.47</sub>	0.47 <sup>0.66</sup> <sub>0.14</sub>
Rd-1442768	150.104083	2.621750	7.6	0.0	1.09 <sup>1.50</sup> <sub>0.96</sub>	9.69 <sup>9.88</sup> <sub>9.44</sub>	0.35 <sup>0.86</sup> <sub>0.14</sub>
Rd-1686652	150.016792	2.626694	4.9	0.2	2.24 <sup>2.75</sup> <sub>2.13</sub>	10.09 <sup>10.23</sup> <sub>9.84</sub>	0.10 <sup>0.14</sup> <sub>0.05</sub>
m45-1711133	150.011292	2.627861	6.7	0.1	1.68 <sup>2.09</sup> <sub>1.16</sub>	10.59 <sup>10.70</sup> <sub>10.42</sub>	0.58 <sup>1.13</sup> <sub>0.28</sub>
Vd-1469863	150.002042	2.605361	1.3	0.2	1.52 <sup>1.99</sup> <sub>1.05</sub>	9.80 <sup>10.41</sup> <sub>9.25</sub>	0.28 <sup>0.81</sup> <sub>0.10</sub>
Vd-1708971	149.979833	2.635639	22.6	0.3	1.87 <sup>2.48</sup> <sub>1.42</sub>	9.78 <sup>9.98</sup> <sub>9.50</sub>	0.12 <sup>0.35</sup> <sub>0.01</sub>
Gd-1470575	149.983375	2.599389	9.5	0.0	0.99 <sup>1.08</sup> <sub>0.91</sub>	9.63 <sup>9.85</sup> <sub>9.33</sub>	0.55 <sup>0.98</sup> <sub>0.21</sub>
Gd-1710861	150.006750	2.630083	9.0	0.2	1.27 <sup>1.84</sup> <sub>1.13</sub>	9.34 <sup>9.64</sup> <sub>8.88</sub>	0.15 <sup>0.34</sup> <sub>0.05</sub>
COSMOS	149.894875	2.670917	6.4	0.0	0.98 <sup>1.48</sup> <sub>0.53</sub>	9.51 <sup>10.19</sup> <sub>8.92</sub>	0.32 <sup>0.93</sup> <sub>0.11</sub>
N7bb-101-29864	150.111333	2.684972	36.2	0.2	2.45 <sup>2.55</sup> <sub>1.82</sub>	9.49 <sup>9.80</sup> <sub>9.43</sub>	0.04 <sup>0.13</sup> <sub>0.01</sub>
N7jp-69	149.944458	2.704361	94.2	0.0	0.87 <sup>1.11</sup> <sub>0.76</sub>	9.07 <sup>9.59</sup> <sub>8.09</sub>	0.23 <sup>0.72</sup> <sub>0.05</sub>
N8bb-101-23318	150.121333	2.687722	—	0.0	0.00 <sup>0.00</sup> <sub>0.00</sub>	0.00 <sup>0.00</sup> <sub>0.00</sub>	0.00 <sup>0.00</sup> <sub>0.00</sub>
N8bb-101-23908	150.093750	2.684278	18.7	0.0	1.25 <sup>1.66</sup> <sub>0.85</sub>	9.67 <sup>10.00</sup> <sub>9.25</sub>	0.31 <sup>0.68</sup> <sub>0.12</sub>
pz-1682081	150.078458	2.657444	11.0	0.0	1.53 <sup>1.65</sup> <sub>1.11</sub>	9.96 <sup>10.12</sup> <sub>9.79</sub>	0.31 <sup>0.90</sup> <sub>0.19</sub>
pz-1725039	149.890917	2.698944	19.5	0.2	1.71 <sup>1.87</sup> <sub>1.31</sub>	9.88 <sup>10.20</sup> <sub>9.48</sub>	0.21 <sup>0.62</sup> <sub>0.10</sub>
Vd-1697491	149.901167	2.719361	3.5	0.0	1.44 <sup>1.82</sup> <sub>1.30</sub>	9.86 <sup>10.20</sup> <sub>9.51</sub>	0.30 <sup>0.80</sup> <sub>0.12</sub>
N8bb-115-24856	149.889250	2.832222	48.5	0.0	1.24 <sup>1.89</sup> <sub>0.94</sub>	9.54 <sup>10.33</sup> <sub>8.96</sub>	0.22 <sup>0.57</sup> <sub>0.09</sub>
N8jp-114-35	149.958583	2.901694	2.3	0.0	2.76 <sup>3.53</sup> <sub>1.61</sub>	10.90 <sup>11.84</sup> <sub>9.55</sub>	0.20 <sup>0.54</sup> <sub>0.05</sub>
N7ib-66-9535	149.967958	2.258167	4.1	0.0	1.21 <sup>2.15</sup> <sub>0.72</sub>	9.60 <sup>10.62</sup> <sub>8.85</sub>	0.26 <sup>0.70</sup> <sub>0.10</sub>

<sup>a</sup>The superscripts (subscripts) represent the 84% (16%) values of the likelihood distribution from the SED fitting

Table 5. Ly $\alpha$  Escape Fractions

Type	Mean $f_{esc}$	Median $f_{esc}$	$\sigma_{f_{esc}}$
$B_J$ & $g^+$ LBGs:	0.29	0.13	0.32
$V_J$ LBGs:	0.30	0.10	0.45
$r^+$ LBGs:	0.14	0.07	0.22
IA624:	1.51	0.96	2.27
NB711:	0.41	0.20	0.54
NB816:	0.37	0.26	0.39

Table 6. Ly $\alpha$  Emission  $1\sigma$  Upper Limits

Source	RA J2000	DEC J2000	z	Flux Upper Limit ( $1e-18$ ergs/cm $^2$ /s)
m45-845998	149.653809	2.084128	4.080	8.5
Vdlz-528373	150.248474	1.896556	4.540	6.5
N7bb-77-37461	150.191086	2.317983	4.376	6.4
Vdlz-1475339	149.898865	2.566839	4.504	11.1
m45-1492079	149.869263	2.617303	4.274	11.5
pz-1232157	150.225754	2.387444	4.276	8.6
Id-533224	150.297577	1.868394	5.430	4.8
pz-561143	150.156738	1.851828	3.885	7.1
id-122195	150.035584	1.934689	5.580	3.8
id-110783	150.235519	1.888269	5.410	5.8
Rc-27-8213	150.404953	1.751894	4.969	7.9
B-4667	150.595856	1.914678	4.169	13.8
N7bb-88-31418	150.390366	2.510094	4.203	0.2
N7bb-30-38883	149.938736	1.657944	4.372	8.3
N7bb-50-39856	150.680740	1.989203	4.578	5.7